Implementation of an Ytterbium 171 Trapped Ion Qubit

By
Naleli Jubert Matjelo

Dissertation presented for the Degree of Doctor of Philosophy
in the Faculty of Science at Stellenbosch University

Laser Research Institute
Physics Department
Private Bag X1
Matieland, 7602

Promoters:
Prof. Hermann Uys
Dr. Christine Steenkamp

March 2020

Declaration

I declare that this dissertation is my own, unaided work. It is being submitted for the degree of Doctor of Philosophy in Physics at the University of Stellenbosch. It has not been submitted before for any degree or examination in any other university.

Signature of Author . . . . . .

March 2020

Abstract

This thesis presents the work done in developing an ion trap lab at Stellenbosch university. A linear Paul trap was assembled under a microscope and geometrically verified using a laser beam and a translational stage. A helical resonator and an LC resonator, to be used for generation of the necessary ion trapping potential, were implemented and characterized in detail, both through modeling and measurement. The helical resonator was used to successfully trap our first cloud of Doppler cooled Ytterbium ions under ultra-high vacuum conditions. Subsequently single ions were trapped successfully. The work culminated in the demonstration of Rabi oscillations in ytterbium 171 ions, a confirmation that we can operate the ions as qubits. One chapter in this thesis discusses theoretical work done under the atomic clock group at NIST on modeling power law noise which affects, among other things, oscillators and resonators such as lasers and optical cavities by broadening their linewidths. In that model we adapt the Barnes-Jarvis model and Mandlebrot model to generate noise with desired spectral properties. We also show that Barnes-Jarvis model and Mandelbrot models can be transformed into one another using partial fractions in frequency domain. In an attempt to model the noise distribution of power law noise, over a given band of frequencies, we invoke the Gaussian Mixture Models. This theoretical work on power law noise models is of importance to our lab here in Stellenbosch since we have a long history of research in mitigation of decoherence, as well as quantum state monitoring and feedback control, all of which rely strongly on detailed knowledge of the underlying noise processes.

Acknowledgements

The success of this work has been the product of an unwearying support from the people who dared to sacrifice their times for the sake of the work presented in this document. On that note, I would like to proceed and thank these people who offered support in this work:

- Prof. Hermann Uys and Dr. Christine Steenkamp for the guidance, encouragement and technical support they gave as my primary advisers in every bit of this work.
- Dr. David Leibrandt for the technical support and guidance he offered as my adviser at the National Institute of Standards and Technology (NIST).
- Mrs Anneke Bester and Prof de Swardt in Engineering Department, Stellenbosch, for their assistance with some circuit testing equipment.
- Stellenbosch University and CSIR for their financial assistance and provision of lab facilities to make this work a success.
- NIST for its support and financial assistance during my six-month visit at its lab facilities in Boulder, Colorado.
- My colleagues for the motivation they gave me throughout the course of this work.
- My family and friends for their love and support.

Contents

List of Tables

List of Figures

Chapter 1

Introduction

Quantum effects such as entanglement and matter-wave interference are predicted to be corner-stones of future technologies [5]. For instance, quantum entanglement plays a fundamental role in quantum information processing, a field which has a potential to revolutionize modern communications and computations [6]. Ion trapping [7, 8] is one of the leading approaches for realizing quantum phenomena including realization of qubits, atomic clocks and quantum computers [9–13]. An overview of our ion trap lab is given in the next section.

1.1 Lab Overview

Our lab setup is composed of various systems including vacuum system, ion trap setup, potential generation system, imaging setup, lasers and optics, computers and various electronics. The story starts with an ion trap mounted in the vacuum chamber and some ovens which emit neutral atoms to be ionized by lasers and ultimately trapped by the ion trap. A system of static and radiofrequency voltage sources is connected to the ion trap to provide the necessary potentials for trapping atomic ions with a particular charge to mass ratio. Lasers give out beams of appropriate wavelengths. A system of optics fixed on the optics table guides the laser beams through various beam paths, one being a fraction that goes to the wavelength meter and another beam path that goes through acousto-optics modulators (AOMs) and electo-optic modulators (EOMs) along the way to trapped ions in a vacuum chamber.

1.1.1 Lasers and Optics

Fig. 1.1 below shows the beam paths from the lasers to the wavelength meter as well as to the ion trap. For the work presented here, the hollow cathode lamp (HCL) spectroscopy was not used hence no beam was present in those paths towards HCL spectroscopy.

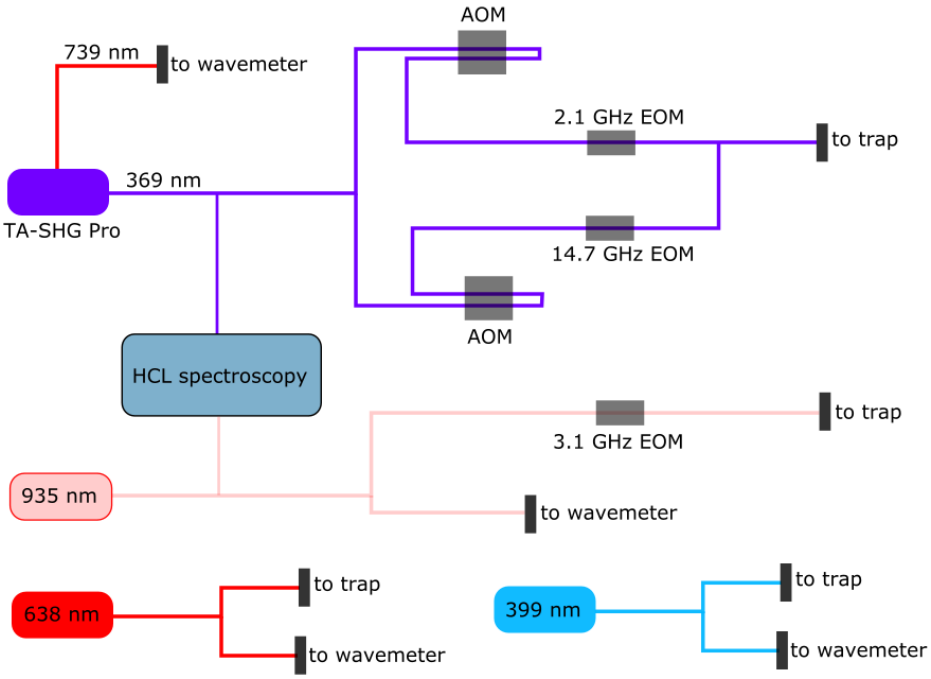

Fig. 1.1: A schematic diagram of lasers and laser beam paths towards the ion trap in a vacuum chamber.

AOMs were used to switch laser beams on and off while EOMs were used to generate the sidebands necessary for excitation of various transitions of the trapped ion.

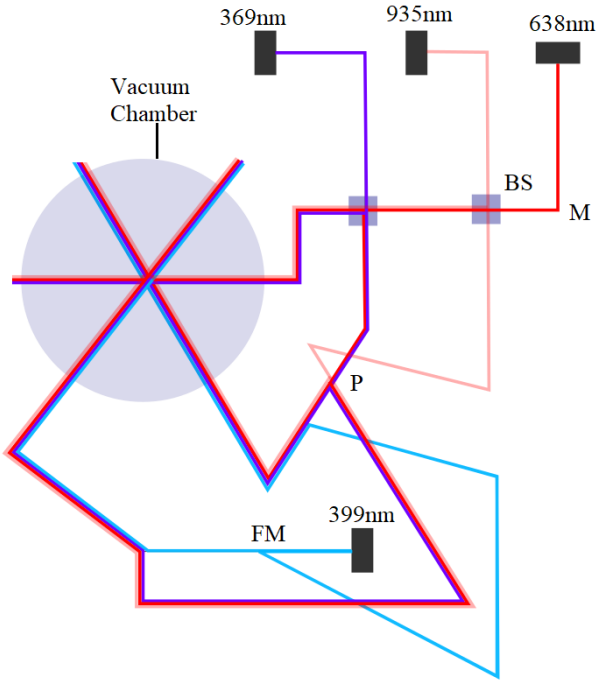

Fig. 1.2: A schematic diagram of laser beams going into the vacuum chamber and crossing each other at the center of an ion trap.

Fig. 1.2 above shows the laser beams guided into the vacuum chamber by some optics elements such as beam splitter (BS), mirror (M), flipper mirror (FM) and pellicle beam splitter (P). The following picture in Fig. 1.3 shows our optics table and the corresponding electronic controls and monitors just above the the table.

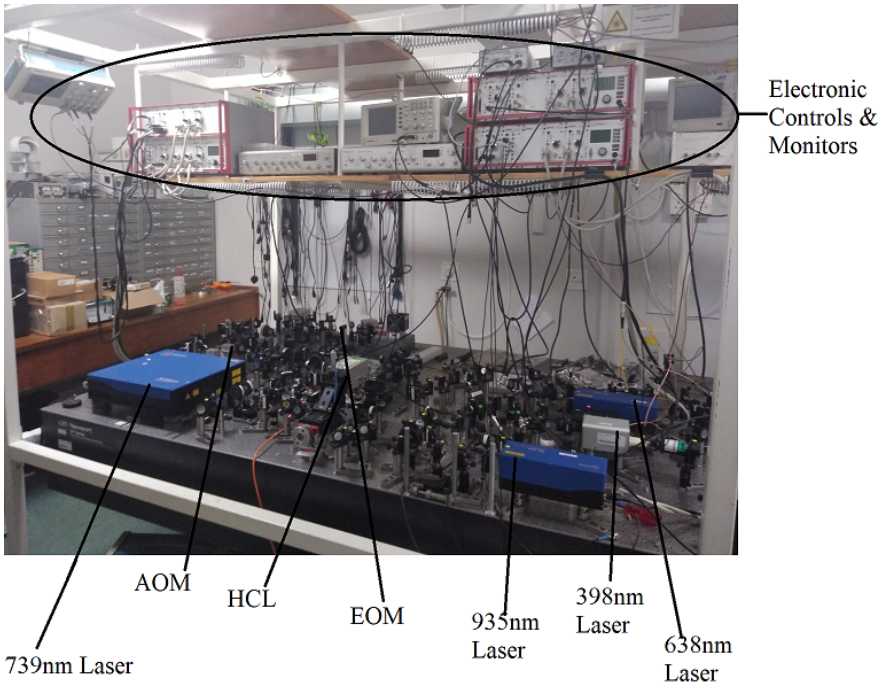

Fig. 1.3: Our optics table and the corresponding electronic controls and scopes.

1.1.2 Vacuum System and Imaging Setup

The following schematic diagram in Fig. 1.4 shows our vacuum system with pipes to various pumps and gauge. It also shows the imaging setup involving the lens stack, filter, PMT and a camera.

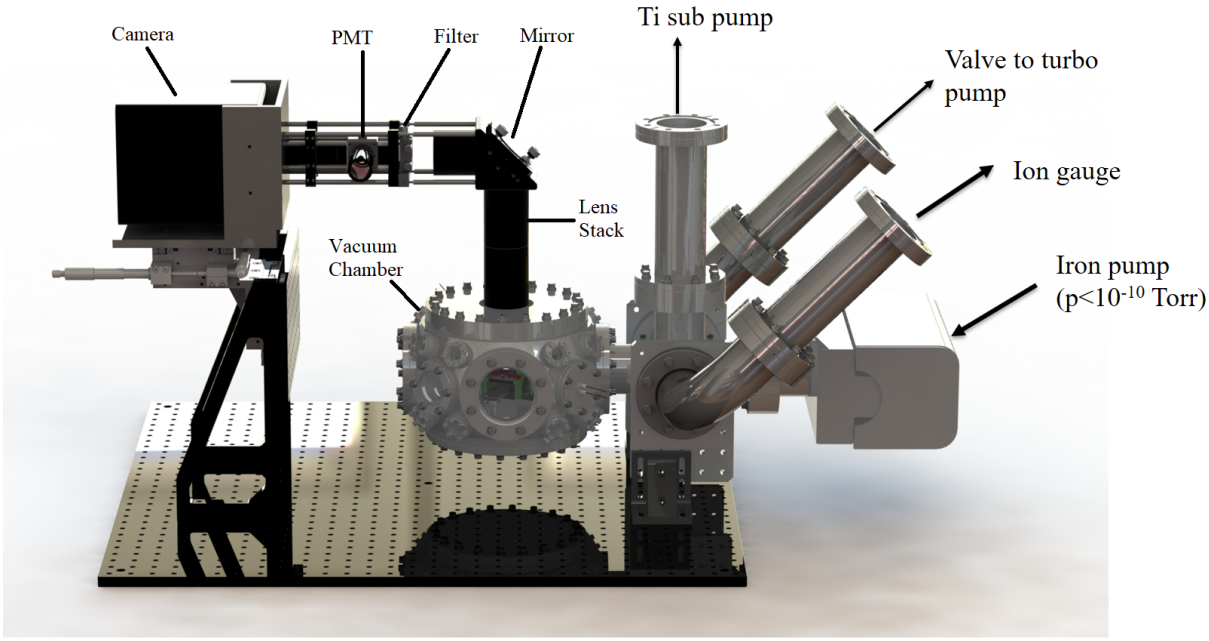

Fig. 1.4: A schematic diagram of our vacuum system as well as the imaging setup.

1.1.3 Ion Trap and Potential Generation Setup

Fig. 1.5 below show how radiofrequency (RF) potential (sine wave) was prepared and delivered to the RF electrodes of the ion trap. The rf amplifier has a typical gain of 43 dB in the frequencies ranging from 0.1 MHz to 200 MHz.

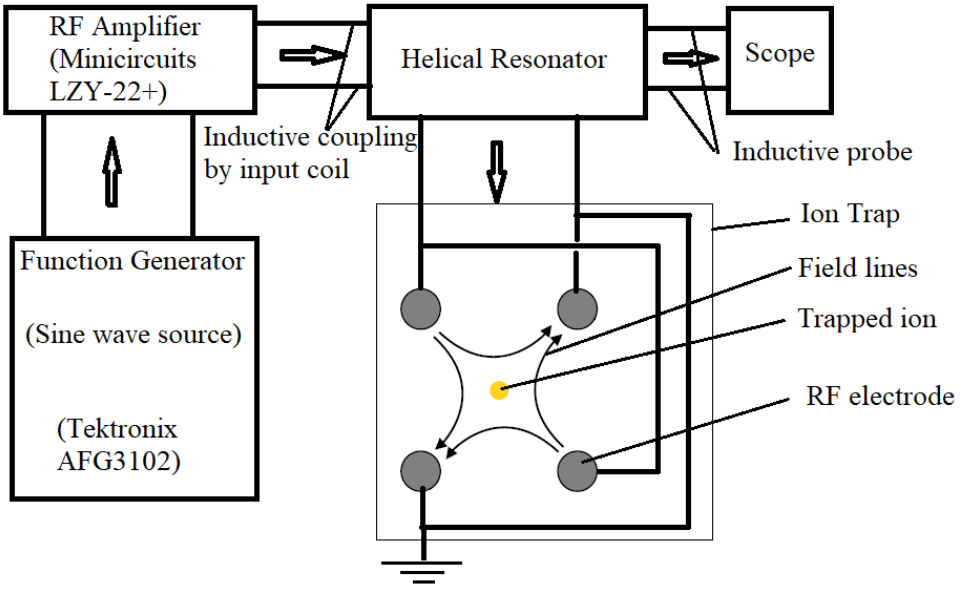

Fig. 1.5: A schematic diagram of the radiofrequency (RF) potential generation setup and how it connects to the ion trap's RF electrodes.

The connection between the rf amplifier and the helical resonator is actually inductive coupling using an input coil as will be shown the next chapter. The same case of inductive coupling holds in the connection between the helical resonator and the scope. The ion trap shown here is the cross-sectional view without the endcaps. Static voltage is applied to the endcaps. A complete picture of an ion trap showing all electrode will be shown in the next chapter. Fig. 1.6 below shows the imaging system, helical resonator and a vacuum chamber

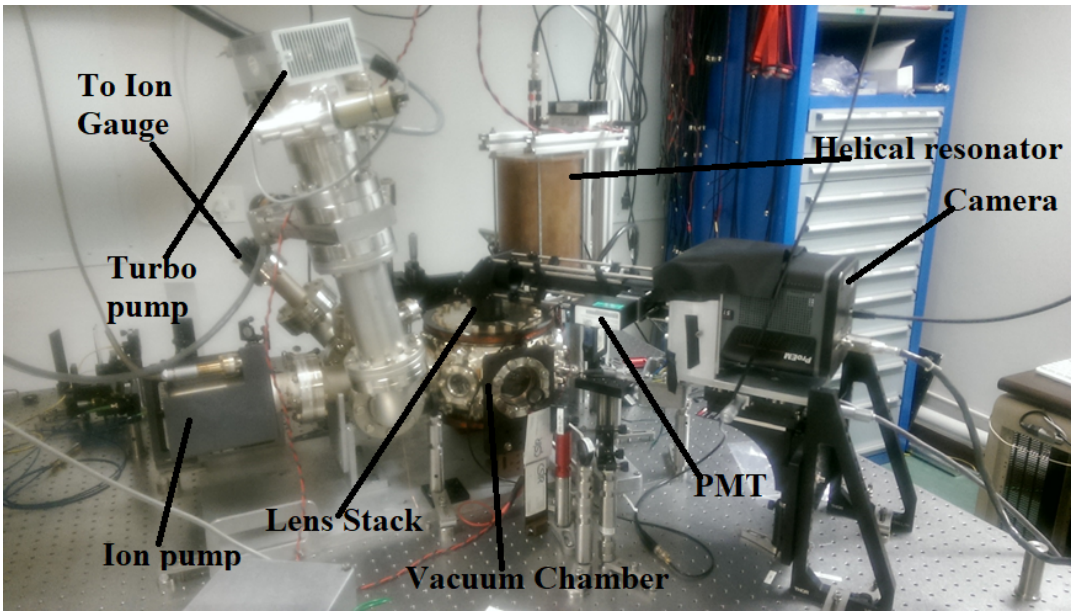

Fig. 1.6: A picture showing the helical resonator, imaging system as well as the vacuum chamber.

1.2 Motivation and Problem Statement

Our group at Stellenbosch University has a longstanding interested in aspects of quantum state monitoring and feedback control, particularly through the use unsharp measurements. Unsharp measurements or weak measurements [14] are a class of non-projective measurements, that do not disturb quantum dynamics as dramatically as the usual von Neumann (projective) measurements, at the cost of reduced information gain per measurement. Our group has shown, through computational modeling, that is possible to dynamically monitor a quantum state using sequential unsharp measurements, and construct a high fidelity estimate of the quantum state even asymptotically and even in the presence of dephasing noise [15]. The iterative state estimation method in [15] served the basis for further explorations in quantum process tomography [16], quantum feedback control [17], and feedback control resulting from measurement [18].

These principles are applicable to any controllable quantum system. It is the ambition of the laboratory to carry out such investigations on single quantum particles and we have chosen trapped ions to that end. Through my thesis work I have laid the foundation for these future studies by implementing an ytterbium 171, trapped ion qubit. I demonstrated trapping of individual ions, and qubit behaviour through the implementation Rabi oscillations on the ytterbium ion clock transition in the ground state hyperfine manifold. I also include in the thesis a theory project carried out partly under the guidance of Dr. David Leibrandt at the National Institute of Standards and Technology, which I visited as part of my PhD training. The study of quantum state monitoring cannot be separated from the study of noise, since challenges relating to decoherence inducing noise processes are part and parcel of every single quantum control experiment. The study was motivated by the need for accurate noise modeling toward improved atomic clock stability. The efficient method of generating noise trajectories with designed spectral and distribution properties, which I proposed, is also expected to be useful for future theoretical studies by the Stellenbosch group, which has previously relied on more computationally taxing methods [15, 19] in their modeling of quantum state monitoring experiments.

As one of the two final chapters I include a look at an alternative method of ion detection, namely image current detection, which we are starting to implement with a look toward future work. This tool is expected to open several new avenues of investigation including feedback cooling, pressure sensing, and potentially even qubit state detection if single ion image current detection can be achieved. Tools and concepts required in the analysis of the amplification and filtering methods for image current flows naturally from the tools developed in earlier chapters which covered characterization of resonators.

1.3 Objectives of Study

To create a trapped ytterbium ion qubit, we set out to implement all of the following objectives:

- Assemble a linear Paul trap.

- Generate and monitor rf potential to be used in trapping Ytterbium ions and characterize the instrumentation.
- Setup a laser cooling system including acousto-optic modulator switches and electro-optical modulators for generating sideband frequencies for optical pumping and closing the cooling transition.
- Setup an ultra-high vacuum system and achieve ultra-high vacuum.
- Construct imaging optics.
- Demonstrate successful trapping of Ytterbium ions.
- Demonstrate a trapped ion qubit with ytterbium 171 by implementing Rabi oscillations.
- Finally, we present a theoretical treatment of power law noise modeling. This is in preparation for handling power law noise associated with optical cavities to be implemented for laser locking as part of future work.

1.4 Scope and Limitations

I was directly responsible for major parts of each of the objectives listed above aside from the construction of an imaging system. That is, I was directly involved in the following parts of the setup and tasks:

- Assembly of a linear Paul trap.
- Generation and monitoring of rf potential to be used in trapping Ytterbium ions and characterizing the instrumentation.
- Setting up a laser cooling system including acousto-optic modulator switches and electro-optical modulators for generating sideband frequencies for optical pumping and closing the cooling transition.
- Setting up an ultra-high vacuum system and achieving ultra-high vacuum.
- Demonstrating a successful trapping of Ytterbium ions.
- Demonstrating a trapped ion qubit with ytterbium 171 by implementing Rabi oscillations.
- Proposing and analyzing the models for detecting image current due to trapped ions (although not implemented).
- Finally, presenting a theoretical treatment of power law noise modeling. This is in preparation for handling power law noise associated with optical cavities to be implemented for laser locking as part of future work.

We do not, however, discuss in detail all these aspects, but rather focus on those where my particular background as an engineer contributed uniquely to the group. Aspects regarding the ultra-high vacuum are for example only summarized very briefly. In this study we assume an rf potential source is available (i.e. signal generator) and focus only on stepping up and filtering the voltage by implementing appropriate resonators. Not all types of resonators are addressed here, only two lumped element-based (e.g. passive and active LC resonators) and helical resonator are covered in detail. The trap stability theory is discussed from the theoretical perspective but the trap stability mapping or characterization of our trap is not covered in this work. The Rabi flops experiment was carried out with a cloud of ions rather than single ions, because at the time we were operating under non-ideal vacuum conditions which necessitated clouds to allow a reasonable fluorescence signal.

1.5 Thesis Structure and Outline

The structure of this thesis is such that the background and literature review is presented in respective sections of each chapter rather than in one dedicated chapter. Chapter 2 of this work addresses the generation of quadrupole fields which are central to the trapping of ions. An rf signal from a signal generator is fed into an RF amplifier and a resonator before getting to the trap. An assembly and alignment of the linear Paul trap electrodes is carried out under the microscope after which a laser beam is used to characterize the linear Paul trap geometrical imperfections. A large portion of this chapter covers the resonator theory and implementation of both a helical and lumped element RLC resonators along with a discussion of impedance matching options.

Chapter 3 addresses the concepts and elements of trapping and manipulating Yb^{+}in particular. A background on laser-atom interaction is presented for completeness and serves as introductory tool for qubit rotations with microwave pulses presented later in the chapter. A two-photon process which takes place during the photoionization of Yb atoms along with the laser beam geometry into the vacuum chamber as well as trap characterization are presented in this chapter. With respect to the laser beam geometry into the trap, the Doppler cooling and isotope selection are made possible and Rabi flops are demonstrated with a cloud of $^{171}Yb^{+}$. Chapter 4 looks into detection of image currents on the trap electrodes resulting from deliberately excited ion oscillations, and issues relating to the detection methods.

Chapter 5 focuses on two power law noise models which could potentially allow Bayesian filtering to be applied to systems with power law noise. Very often when addressing power law noises, a frequency domain approach such as power spectral density is adopted to study them. In this chapter we start from the frequency domain by modeling the power law noise for a given band of frequencies, then transform the models from frequency to time domain as state space models which are compatible with Bayesian estimation. The state space models appear to have a similar structure with Gaussian mixture models (GMMs) which are often used for estimation in non-Gaussian probability distributions and work very well with Bayesian estimation. Chapter 6 concludes this work.

Chapter 2

Ion Trapping with Quadrupole Fields

The earliest ion traps were developed in the 1950's and 1960's by Wolfgang Paul [7] and Hans Dehmelt [8]. Over time, ion traps proved to be very useful tools for studying various physical systems including quantum information processors [9–11], quantum simulators [20, 21], ion cavity QED [22, 23], frequency standards [12, 13]. This chapter outlines some of the concepts involved in the trapping of atomic or molecular ions with quadrupole fields. In section 2.1 we summarize the equations of motion of a trapped ion in a linear Paul trap. These equations of motion for trapped ions are helpful in choosing trap parameters which lead to stable trapping of ions. We also elaborate on the generation of quadrupole fields necessary for trapping. Section 2.2 discusses the assembly and alignment of our linear Paul trap components. The theory behind potential generation is covered in section 2.3 which focuses more on resonator concepts and briefly touches on impedance matching. Section 2.4 discusses the design and implementation of a helical resonator.

2.1 Quadrupole Field Traps

This section presents a brief review on the dynamics and stability of the ion confined by the quadrupole fields.

2.1.1 Earnshaw's Theorem

Earnshaw's theorem tells us that a charged particle cannot be stably confined in stationery equilibrium using only electrostatic fields. That is, according to this theorem it is impossible to trap ions in a stable spatial equilibrium using only static electric fields, so either a combination of electric and magnetic fields could be used (i.e Penning traps) or a time-varying electric field could be used (i.e. Paul traps) [24]. This can be illustrated with an example of a charged particle supposedly trapped in a three dimensional harmonic electric potential of the following form [25],

$$\Phi(x,y,z) = \alpha x^2 + \beta y^2 + \gamma z^2 \tag{2.1}$$

The corresponding electric field,

$$\mathbf{E}(x,y,z) = -\nabla\Phi(x,y,z) = -2\begin{bmatrix}\alpha x & \beta y & \gamma z\end{bmatrix}^{\dagger} \tag{2.2}$$

According to Maxwell's equation the divergence of electric field in the absence of charge vanishes, that is,

$$\nabla\cdot\mathbf{E}(x,y,z) = -2(\alpha+\beta+\gamma) = 0 \tag{2.3}$$

This divergence implies that one of the components of the field has to be non-confining whenever the other two are confining. To prevent a charged particle from escaping along the non-confining field direction, the fields must be switched back and forth to alternate between confinement and non-confinement thus, resulting in trapping with electrodynamic fields.

2.1.2 Linear Paul Trap

A schematic of a linear Paul trap is shown in Fig. 2.1 below with axes and electrodes labeled.

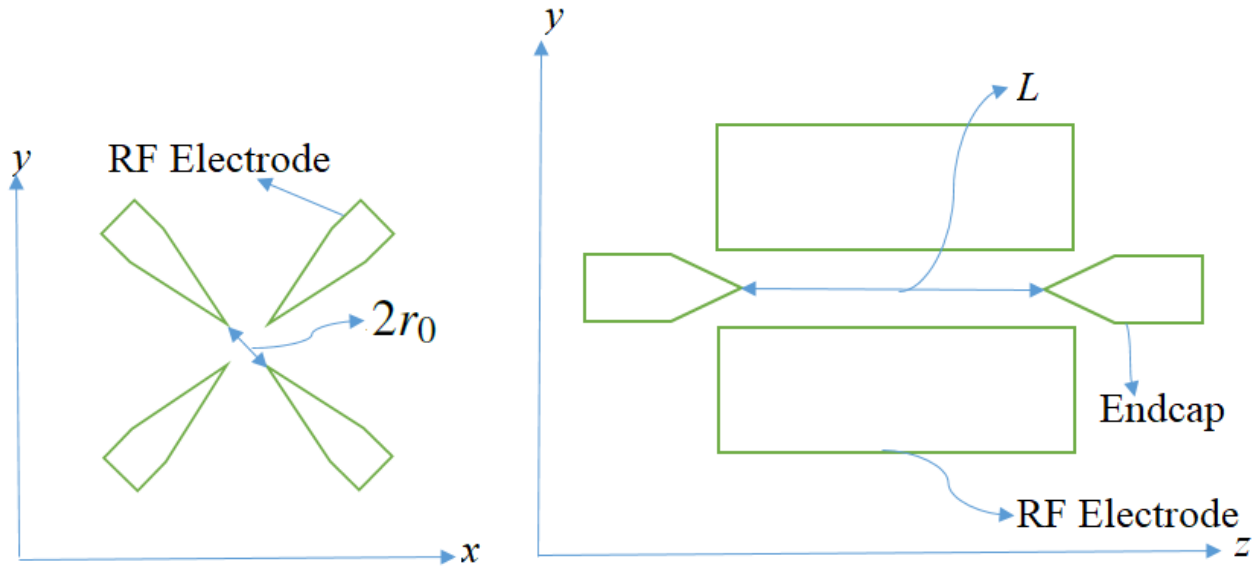

Fig. 2.1: A schematic diagram of a linear Paul trap's cross-sectional view (left) and lateral view (right).

In the schematic diagram above, the xy-plane is also referred to as the radial plane while z-axis is referred to as the trap axis. Compensation electrodes used for biasing the trap are not shown in this schematic diagram. An actual picture of our linear Paul trap is shown in Fig. 2.2 below. In this picture the top compensation electrode can be seen help down with bolts on the trap frame.

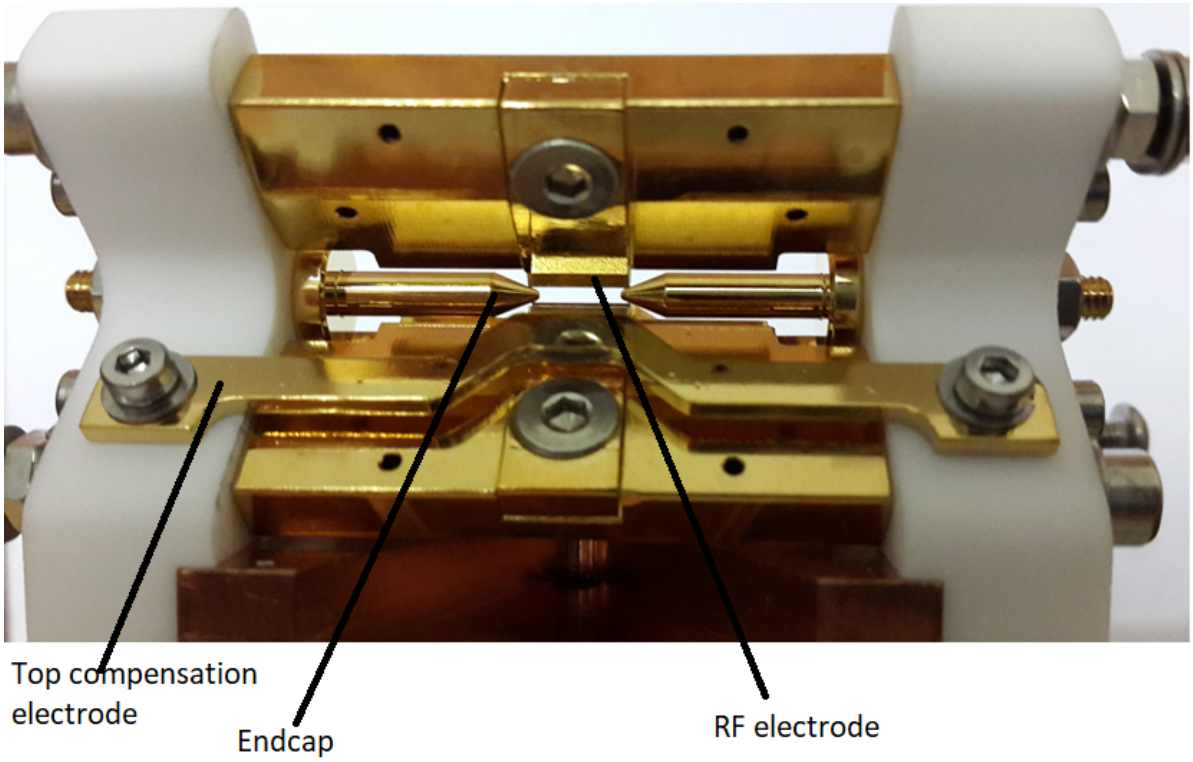

Fig. 2.2: A picture of our actual linear Paul trap.

A linear Paul trap produces a harmonic electric potential with a static and time-varying components as shown below [25],

$$\Phi(\mathbf{r},t) = \Phi_{RF}(\mathbf{r},t) + \Phi_{EC}(\mathbf{r}) \tag{2.4}$$

with $\Phi_{RF}(\mathbf{r},t)$ and $\Phi_{EC}(\mathbf{r})$ being,

$$\begin{aligned} \Phi_{RF}(\mathbf{r},t) &= V_{RF}\frac{(x^2-y^2)}{2r_0^2}\cos(\Omega t) \\ \Phi_{EC}(\mathbf{r}) &= \frac{V_{EC}}{L^2}(2z^2-x^2-y^2) \end{aligned} \tag{2.5}$$

2.1.3 Trapped Ion Dynamics

The resulting Matthieu equations below govern the motion of a trapped ion [25],

$$\begin{aligned} \frac{d^2x}{d\tau^2} &= -(a-2q\cos(2\tau))x \\ \frac{d^2y}{d\tau^2} &= -(a+2q\cos(2\tau))y \\ \frac{d^2z}{d\tau^2} &= -2az \end{aligned} \tag{2.6}$$

with

$$\begin{aligned} \tau &= \tfrac{1}{2}\Omega t \\ a &= \frac{e\kappa V_{EC}}{mL^2\Omega^2} \\ q &= \frac{2eV_{RF}}{mr_0^2\Omega^2} \end{aligned} \tag{2.7}$$

where Ω and V_{RF} are the angular frequency and amplitude of the radio frequency drive respectively, e and m are the charge and mass of the trapped particle respectively, V_{EC} is the static endcap potential, L is endcap to endcap spacing and $2r_0$ define the spacing between two diagonal rf electrodes. A dimensionless factor κ accounts for geometrical imperfections of the endcaps which lead to experimental deviations from pure quadrupole field [25]. The electric potential inside the trap resembles a saddle rotating at the rf drive frequency Ω.

2.1.4 Frequencies of Motion

The exact solution to the Matthieu equations above take the following form, as outlined in [1],

$$u(\tau) = A\sum_{n=-\infty}^{\infty} C_{2n}\cos(\beta+2n)\tau + B\sum_{n=-\infty}^{\infty} C_{2n}\sin(\beta+2n)\tau \tag{2.8}$$

where A and B are constants dictated by initial conditions. The coefficients C_{2n} are the amplitudes for the Fourier components of the particle motion which decrease with increasing n. The frequency of motion in the i^{th} dimension is given by,

$$\omega_i = \beta_i\Omega, \text{ for } i \in \{x,y,z\} \tag{2.9}$$

where the exact value of β_i is expressed by the following continued fraction form [1, 26],

$$\beta_i^2 = a_i + \frac{q_i^2}{(\beta_i+2)^2 - a_i - \frac{q_i^2}{(\beta_i+4)^2-a_i-\frac{q_i^2}{(\beta_i+6)^2-a_i-\cdots}}} + \frac{q_i^2}{(\beta_i-2)^2 - a_i - \frac{q_i^2}{(\beta_i-4)^2-a_i-\frac{q_i^2}{(\beta_i-6)^2-a_i-\cdots}}} \tag{2.10}$$

However, the adiabatic approximation, ($q_i < 0.4$ and $a_i \ll q_i$) is sufficient in most practical cases and yields the following,

$$u(\tau) = R_i\cos(\frac{2\omega_i\tau}{\Omega})(1+\frac{q_i}{2}\cos(2\tau)) \tag{2.11}$$

where $\omega_i = \beta_i \Omega$ and $\beta_i = \sqrt{\frac{q_i^2}{2} + a_i}$ with $q_y = -q_x = q$, $q_z = 0$ and $a_z = -2a_x = -2a_y = -2a$ [26].

The solution of the axial component of the equation of motion is simply a harmonic oscillator with axial trap frequency ω_z. On the other hand the radial components lead to a solution which has two modes of oscillation; one at the trap/secular frequency ω_r while the other, called micromotion, is at the rf drive frequency. The trap frequencies are given by [1, 25],

$$\begin{aligned} \omega_z &= \frac{\Omega}{2}\sqrt{2a} \\ \omega_r &= \frac{\Omega}{2}\sqrt{\frac{q^2}{2} - a} \end{aligned} \tag{2.12}$$

In our lab experiments we were not able to definitively pin down the precise values of these secular frequencies due to the bad vacuum conditions which led to the loss of trapped ions. Despite not being able to report the results of the secular frequencies, we will briefly summarize the procedure we used to look for these frequencies. The idea was to trap as few ions as possible and then apply an additional RF voltage on the trap electrodes as a frequency which is swept slowly over a wide enough range, centered at the anticipated secular frequency. When the frequency of this additional RF voltage is swept past the secular frequency the trapped ions would be driven on resonance and their fluorescence diminishes. This effect was observed in our experimental trials but with a large cloud of ions rather than few ions. With a cloud of ions once could have been exciting the center of mass mode or other modes and as such the obtained frequencies would not necessarily be secular frequencies we are interested in. The results are therefore, not reported here. It is left as future work attempt this experiment again when the vacuum is better.

2.1.5 Trap Stability

The stability of Matthieu equations shown in the previous sections is determined by the values of a and q. The stability regions can also be shown graphically as shown in Fig. 2.3 below [1, 26].

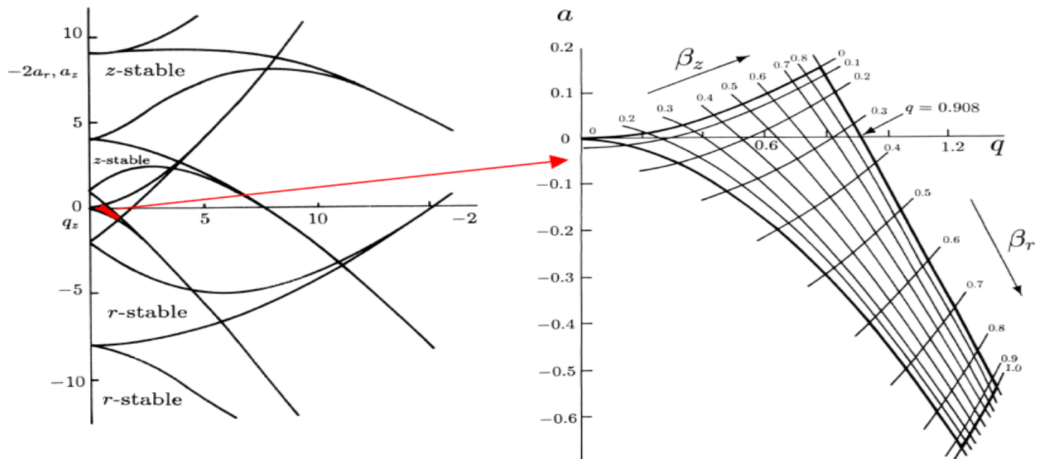

Fig. 2.3: Stability map of a linear ion trap [1].

The overlapping regions in the stability map are regions where the stability is achieved both axially, z and radially, r [1,26]. The a and q parameters can be varied conveniently by changing the trap frequency or rf and dc voltages applied to the trap electrodes. This tuning of ion trap parameters is essential when relaxing and tightening the trap strength during the experiments. Linear Paul traps are typically operated with a q value below unity in order to keep excess micromotion reasonably small [25].

2.1.6 Excess Micromotion

The solution of the radial components of Matthieu equation has the fast oscillatory component superimposed upon the slow secular motion. This fast oscillatory component of the solution is in sync with the rf drive frequency and is termed micromotion and its presence is necessary for the trapping of particles even though one seeks to minimize its amplitude because it adds unwanted spectroscopic features [25]. In the case whereby the ion's axial trapping field is not aligned with the rf quadrupole field axis, or if there exists a phase difference between rf trap electrodes, there will be excess micromotion which needs to be compensated [27]. There are techniques used to compensate for the micromotion however, those are beyond the scope of what we wish to report in this work. Additional electrodes called compensation electrodes (see Fig. 2.4) are made specifically for handling excess micromotion as well as shifting the null of the trap.

2.2 Linear Paul Trap Design

There are different designs of ion traps, each of which is suited for some particular purpose. For instance, chip or microfabricated ion traps [28, 29] are well-suited for quantum information processing which require large arrays of traps to scale up information capacity. In some designs the ion trap is placed in an optical cavity and this boosts the fidelity and speed of the trapped ion qubit measurement through the Purcell effect [30,31]. There are approaches for ion trap designs with enhanced optical access including traps with one ring electrode or two opposing endcap electrodes or even planar trap geometries. The authors in [32] present a design of an ion trap combined with a reflective parabolic surface with trap electrodes, thus, enhancing the efficiency of fluorescence collection. This parabolic trap design covers a solid angle of 2π steradians, and allows precise ion placement at the focal point of the parabola [32].

Our trap is a linear Paul trap generating quadrupole fields with four rf electrodes radially and two dc electrodes axially. Our trap bears similarities to that used in the group of Rainer Blatt, and has good optical access with end cap electrodes designed to shield the exposed dielectric surfaces. It was constructed out of gold coated, oxygen free copper. In our version the rf electrodes are 200 μm thick copper sheets clamped to a stronger support. Figure 2.4 shows the trap design in CAD environment.

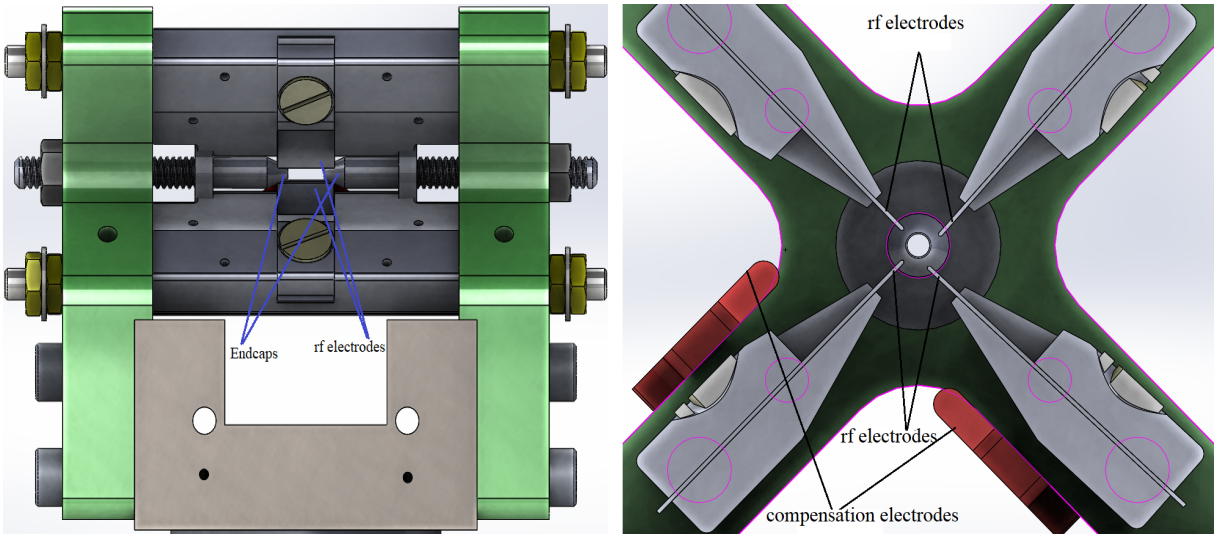

Fig. 2.4: A picture of side view (left) and cross-sectional view (right) of our trap design in CAD environment.

There were no specific values of stability parameters (a and q) aimed for during the design of our design. This is primarily because we needed to be able to vary these stability parameters during experiments such that we can investigate different trapping points (stable and unstable) on the stability map. The choice was made to set the design parameters as follows;

- Separation of diagonal RF electrode: $2r_0 = 1$ mm
- Axial length of the trap (Endcap to endcap): $L = 5$ mm
- RF drive frequency range:$2\pi(15\text{ MHz}) \leq \Omega \leq 2\pi(20\text{ MHz})$
- Leave V_{EC} and V_{RF} to vary as much as possible.
- Ytterbium had been chosen as the atom to create ions from hence charge to mass ratio e/m was already decided.

With this set of choices, it is clear that stability parameters (a and q) will be adjusted using the tunable voltages V_{EC} and V_{RF} respectively. One limitation in the choice of trap dimensions was that for the same stability point at a chosen operating frequency, large trap would require high voltages and that is expensive. The other limitations in our case was that a smaller trap would be tedious to align properly during assembly as we did all that manually under the microscope. The following sections covers the alignment of electrodes and measurements of electrode separations taken.

2.2.1 Electrode Alignment

The rf electrodes were positioned using a reference copper block which allowed only a prescribed length of the electrode to protrude out from its mounting platform. The electrodes were then tied down with bolts to secure them in their respective positions. The four rf electrodes holders, end caps and the

compensation electrodes were all assembled and held in place with stainless steel bolts on the ceramic frame and the base copper block to give a rigid structure. For finer adjustments of the rf and end cap electrodes orientation, the trap was placed under the microscope and tweaked with forceps while some bolts were slightly loosened and re-tightened when the electrode is in place. Fig. 2.5 shows the top view of trap electrodes seen under the microscope.

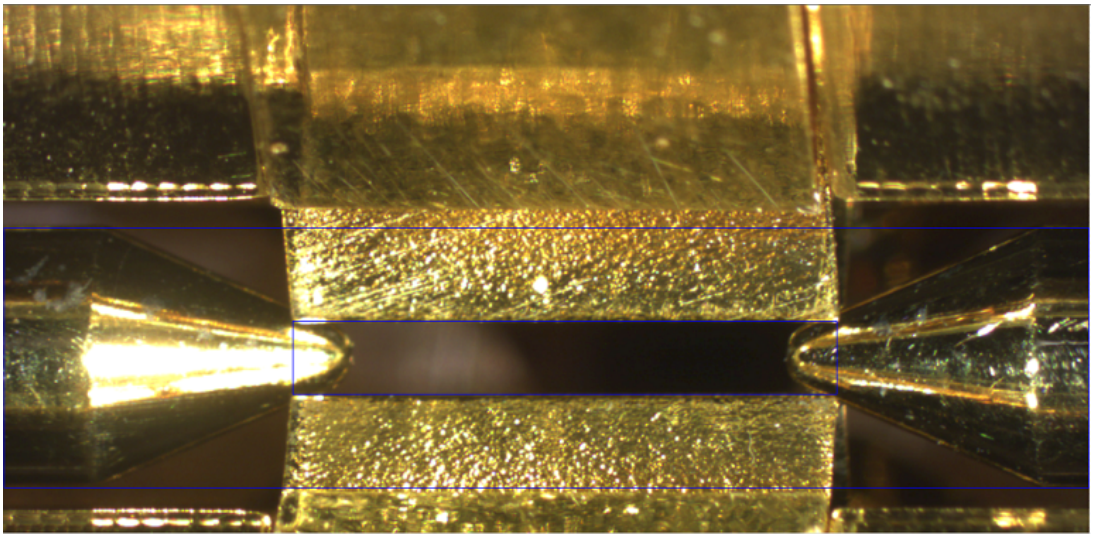

Fig. 2.5: Top view of our linear Paul trap as seen under the microscope.

The blue rectangles are part of the tools from the microscope software that were useful in detecting and correcting the skewness of rf and end cap electrodes relative to one another. Fig. 2.6 below shows the side view of the trap electrodes as seen under the microscope after tweaking.

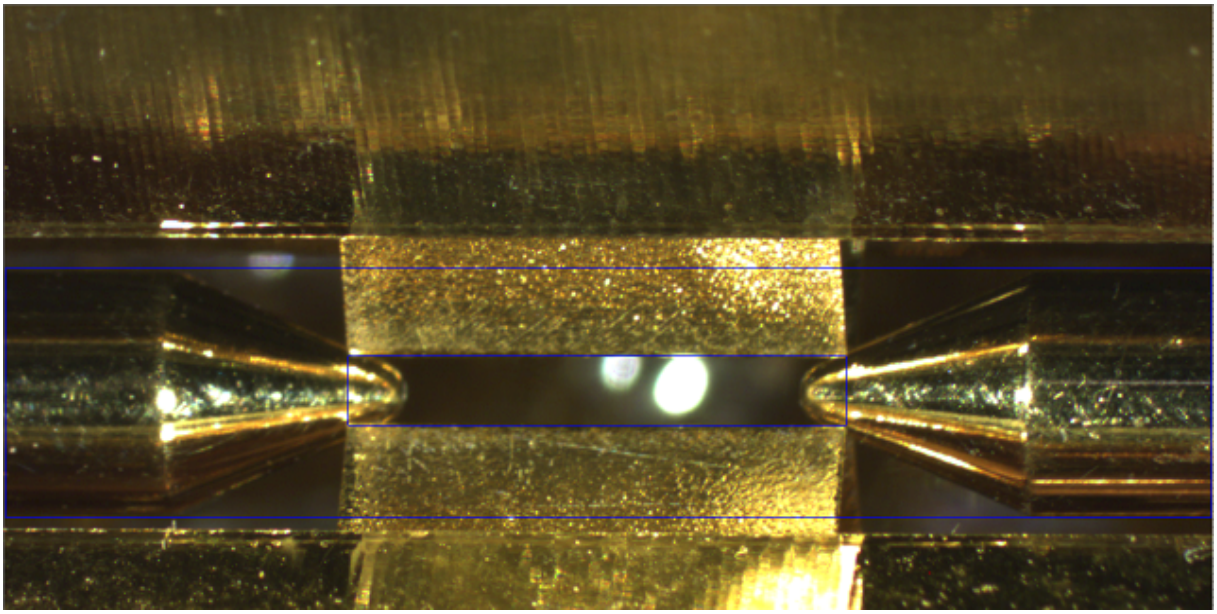

Fig. 2.6: Side view of our linear Paul trap as seen under the microscope.

After the tweaking process under the microscope we mounted the whole trap setup on a translation stage and used the 369 nm laser beam to measure the separation between end caps and the separation between adjacent rf electrodes on two sides of the trap. We moved the trap on the translation stage horizontally

and vertically, perpendicular to the laser beam direction, and recorded the micrometer reading upon reaching positions where half of maximum laser beam power passed through while the other half was blocked by the electrode. Following this procedure, the separation between the two end caps was found to be 5.06 mm as shown in Table 2.1 below.

Table 2.1: Laser coming from side 2 to side 1 of the trap.

Endcap 1	Endcap 2	Endcap separation
17.212 mm	12.150 mm	5.062 mm

Table 2.2 below shows the differences in the two endcap positions and the separation between rf blades as seen from the side with the trap sitting upright and laser beam going from side 2 to side 1 of the trap.

Table 2.2: Laser beam from side 2 to side 1 of the trap in upright orientation.

Endcap (EC)	Top rf Blade	EC Top side	EC Bottom side	Bottom rf Blade	rf Blade separation
1	22.974 mm	22.757 mm	22.316 mm	22.142 mm	0.832 mm
2	23.005 mm	22.832 mm	22.300 mm	22.184 mm	0.821 mm

From the measurement data in the table, a virtual line joining the two endcaps is angled by no more than 0.334° to the assumed horizontal. This is an overestimation since the measurements from one endcap to the other was greater than 5.062 mm but for estimating the deviation angles we used the separation of 5.062 mm to set a loose upper bound. With respect to the same horizontal the top and bottom rf blades are angled by no more than 0.351° and 0.476° respectively. Hence the relative deviation between the two rf blades as seen from side 2 of the trap is no greater than 0.125°. Table 2.3 below shows the differences in the two endcap positions and the separation between rf blades as seen from the side with the trap sitting upright and laser beam going from side 1 to side 2 of the trap.

Table 2.3: Laser beam from side 1 to side 2 of the trap. Trap sitting upright on the translation stage.

Endcap (EC)	Top rf Blade	EC Top side	EC Bottom side	Bottom rf Blade	rf Blade separation
1	23.002 mm	22.922 mm	22.260 mm	22.212 mm	0.790 mm
2	22.983 mm	22.820 mm	22.315 mm	22.205 mm	0.778 mm

From the measurement data in the table, a virtual line joining the two endcaps is angled by no greater than 0.266° to the assumed horizontal. With respect to the same horizontal, the top and bottom rf blades are angled by no more than 0.216° and 0.080° respectively. Hence the relative deviation between the two rf blades as seen from side 1 of the trap is no greater than 0.137°. Table 2.4 below shows the differences in the two endcap positions and the separation between rf blades as seen from the top with the trap sitting on the side and laser beam going from top to bottom of the trap.

Table 2.4: Laser beam from side 2 to side 1 of the trap. Trap sitting up-side down on the translation stage.

Endcap (EC)	Top rf Blade	EC Top side	EC Bottom side	Bottom rf Blade	rf Blade separation
1	4.640 mm	4.520 mm	3.908 mm	3.815 mm	0.825 mm
2	4.641 mm	4.491 mm	3.975 mm	3.851 mm	0.790 mm

From the measurement data in the table, a virtual line joining the two endcaps is angled by no greater than 0.216° to the assumed horizontal. With respect to the same horizontal, the top and bottom rf blades are angled by no more than 0.012° and 0.408°respectively. Hence the relative deviation between the two rf blades as seen from the side 2 in an up-side down orientation of the trap is no greater than 0.397°. Table 2.5 below shows the differences in the two endcap positions and the separation between rf blades as seen from the bottom with the trap sitting on the side and laser beam going from bottom to top of the trap.

Table 2.5: Laser beam from side 1 to side 2 of the trap. Trap sitting up-side down on the translation stage.

Endcap (EC)	Top rf Blade	EC Top side	EC Bottom side	Bottom rf Blade	rf Blade separation
1	5.055 mm	4.887 mm	4.371 mm	4.205 mm	0.850 mm
2	4.962 mm	4.760 mm	4.412 mm	4.188 mm	0.774 mm

From the measurement data in the table, a virtual line joining the two endcaps is angled by no greater than 0.487° to the assumed horizontal. With respect to the same horizontal the top and bottom rf blades are angled by no more than 1.053° and 0.193° respectively. Hence the relative deviation between the two rf blades as seen from the side 1 in an up-side down orientation of the trap is no greater than 0.861°.

2.2.2 Trap Wiring and Mounting

After alignment of the ion trap electrodes the trap was mounted and clamped with screws on the rails inside the vacuum chamber as shown in Fig. 2.7 below.

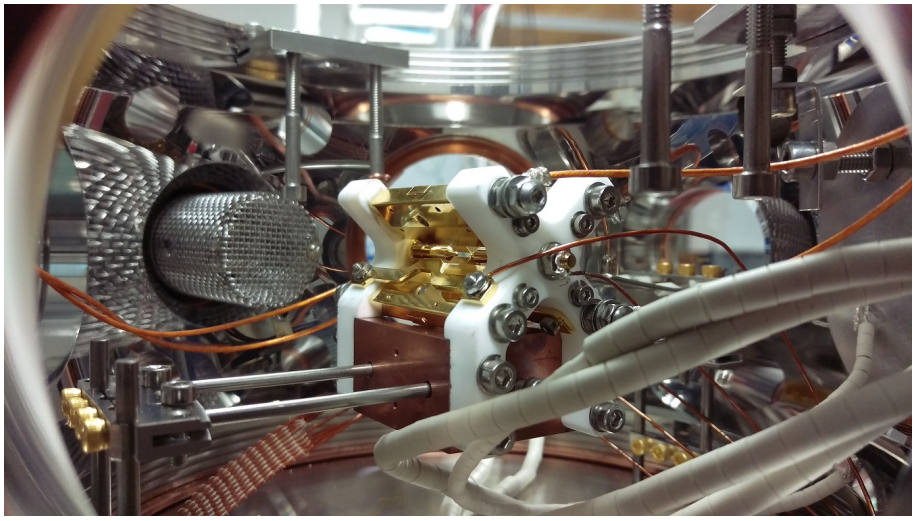

Fig. 2.7: The ion trap inside the vacuum chamber with the wiring to all the electrodes.

Steatite ceramic beads were used to provide insulation to the bare wires to reduce chances of unwanted shortcircuits.

2.3 RF Potential Generation

Equation set (2.7) in the previous section shows how the trapping stability parameters (a and q) relate to different quantities such static and rf voltage, rf frequency, trap dimensions as well as charge to mass ratio. Fig. 2.3 shows the plot or map of values of trapping stability parameters which lead to stable trapping of ions. Now this means the choice of quantities like voltages, frequency, trap dimensions and choice atomic ion can determine whether the ion is stably trapped or not. In our design we seek the choice of values of these quantities which will allow us to vary the trapping parameters as much as possible in order for us to later on map out the stability map of our own trap. Notice that once can choose fixed values of all other quantities and leave only voltages to be varied and still be able to move a and q through the entire stability map provided the voltage supplies have a wide enough voltage range. This is precisely what we did in our case and this shifts the design problem to building voltage supplies which can go as high as possible and provides noise-free voltage to the trap electrodes. This section addresses the generation of voltage that is clean and reasonably high.

Trapping ions with a linear Paul trap requires a stable static and radio frequency (rf) potential supplies with sufficiently high amplitudes and minimal noise [33]. The dc voltage supply is pretty straightforward to assemble from commercial high voltage power supplies hence the focus of this chapter is mostly on rf potential generation. There are various ways of generating clean high amplitude rf voltage depending on specific needs and available tools. For instance, in the absence of rf sources, an oscillator with these desired properties, needs to be implemented. Alternatively, in the presence of low voltage rf sources, filters, amplifiers and/or resonators would suffice for the generation of high amplitude clean rf voltages. In our case we assume the presence of a low voltage broadband rf source thus, both amplification and filtering are required to obtain the desired high amplitude clean rf voltage.

One of the important factors, with regard to ion trapping, is the stability of the supplied rf voltage. This stability can be looked at in terms of the deviations in amplitude and frequency of the voltage supplied to the trap electrode by the resonator setup. If the resonance frequency of the resonator is drifting in time, this can affect the amplitude of the supplied voltage. The same thing happens if the source frequency is drifting in time. In ion trapping it is common to use helical resonator as a means to filter and step up the voltage [33–35]. An active stabilization of the helical resonator potential by means of measurement feedback (closed loop control) is presented in [35]. A non-intrusive measurement for feedback is achieved by capacitively coupling out (weak coupling) a small fraction of the resonator output.

The other important thing concerns the efficient transfer of power from the source to the load (i.e. ion trap). Efficient power transfer is possible only in the case whereby the source output impedance is matched to the load input impedance [34–38]. It is possible to use amplifiers and filters to obtain a clean high voltage signal and impedance matching, but the common approach is to use a resonant filter since it can offer voltage amplification, filtering and impedance matching at a go. In the next section we briefly discuss the concepts of resonance and impedance matching. The rest of the chapter outlines the design, implementation and testing of the helical resonator.

2.3.1 Resonator Theory

As mentioned above the required voltages for trapping need to be noise-free to avoid heating up the ions. A resonator can be used to achieve the goal of filtering out the noise that may be present in the voltage from the source or amplifier. A resonator can be thought of as a system that naturally oscillates at some specific frequencies with greater amplitude than at others upon excitation [39]. These specific frequencies are called resonant/natural frequencies ω_n. The oscillations in a resonator can be mechanical, acoustic or electromagnetic however, in this chapter we focus on electrical resonators for ion trapping purposes. As mentioned in [40], most resonators can be adequately approximated by a second order linear time-invariant system which can be represented as second order ordinary differential equation such as the one shown below:

$$y'' + \frac{\omega_n}{Q}y' + \omega_n^2 y = au'' + bu' + c\omega_n^2 u \tag{2.13}$$

In this equation, $u(t)$ and $y(t)$ are the input and output signals respectively, Q is the quality factor (Q - factor), a measure of how damped the system is or the selectivity in frequency of the system. The low frequency gain c controls the low pass filtering behavior independent of resonance while a and b are the gains associated with high pass filtering and band pass filtering respectively. Sometimes it is more convenient to do analysis and system identification in the frequency domain rather than time domain, since signal operations are easier in the frequency domain. In such cases the transfer function representation and perhaps the associated graphical frequency domain representations like Bode diagrams and Nyquist plots of the system become more useful, especially for system identification. Applying Laplace transform on equation (2.13) and setting initial conditions to zero we get:

$$\begin{aligned}
\mathscr{L}\{y'' + \tfrac{\omega_n}{Q}y' + \omega_n^2 y\} &= \mathscr{L}\{au'' + bu' + c\omega_n^2 u\} \\
&\Downarrow \\
s^2Y(s) + \tfrac{\omega_n}{Q}sY(s) + \omega_n^2 Y(s) &= as^2U(s) + bsU(s) + c\omega_n^2 U(s) \\
&\Downarrow \\
(s^2 + \tfrac{\omega_n}{Q}s + \omega_n^2)Y(s) &= (as^2 + bs + c\omega_n^2)U(s)
\end{aligned} \tag{2.14}$$

with $U(s) = \mathscr{L}\{u(t)\}$ and $Y(s) = \mathscr{L}\{y(t)\}$. The resulting transfer function of the above system is given below as:

$$G(s) = \frac{Y(s)}{U(s)} = \frac{as^2 + bs + c\omega_n^2}{s^2 + \frac{\omega_n}{Q}s + \omega_n^2} \tag{2.15}$$

Where $G(s)$ is the system's gain and s is the complex Laplace parameter (i.e. $s = \sigma + i\omega$). A Bode plot is the graphical representation of the system transfer function magnitude $|G(s = i\omega)|$ and phase $\angle G(s = i\omega)$ against frequency ω. The magnitude and phase of $G(s)$ in terms of the frequency are shown below;

$$\begin{aligned} |G(i\omega)| &= \frac{\sqrt{(c\omega_n^2 - a\omega^2)^2 + b^2\omega^2}}{\sqrt{(\omega_n^2 - \omega^2)^2 + (\frac{\omega_n\omega}{Q})^2}} \\ \angle G(i\omega) &= arctan(\frac{b\omega(\omega_n^2 - \omega^2) - \frac{\omega_n}{Q}(c\omega_n^2 - a\omega^2)}{(\omega_n^2 - \omega^2)(c\omega_n^2 - a\omega^2) + \frac{b\omega_n\omega}{Q}}) \end{aligned} \tag{2.16}$$

Rewriting the magnitude in decibels (dB) leads to greater simplification as shown below;

$$|G(i\omega)|_{dB} = 10log((c\omega - a\omega^2)^2 + b^2\omega^2) - 10log((\omega_n^2 - \omega^2)^2 + (\frac{\omega_n\omega}{Q})^2) \tag{2.17}$$

At resonance $(\omega = \omega_n)$ the magnitude is given by;

$$|G(i\omega_n)|_{dB} = 10log((c-a)^2 + \frac{b^2}{\omega^2}) + 20log(Q) \tag{2.18}$$

The first logarithmic term in equation (2.18) above refers to the gain of the system without considering resonance effects. If $a = b = 0$ this first term becomes just $20log(c)$ which simply means that at low frequencies the gain of the system is c, which is also called DC gain. At high frequencies the gain approaches zero hence this setup act as a low-pass filter. On the other hand if only $b = 0$ the configuration results in a band-stop filter. If $b = c = 0$ we would have a high-pass filter or if $a = c = 0$ we have a band-pass filter configuration. Lastly if all the three gains nonzero then we have an all-pass filter. The second term, $20log(Q)$, in equation (2.18) above refers to the gain of the system contributed solely by resonance and it can be seen from this term that the gain contributed by resonance has magnitude Q at resonance.

The common types of electrical resonators are lumped element resonators, distributed resonators and quasi-lumped element resonators, such as a helical resonator [34]. The lumped element resonators are those made of common electrical circuit components such as resistors R, inductors L, capacitors C and perhaps some active components like transistors. For sufficiently high frequencies whereby a quarter of an operating wavelength is a reasonable length for a resonator physical size, transmission line resonators are a good option. Transmission line resonators have a higher selectivity compared to the lumped element resonators. In passive resonator circuits, the circuit resistance places a limit on how high the selectivity (Q - factor) of the resonator can be. However, in active circuits this limitation can be overcome in several ways such as simulating a negative resistance or by introducing the concept of positive feedback in the circuit. The next section gives a brief outline of the positive feedback concept applied to resonator design and some practical issues associated.

2.3.2 Positive Feedback Concept

Looking at the resonator theory in the previous section from the perspective of control systems engineering, one can immediately realize that there is an obvious way of improving the quality factor of the resonator by simply implementing a positive feedback loop. This is done with an intent to drive the poles

of the transfer function (equation (2.15)) to sit as close as possible to the imaginary line (i.e. marginal stability line). In this way the poles will have almost zero real-part which means achieving a minimized damping effect and therefore, high selectivity. This thought exercise is presented next together with the practical challenges that come with it.

In this section we present an alternative approach to building a low voltage high Q - factor resonator and this is based on common engineering knowledge of classical control systems modeled in Laplace (or frequency) domain. This approach makes use of the complex pole placement through positive feedback and therefore, allowing the poles of the filter to be placed at any desired positions in principle. There are many open loop transfer function models whose closed loop poles can be placed in a way that improves the closed loop Q - factor relative to open loop. In this discussion we choose our open loop model as a second order band-pass filter conveniently, because it allows one to tune the Q - factor without affecting resonance frequency ω_n in closed loop. The general second order resonant band pass filter has the following transfer function;

$$G(s) = \frac{b\frac{\omega_n}{Q}s}{s^2+\frac{\omega_n}{Q}s+\omega_n^2} \tag{2.19}$$

The roots of the characteristic polynomial in denominator of equation (2.19) above are the poles while the root of the numerator polynomial are the zeros of the filter. The most common way of closing the loop in control systems design is through negative feedback which reduces the open loop gain and lead to stable dynamics in most cases. Applying the negative feedback on equation (2.19) increases the phase and gain margins leading to faster poles and hence fast damping. This translates to lowering the Q - factor of the filter and that is not our intention here. On the other hand, positive feedback leads to slower poles which yield higher Q - factor. We aim to drive the real part of the poles of this filter towards zero (*marginal stability condition*) in order for the resonator to sustain oscillations for a longer time without significant damping. Using positive feedback to close the loop results in the following closed loop transfer function:

$$H(s) = \frac{G(s)}{1-G(s)} = \frac{b\frac{\omega_n}{Q}s}{s^2+(1-b)\frac{\omega_n}{Q}s+\omega_n^2} \tag{2.20}$$

From equation (2.20) above the closed loop Q - factor is $\frac{Q}{1-b}$, hence by varying the band-pass gain b the closed loop Q - factor can be tuned to a desired operating value. As will be seen in the proposed simple circuit, b can be associated with a variable resistor. A way to realize this closed loop transfer function in electrical circuits is by using active elements such as the operational amplifiers and some assisting passive elements as shown in Fig. 2.8 below. The most serious disadvantage of using op-amps is the conflict between gain and bandwidth of op amp-based circuits.

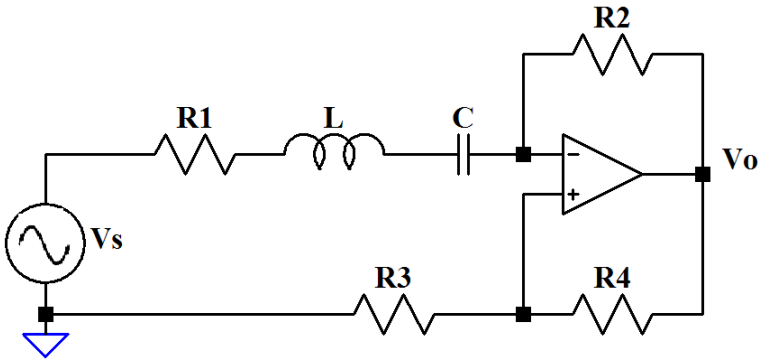

Fig. 2.8: Op-amp based second order band-pass filter circuit.

The resulting closed loop transfer function $H(s)$ relating input voltage V_s and output voltage V_o is given by

$$H(s) = \frac{-2b\frac{R}{L}s}{s^2+(1-b)\frac{R}{L}s+\frac{1}{LC}} \tag{2.21}$$

with all resistors re-written in terms of $R_1 = R$ as $R_3 = R_4 = nR_1$, $R_2 = bR_1$. It is obvious that setting $b = 1$ makes the closed loop transfer function marginal stable, a condition corresponding to infinite Q - factor or zero bandwidth. Such a strict filter selectivity comes at the cost of infinite gain bandwidth product requirement at resonance, that is the closed loop gain magnitude, $\left|\frac{-2b}{1-b}\right|$approaches infinity as the open loop gain b approaches one. For an op amp this is bad news since with its limited gain-bandwidth product the required gain at resonance frequency cannot be met and likewise the required bandwidth, at very high gains, does not cover the desired resonance frequency. In either case the desired dynamics are not realized in practice, therefore, the limit to how close to unity b can get is set by the gain-bandwidth product of the available components. In the figure below we show the simulation of the circuit above under low and high gain-bandwidth product to illustrate the distortion arising from limited gain-bandwidth product.

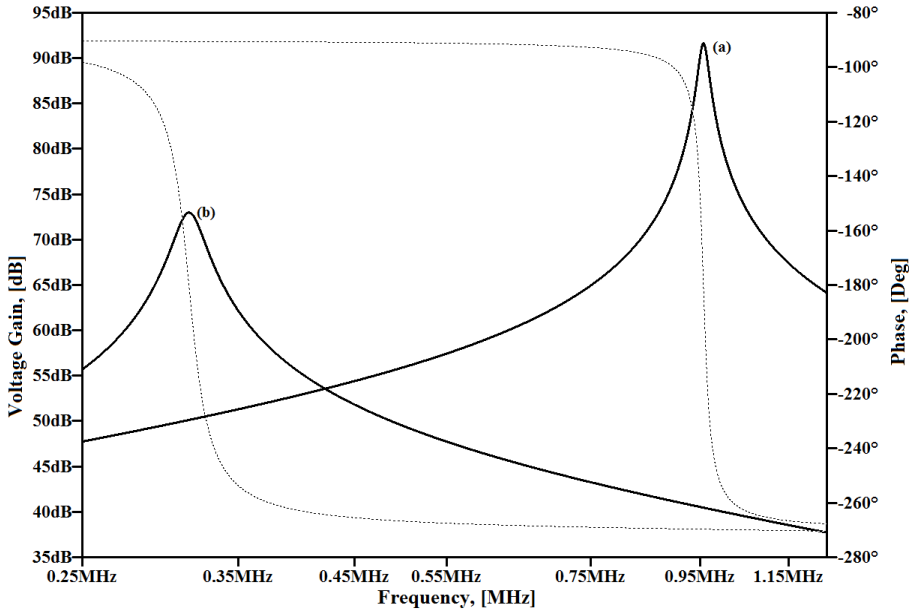

Fig. 2.9: (a) High gain-bandwidth product 1 GHz, (b) Low gain-bandwidth product 10 MHz.

The resonance frequency was set by the choice of $L = 7$ uH and $C = 3.62$ nF to 1 MHz as evident in the Fig. 2.9 response (a) above and the open loop gain parameter b was set to 0.999. With the resistance R set to 1 KΩ, the expected Q - factor is 44. Using an op-amp with gain-bandwidth product of 1 GHz results in a resonance frequency of 0.958 MHz and quality factor (or selectivity) of 42.33 as shown in Fig. 2.9 response (a). There is a slight shift from the expected theoretical figures. The effect of limited gain-bandwidth product can be clearly illustrated by lowering it significantly from 1 GHz setting.

Notice how the filter response changes both resonance frequency and selectivity once we limit the gain-bandwidth product to 10 MHz in Fig. 2.9 response (b). Here the resonance frequency is 0.315 MHz and the selectivity is only 15.71 which is a significant shift from the expected figures. It is evident then that limited gain-bandwidth product of a device does alter the dynamics of the system. There are op-amps with reasonably high gain-bandwidth product however, they are typically low voltage devices which cannot offer sufficiently high voltage output, required in high voltage applications such as ion trapping, without an additional voltage amplification stage. A resonator like this one can perhaps be suitable in low frequency centimeter scale ion traps for filtering mostly. This approach of designing resonators can offer substantial improvement on Q - factor, however, the cheaper ways using only passive elements are usually preferred in practice. Alternatively, transistors, as opposed to op-amps, can be used to realize this positive feedback concept at higher frequencies.

2.3.3 Impedance Matching

In most electrical circuit applications one is faced with the challenge of optimizing power transfer from one point (*source*) to another (*load*) in the circuit. This helps avoid back-reflection which in our case caused an interference on our camera screen. Impedance matching can be explained by considering a simple potential divider like the one shown in Fig. 2.10.

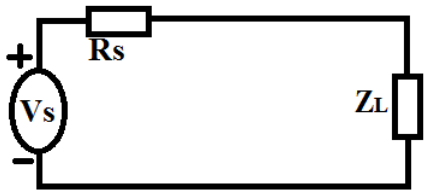

Fig. 2.10: Impedance matching demonstration.

The power P_L delivered to the load Z_L by a source V_s, with internal resistance R_s is given by:

$$P_L = \frac{Z_L}{(R_s + Z_L)^2} V_s^2 \tag{2.22}$$

To find the maximum power delivered to the source, one can just find the extremum of load power P_L with respect to variation of load impedance Z_L. That is similar to asking which load impedance provides maximum power transfer from source to load. Taking the first derivative of equation (18) one gets:

$$\frac{\partial P_L}{\partial Z_L} = \frac{(R_s - Z_L)}{(R_s + Z_L)^3} V_s^2 \tag{2.23}$$

Equating equation (19) to zero and solving for Z_L leads to the following solution:

$$Z_L = R_s \tag{2.24}$$

This means for maximum power transfer to the load the equivalent impedance observed from the load when looking towards the source must be equal or matched to that of the load itself. Fig. 2.11 shows a plot of power delivered to the load P_L as a function of load impedance Z_L for a source output impedance fixed at $R_s = 100\ \Omega$ and source voltage of $V_s = 10$ V. It can be seen from the plot that indeed we get maximum power at the load when the two impedances match.

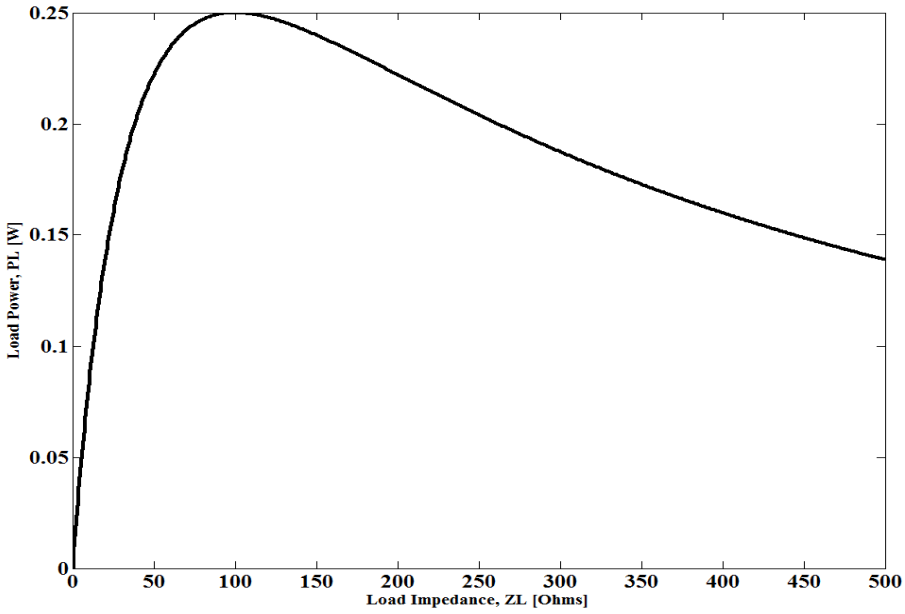

Fig. 2.11: Load power as a function load impedance.

In many practical cases there are no degrees of freedom on both output impedance R_s of a driving circuit and the input impedance Z_L of the load circuit. In such cases an interfacing network has to be implemented and installed between the two impedances. This network should transform the output impedance R_s of the driving circuit and make it appear to the load as just Z_L. This process of equalizing the impedances between two circuits connected in cascade form is called *impedance matching*. A wide variety of components and circuits can be used for doing this job including the L, π, T and LCC Networks and transformers [41–43].

Matching with Transformer

In our case we used a transformer for impedance transformation when coupling into the resonator with an input coil as well as when inductively coupling out with the probe coil. The transformer approach takes advantage of the dependence of inductive reactance on the number of turns N of the inductor.

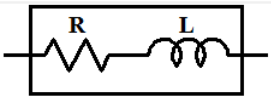

Fig. 2.12: An inductor model with internal resistance R.

The impedance due to an inductor is given by:

$$Z_L = R + j\omega L \tag{2.25}$$

where ω is the frequency in radians per second and L is the self inductance of an inductor. But the (*self*) inductance L is given by:

$$L = \frac{\mu N^2 A}{l} \tag{2.26}$$

where μ is the permeability constant, A and l are the cross-sectional area and length of the inductor coil respectively. Now an ideal transformer consists of two coils (no internal resistances) with number of turns N_p for primary and N_s for secondary and the corresponding coil lengths and cross-sectional areas as shown in Fig. 2.13 below.

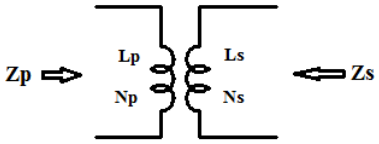

Fig. 2.13: Impedance transformation with an ideal transformer.

In the ideal case whereby the real part (resistance) of an inductor is zero or relatively small, the ratio relating the output impedance Z_s of the transformer to its input impedance Z_p can be shown to be:

$$\frac{Z_s}{Z_p} = \frac{N_s^2}{N_p^2}\frac{A_s}{A_p}\frac{l_p}{l_s} \tag{2.27}$$

This means a transformer converts an output impedance Z_p of a device and makes it appear as if it had an output impedance of $\frac{N_s^2}{N_p^2}\frac{A_s}{A_p}\frac{l_p}{l_s}Z_p$ at the transformer output (secondary coil). Thus, for impedance matching one can tune the relative number of turns, cross-sectional area and/or length of the coils to achieve best matching. If the two impedances to be matched are known, one needs to build a transformer with the turns ratio given by the square root of the ratio of those impedances. If the impedance are unknown, one has to rely on the knowledge that power transfer is maximum when the the source impedance is matched with the load impedance and keep varying the transformer turns ratio until maximum power is measured at the load.

Matching with Resonator

As mention in the beginning of this chapter a resonator is a form of impedance matching device and as such it can be designed to achieve the maximum power transfer from source to load. Consider matching a source ($R_s = 50\Omega$) to a capacitive load C_T with leakage resistance R_T with an L - matching network as shown in Fig. 2.14 below.

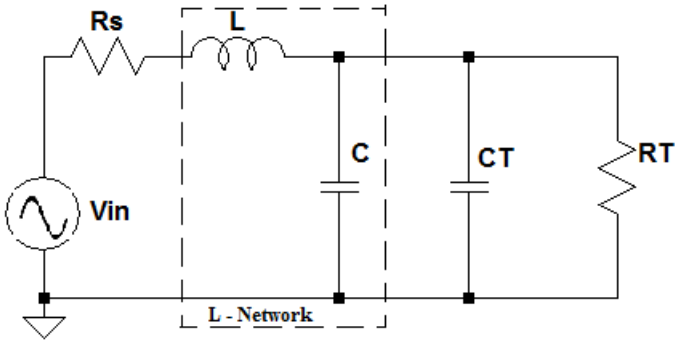

Fig. 2.14: A resonant L - matching network.

The L - matching network is a resonant circuit that can be designed such that at resonance the reactances cancel out and source and load resistances are matched. For $R_T > R_s$ the following parameters achieve the necessary matching:

$$\begin{aligned} L &= \frac{R_s}{\omega_n}\sqrt{\frac{R_T}{R_s}-1} \\ C &= \frac{1}{\omega_n R_T}\sqrt{\frac{R_T}{R_s}-1} - C_T \end{aligned} \tag{2.28}$$

where ω_n is the resonance frequency. The corresponding voltage transfer function of the circuit above, given by:

$$G(s) = \frac{\frac{1}{L(C+C_T)}}{s^2 + (\frac{1}{R_T(C+C_T)} + \frac{R_s}{L})s + \frac{R_s+R_T}{R_T L(C+C_T)}} \tag{2.29}$$

which is a resonator with resonance frequency $\omega_n = (\frac{R_s+R_T}{R_T L(C+C_T)})^{\frac{1}{2}}$ and the selectivity (or quality factor) $Q = \frac{((R_s+R_T)R_T L(C+C_T))^{\frac{1}{2}}}{(R_s R_T(C+C_T)+L}$. This configuration matches the source impedance to a higher impedance load. In the case whereby the source has higher impedance than the source the inductor and capacitor swap positions. Although easier to build, the L - matching topology limits the choice of Q - factor of the matching network or resonator since the Q - factor is dictated by the source and load impedance. For ion trapping applications this can be thought of as matching the rf source impedance to the trap leakage resistance provided this leakage resistance is higher than the rf source impedance. That is, the capacitance of the trap becomes part of the L - network hence the inductor is the only component to be chosen appropriately to match a particular operating frequency. However, the trap leakage resistance is usually

smaller than the rf source impedance hence this network would be a bad choice for matching unless some additional matching stage is introduced such as a matching transformer.

More sophisticated topologies, like π - network and T - network, offer a degree of freedom to tune the Q - factor independently from the source and load impedances and make no restriction on which of the two impedances to be match should be smaller. These networks achieve these good features by merging two L - networks in one network. If we want to match the rf source resistance to the trap resistance (leakage) we can choose a π - network which allows us to treat the trap capacitance as part of the matching network. The impedance matching networks are not necessarily optimizing the voltage delivered to the trap electrodes but rather maximizing the energy delivered to the trap electrodes. The importance of this maximization of delivered energy is that there back-reflected power is minimal ad does not generate interference on our camera screen. Matching with a step-up transformer on the other hand (as we did with our helical resonator) leads to maximization of both voltage and energy.

2.4 Helical Resonator

Designing circuits using lumped elements becomes a challenge when operating in the frequency regime near the self-resonance frequencies of individual lumped elements, which is from a few tens of megahertz to hundreds of megahertz. The self-resonance of an individual lumped element has to be considered in the design and this complicates the entire process of designing. An alternative approach would be to go for transmission line resonators like a quarter-wave section. However, the transmission line resonators are impractical for frequencies around tens of megahertz and below since the required transmission line length would be too long for compact design. A popular alternative [2, 33, 34, 44] for designers in this situations is to go for a helical resonator which is usually used in the mid-range frequencies where lumped components are hard to model due to parasitic properties and yet again the transmission line resonators are too cumbersome.

The helical resonator could be thought of as a compact transmission line shortened through winding of the coil. In some way one could also think of the helical resonator as an inductor whose parasitic capacitance has been carefully altered through adding other parts, like a shielding case, to meet some given specifications. This alteration of parasitic capacitance changes the self-resonance frequency of the inductor and hence opens up a degree of freedom to design a quasi-lumped resonant filter for various desired frequencies of operation. The design question then becomes that of what properties of the additional parts to the inductor are required in order to achieve a filter with certain characteristics such as resonance frequency and quality factor.

2.4.1 Theory, Design and Predictions

A typical helical resonator consists of a copper can, called the shield, and copper coil inside it as shown in the schematic in Fig. 2.15. One end of the coil could be connected to the shield and grounded or

connected to the driving rf source depending on how the rf drive voltage is coupled to the resonator. The other end of the coil becomes the output of the resonator.

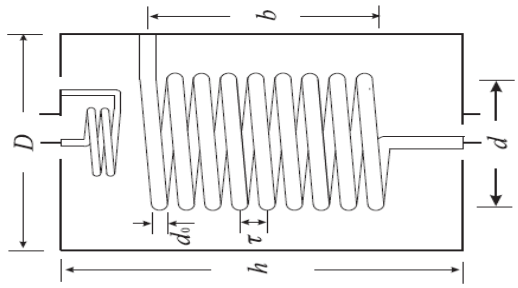

Fig. 2.15: The structure of helical resonator (right) and a small input coupling coil (left). [2].

While there have been attempts to derive the equations describing the properties of the helical resonator, most of the design equations are largely empirical as outlined below. The helical resonator performance is very much dependent on its geometry and electrical properties of material used. Due to well-established design techniques of circuit using lumped elements, there have been attempts to obtain equivalent lumped element models for helical resonator, including [2, 33]. In [33] the equivalent capacitance C_e of an unloaded resonator is considered to be the parallel connection of the shield capacitance C_s and coil capacitance C_c as shown in the equivalent circuit model in Fig. 2.16.

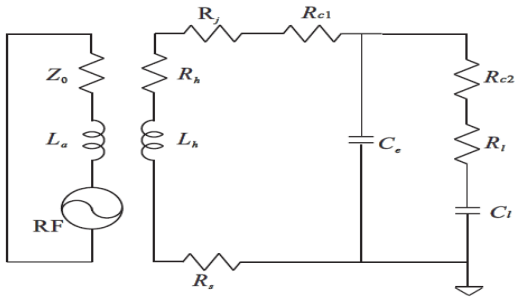

Fig. 2.16: Simplistic equivalent circuit model [2].

This model is criticized in [2] for not accounting for the inter-coupling effect of C_s and C_c thereby not giving a full picture. Fig. 2.17 below shows how this inter-coupling effect is accounted for in [2] through a model of network of capacitors C_{s0} and C_{c0}. This is the same model we adopt in this work and more details can be found in [2] .

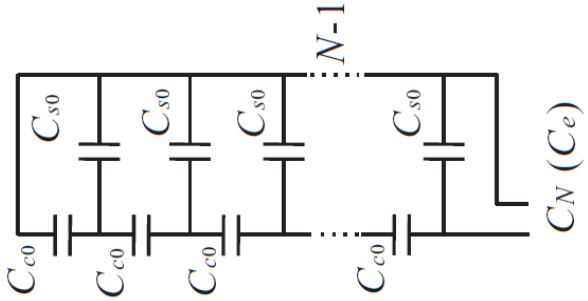

Fig. 2.17: Equivalent circuit model with inter-coupling effect [2].

While designing the helical resonator a designer must take into account the loading effect when the drive and load are connected to the helical resonator. This is because if the output impedance of the helical resonator is not sufficiently small relative to the input impedance of the load circuit then the helical resonator dynamics will be altered by the load circuit and parameters such as resonance frequency and frequency selectivity can shift. It is therefore, important that the design parameters are chosen based on the loaded resonator rather than unloaded one. It becomes helpful then to know about the load circuit before designing the helical resonator. With this information in mind a designer can choose the resonator parameters; τ, b, d, N and D such that the predicted unloaded resonance frequency f_u of the helical resonator shifts to the desired operating frequency f_l when loaded with the intended load circuit.

In our case the load circuit is the ion trap which is effectively a capacitor measuring $C_T = 14.9$ pF without the feed-through connections and $C_T = 28.82$ pF with the feed-through connected. Our helical resonator parameters b, d and D are fixed at 120 mm, 89 mm and 154 mm respectively while the number of turns N is left to be tuned so that the desired loaded resonance frequency of around 15 MHz is obtained when the resonator is loaded with $C_T = 28.82$ pF. Changing the number of turns affect the spacing τ between turns through the relation, $\tau N = b$. The following equations, taken from [2] and [33], are used to obtain the required helical resonator's total capacitance C_N and inductance L.

The capacitance created by the shield and the coil is given by equation (2.30) below:

$$C_s = 39.37\frac{0.75b}{log_{10}(\frac{D}{d})}pF/m = 32.71 \text{ pF} \tag{2.30}$$

The capacitance created by the turns of the coil itself is given by equation (2.31) below:

$$C_c = d(11.26\frac{b}{d} + 8 + 27\sqrt{\frac{d}{b}}) \text{ pF/m} = 4.13 \text{ pF} \tag{2.31}$$

Using equations below, different values of N were tried to determine the resonator inductance L and capacitance C_N which result in the loaded resonance frequency close to 15 MHz. This trial and error led to $N = 7$ and the coil turning pitch of $\tau = 15$ mm. In [33] the inductance of the coil is approximated by equation (2.32) shown below:

$$L = 39.37b\frac{0.025d^2(1-(\frac{d}{D})^2)}{\tau^2} \ \mu\text{H/m} = 2.12 \ \mu\text{H} \tag{2.32}$$

The total capacitance of the helical resonator is obtained as follows:

$$\begin{aligned} C_{c0} &= (N-1)C_c = 24.80 \text{ pF} \\ C_{s0} &= C_s/(N-1) = 5.45 \text{ pF} \\ C_1 &= C_{c0} + C_{s0} = 30.25 \text{ pF} \\ C_N &= \frac{C_{co}C_{N-1}}{C_{co}+C_{N-1}} + C_{so} = 14.70 \text{ pF} \end{aligned} \tag{2.33}$$

The resonance frequency of the helical resonator is then given by equation (2.34) below:

$$f_u = \frac{1}{2\pi\sqrt{LC_N}} = \frac{\omega_u}{2\pi} = 28.51 \text{ MHz} \tag{2.34}$$

This quantity f_u above is referred to as unloaded resonance frequency primarily because it is predicted the resonator without the load at its output. In the case where the resonator is loaded with a capacitive load, like an ion trap $C_T = 28.82$ pF, the resonance frequency shifts and the resulting resonance frequency becomes:

$$f_l = \frac{1}{2\pi\sqrt{L(C_N+C_T)}} = \frac{\omega_l}{2\pi} = 16.57 \text{ MHz} \tag{2.35}$$

2.4.2 Implementation and Measurements

Fig. 2.18 below shows different parts of our helical resonator with dimensions mentioned in the previous section. The input voltage to the resonator is coupled into the resonator through the input coil, which is adjusted for maximum coupling and locked. This input coupling coil was constructed based on a manual optimization (trial and error) of minimizing back-reflected voltage using a directional coupler. Teflon was used to provide support for the main coil. The output terminals of the resonator protrude to the outside of the casing through the mouth piece, shown in the picture, and connect to the feed-through from the ion trap. The probe is used used for monitoring the resonator voltage signal indirectly by inductive coupling.

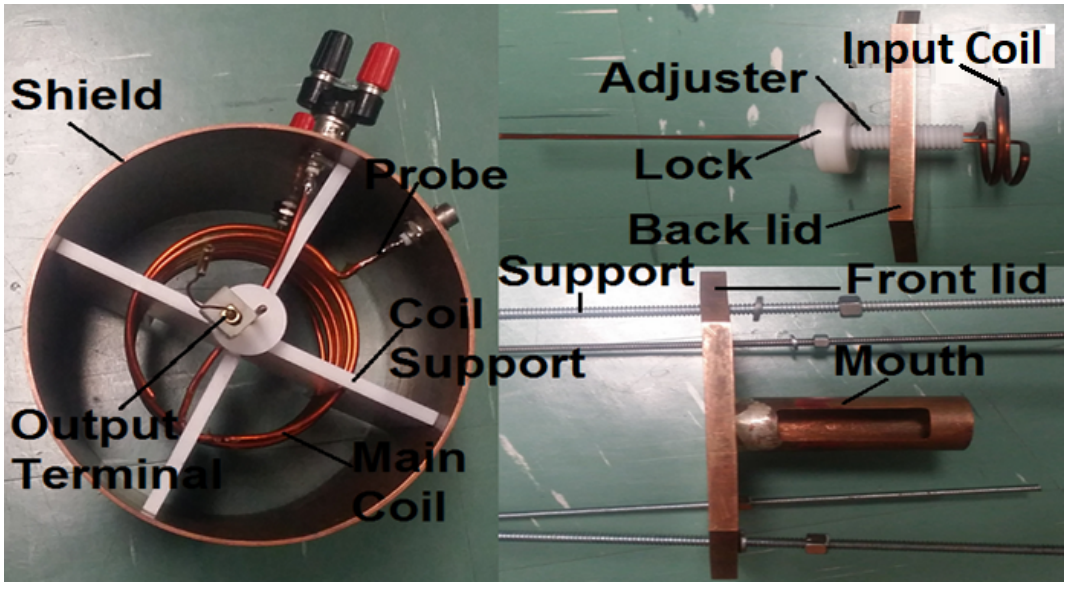

Fig. 2.18: A picture of helical resonator.

Measuring the output voltage of the resonator directly with a 50 Ω scope causes the resonance to shift from 15.63 MHz down to around 8 MHz. This is because the output impedance of the resonator is not small enough relative to the input impedance of the scope and this causes current loading problems. The

standard probe cables can overcome this loading problem but they also have a significant capacitance in parallel with the trap capacitance and thus, can modify the effective capacitance of the circuit leading to a significant resonance shift again. One trick is to use a network of inductors (i.e. a transformer) to transform the impedances of the two such that the resonator sees the scope's input impedance being quite higher than what it actually is. This alternative way of measuring without significantly affecting the resonator dynamics can be viewed as inductively coupling out the signal from the output of the resonator.

That is, a probe wire is fixed close to the output end of the inner coil so that the output of the resonator is induced into the probe and can be monitored on the scope. This probe wire can be seen in Fig. 2.18 above, with about half a turn in length. To help with calibrations we built another probe which couples capacitively, instead of inductively, with a network of capacitors. A simple potential divider network in Fig. 2.19 below shows the setup for impedance transformation between helical resonator and the scope using this network of capacitors as done in [35].

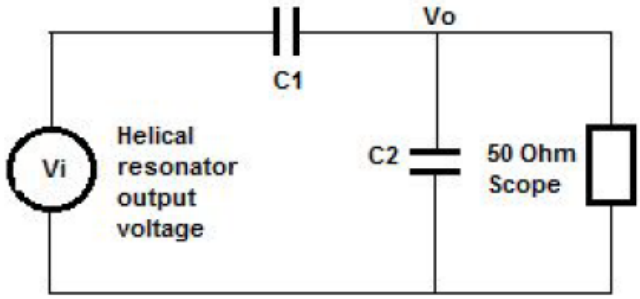

Fig. 2.19: Capacitive probe setup we made for the illustration of capacitive coupling.

The impedance of the scope as seen by the resonator is $\frac{(C_1+C_2)^2}{C_1^2}$ times the original scope impedance of 50 Ω. Thus, choosing C_2 much larger than C_1 can amplify the scope's impedance. The step up ratio from the scope voltage (V_o) to the resonator voltage (V_i) is given by $\frac{Vi}{Vo} = 1 + \frac{C_2}{C_1}$. Also since C_1 is in parallel with the trap capacitance, it should be chosen such that it is relatively small compared to the trap capacitance so that it does not add any significant capacitance that results in lowering the resonance frequency. In our case we chose $C_1 = 1.1$ pF and $C_2 = 220$ pF and this gives scope impedance step up of 40401 while the scope to resonator to trap voltage step-up is 201. To test these predictions we drove our capacitive transformer with a function generator and monitored both its input and out voltage.

The measured voltage step up was 195 over the range frequencies swept ($12 - 19$ MHz), therefore, our predicted step-up is off by only 3%. The first inductive probe was then connected to measure the output of the resonator and the resonance shifted from 15.63 MHz to 15.23 MHz which about 2.6% shift. The step up ratio from the capacitive probe to the in-built inductive probe was measured to be $1 : 4.34$ and the step up from the capacitive probe to the resonator output measured $1 : 195$. The step up ratio from the in-built inductive probe to the resonator output was determined from the two step up ratios and found to be $1 : 45$. This ratio helps us to figure out the actual resonator output voltage given the monitored voltage from the inductive probe. With the probe setup in place we proceeded to determine the parameters of the helical resonator. Looking at equation (2.35) we can rearrange terms to get the following,

$$\omega_l^{-2} = LC_X + LC_N \tag{2.36}$$

which can be viewed as a straight line equation with the $y-$intercept LC_N and slope L. So to measure the inductance L and capacitance C_N of the helical resonator we loaded it with various known capacitors C_X and produced a plot of inverse square radial frequency ω_l^{-2} against the load capacitor C_X as shown in Fig. 2.21 (*Left*) below. The slope of this plot gives an approximate value of the resonator's internal inductance L while the y-intercept gives LC_N from which the resonator's capacitance C_N can be obtained since L is known. The same experiment was carried out, but this time with the ion trap (*load*) connected as shown in Fig. 2.20 below.

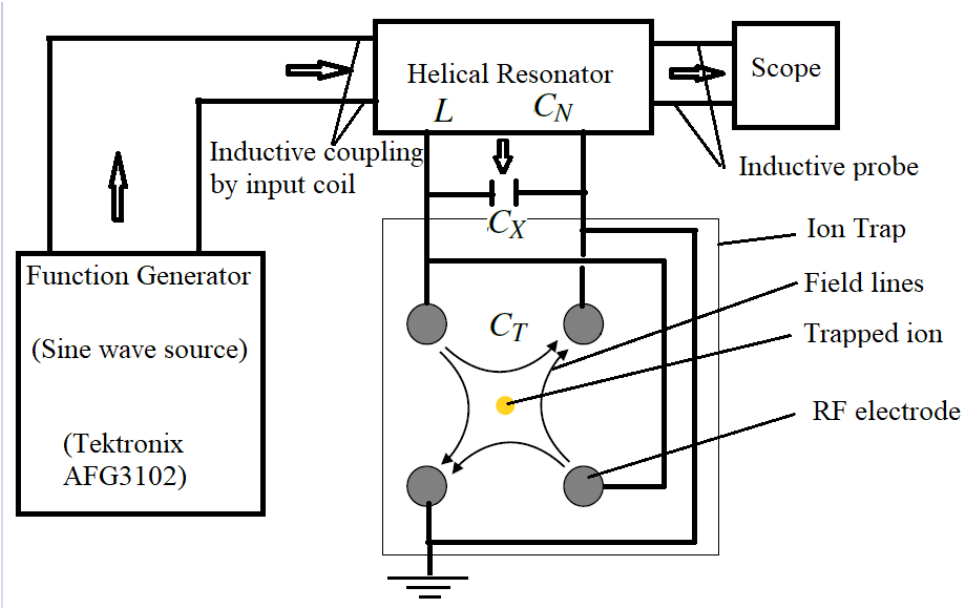

Fig. 2.20: Schematic diagram showing connections from function generator to ion trap for determination of inductance and capacitances.

Fig. 2.21 (*Right*) below shows the corresponding linear fit which helps us determine the combined capacitance of the resonator and ion trap.

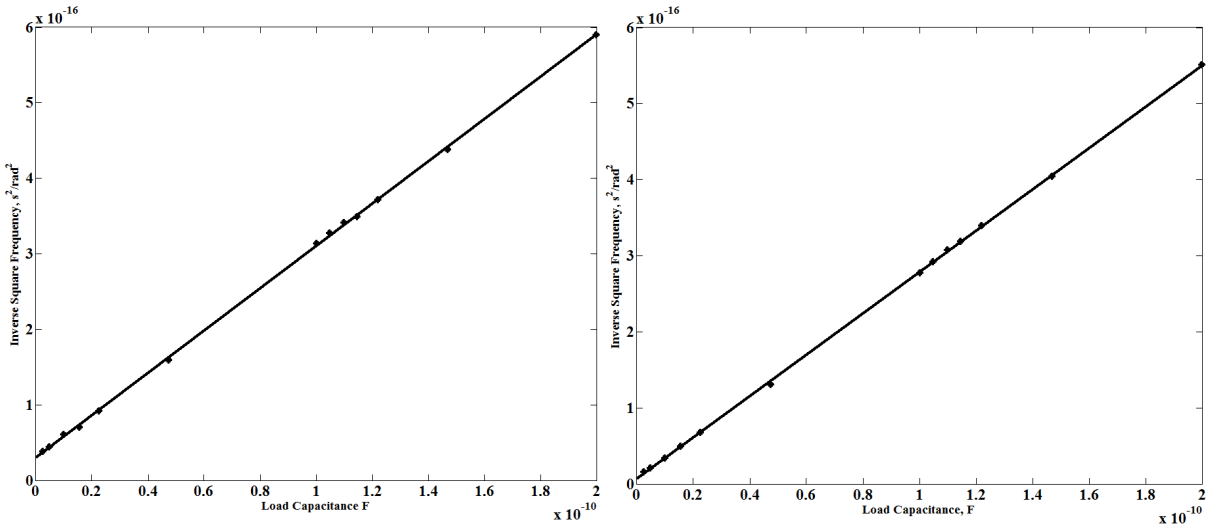

Fig. 2.21: Determining the inductance and capacitance of unloaded (*Left*) and loaded (*Right*) helical resonator.

From Fig. 2.21 the values of L and C_N are found to be,

$$\begin{aligned} L &= 2.80\ \mu\text{H} \\ C_N &= 10.80\ \text{pF} \end{aligned} \tag{2.37}$$

And the values of the inductance of trap and resonator L_c and the combined capacitance of trap and resonator C_c are found to be,

$$\begin{aligned} L_c &= 2.72\ \mu\text{H} \\ C_c &= 39.62\ \text{pF} \end{aligned} \tag{2.38}$$

Thus, the trap capacitance is approximately,

$$C_T = 28.82\ \text{pF} \tag{2.39}$$

The resistivity of the resonator is not known *a priori* and need to be determined through experiment to obtain a complete identification of the resonator. The following schematic diagram in Fig. 2.22 shows how the components were connected in order determine the frequency response of the resonator plus trap.

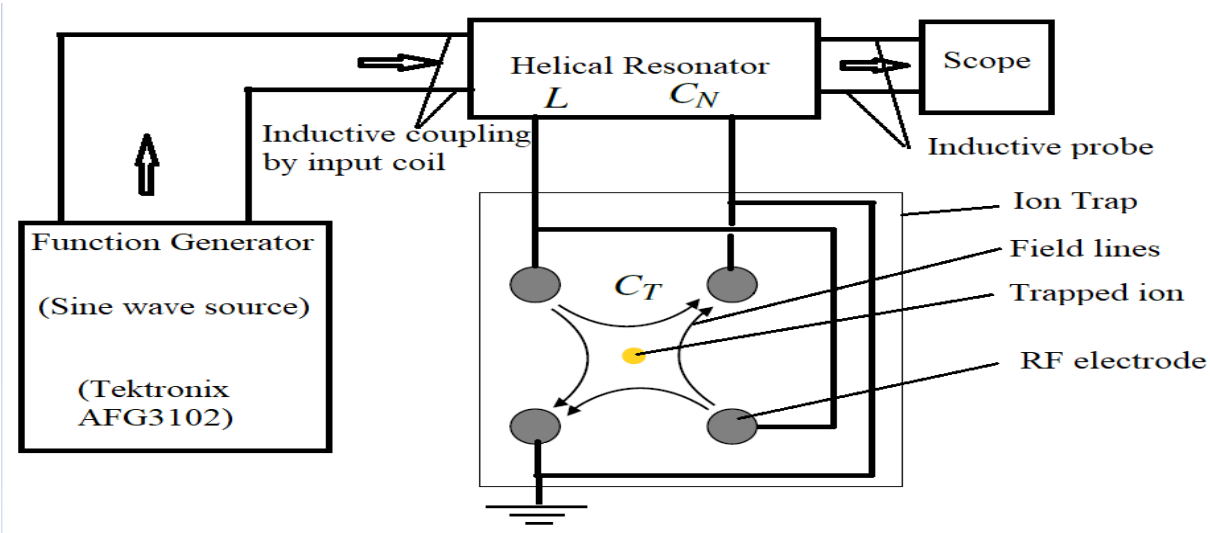

Fig. 2.22: Schematic diagram showing connections from function generator to ion trap for determination of resonator frequency response.

The voltage was measured at the output of the of the function generator (as input voltage) and also a the probe of the resonator (as output voltage). The voltage gain was then computed as the ratio between the measured output voltage and input voltage. The voltage gain of the resonator was measured for various frequencies and from the plot of voltage gain against frequency the Q-factor was determined and the resistance deduced from the Q-factor. Fig. 2.23 below shows plots of the voltage gain (from measured input voltage to measured probe voltage) in decibels against frequency for the unloaded (*Left*) and loaded

(*Right*) resonator respectively and the unloaded and loaded Q-factors are 320 and 96 respectively. The circuit resistances for the unloaded and loaded cases are 1.61 Ω and 3.42 Ω respectively thus, we can infer that the ion trap, together with feed-throughs, contributes the excess resistivity of about 1.81 Ω.

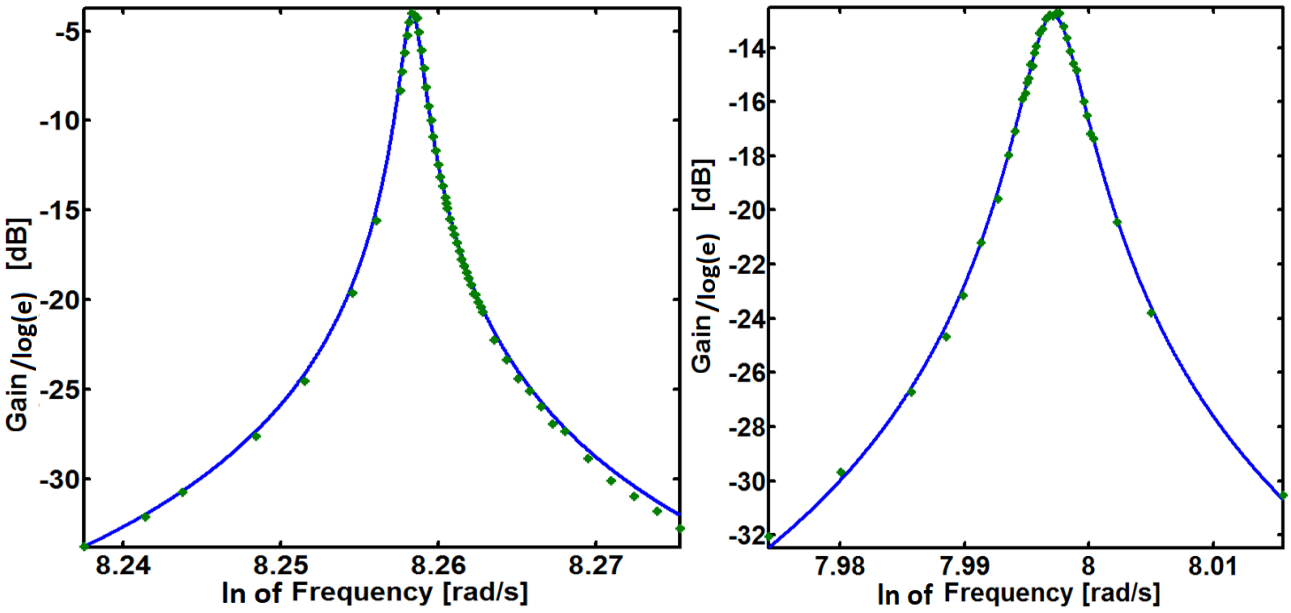

Fig. 2.23: The frequency response of the unloaded (*Left*) and loaded (*Right*) helical resonator.

The information obtained thus, far allows us to write the complete transfer functions for both unloaded and loaded resonators as shown below,

$$\begin{aligned} G_u(s) &= \frac{(0.63)5.6558\times10^5 s}{s^2+5.6558\times10^5 s+3.287\times10^{16}} \\ G_l(s) &= \frac{(0.229)1.0331\times10^6 s}{s^2+1.0331\times10^6 s+9.8679\times10^{15}} \end{aligned} \tag{2.40}$$

These transfer functions relate rf input voltage to the inductive probe output. Therefore, one should multiply these transfer functions by a gain factor $k = 45$ from resonator probe to the resonator output to obtain the transfer functions from rf input voltage to rf output voltage of the resonator. The gain against frequency plots in Fig. 2.23 above have no information regarding the phase relationship between input and output voltages, however, the corresponding transfer functions in equation (2.40) above have the phase information embedded in them. The resonance frequencies for the unloaded and loaded resonator, extracted from equation (2.40) above are,

$$\begin{aligned} \omega_u &= 2\pi(28.85\text{ MHz}) \\ \omega_l &= 2\pi(15.81\text{ MHz}) \end{aligned} \tag{2.41}$$

These measured resonance frequencies are slightly off from the predicted values, with the unloaded resonance frequency being off by about1.2% from the predicted value of 28.51 MHz while the loaded resonance frequency is off by about 4.8% from the predicted value of 16.57 MHz.

2.4.3 Mounting and Testing

A stand for the resonator was constructed out of old aluminium tubes, as shown in Fig. 2.24 below, to hold the helical resonator up and close to the feed-through connected to the linear Paul trap inside the vacuum chamber. Due to it being bulky, the helical resonator setup seems to take up a significant amount space, next to the vacuum chamber, that could be used for something else useful. The connection setup begins with a function generator driving the rf amplifier whose output is connected to the input of the helical resonator and lastly the output terminals of the resonator connect the ion trap in the chamber through the feed-through wires.

Fig. 2.24: The mounted helical resonator.

The probe, coupled inductively to the resonator output, is monitored on the scope at all times so as we can infer the voltage applied on the trap using the probe voltage and the step up factor. After mounting the helical resonator the testing phase followed in which attempts to trap ions were made. In this case there is an rf amplifier between the function generator and the helical resonator as shown in Fig. 1.5. The ion cloud was successfully trapped with function generator voltage output set to 310 mVpp and the resonator probe reading 2.42 Vpp.

Fig. 2.25: A string of four cold trapped ytterbium 171 ions in our lab at Stellenbosch University.

Using the step up factor of 45, from probe voltage to trap voltage mentioned in the previous section, the inferred voltage across the trap electrodes is 108.9 Vpp. The trapped single ions are shown in Fig. 2.25

above as captured by the camera from the top of the trap. We are confident that this shows four trapped ions first because of the crystalline structure which is indicative of Coulomb repulsion. Secondly based on the estimated spacing 8 μm – 16 μm between adjacent bright spots. This spacing seems reasonably close to the commonly reported values on the order of 10 μm.

The internal resistivity of the resonator places the upper limit on the quality factor (selectivity) of the resonator. The less internal resistance the resonator has the more selective (high quality factor) it becomes, thus, giving a cleaner voltage signal. However, the helical resonator's resistance is not easy to reduce without having to redesign the entire resonator from scratch with material of lesser resistivity. On the other hand the advantage of helical resonator is that it is cheap in power requirements since it's fully passive. It is not sensitive to component self-resonances due to parasitic behaviors in the component at high frequencies and it tolerates high powers. The main disadvantage is that its design is nontrivial, tuning of frequency and quality factor is not easy and achieved through tedious trial and error.

2.4.4 Modifications on Helical Resonator

The lids of the resonator had to be fixed in place to avoid shifts which affect the resonance frequency. The grooves were drilled into the lids to give a snug fit with a cylinder thus, holding all parts fixed relative to each other. The number of turns in the main coil was also changed to compensate for the 3 mm reduction in resonator length due to grooves on the lid plates. The new helical resonator parameters b, d and D are 105 mm, 89 mm and 154 mm respectively while the number of turns is $N = 6.5$. Fig. 2.26 below shows the plot of inverse square angular frequency against load capacitance.

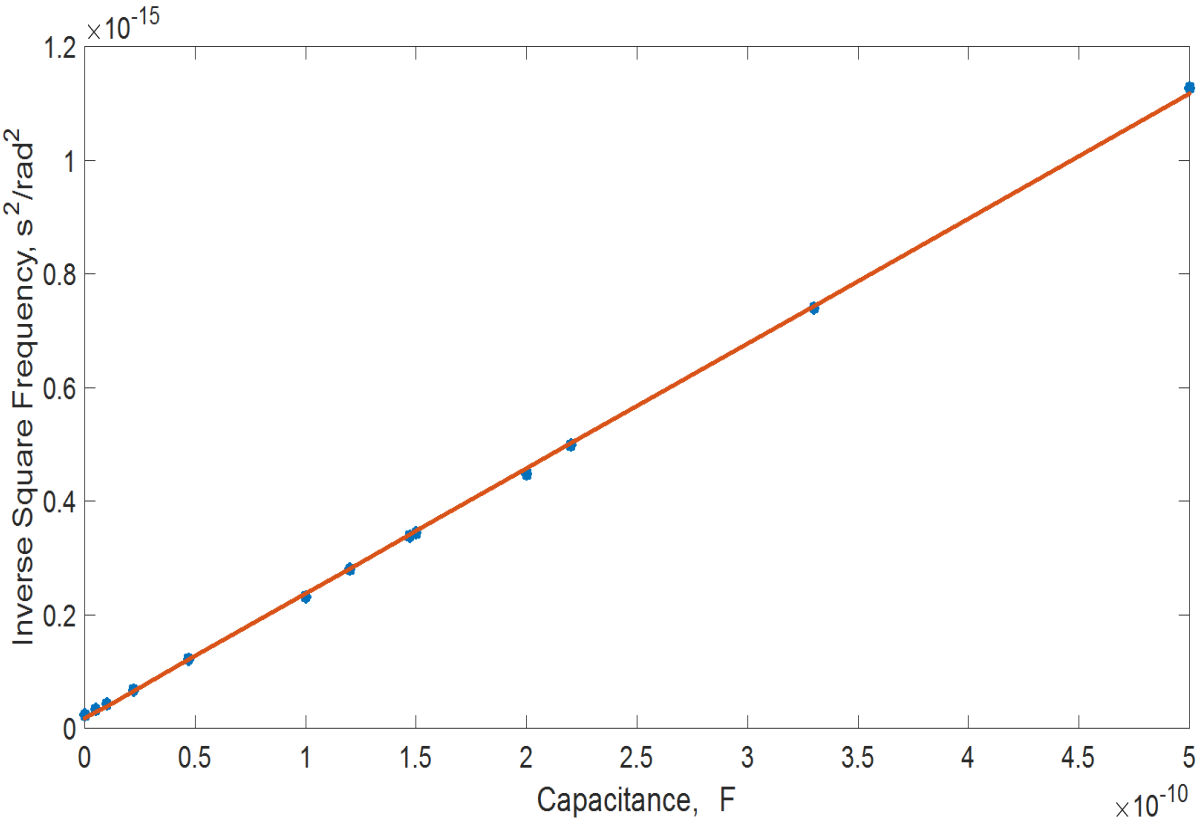

Fig. 2.26: Helical resonator inductance and capacitance line fit after lid modification.

The slope of the line gives the resonator inductance L while the $y-$intercept gives the product of the resonator capacitance and inductance LC_N as described previously in equation (2.36). The new inductance for the unloaded resonator is $L = 2.09\ \mu$H and the resonator capacitance is $C_N = 10.92$ pF thus, making the predicted unloaded resonance frequency to be $f_u = 33.315$ MHz. Fig. 2.27 below shows the frequency response of the modified unloaded resonator.

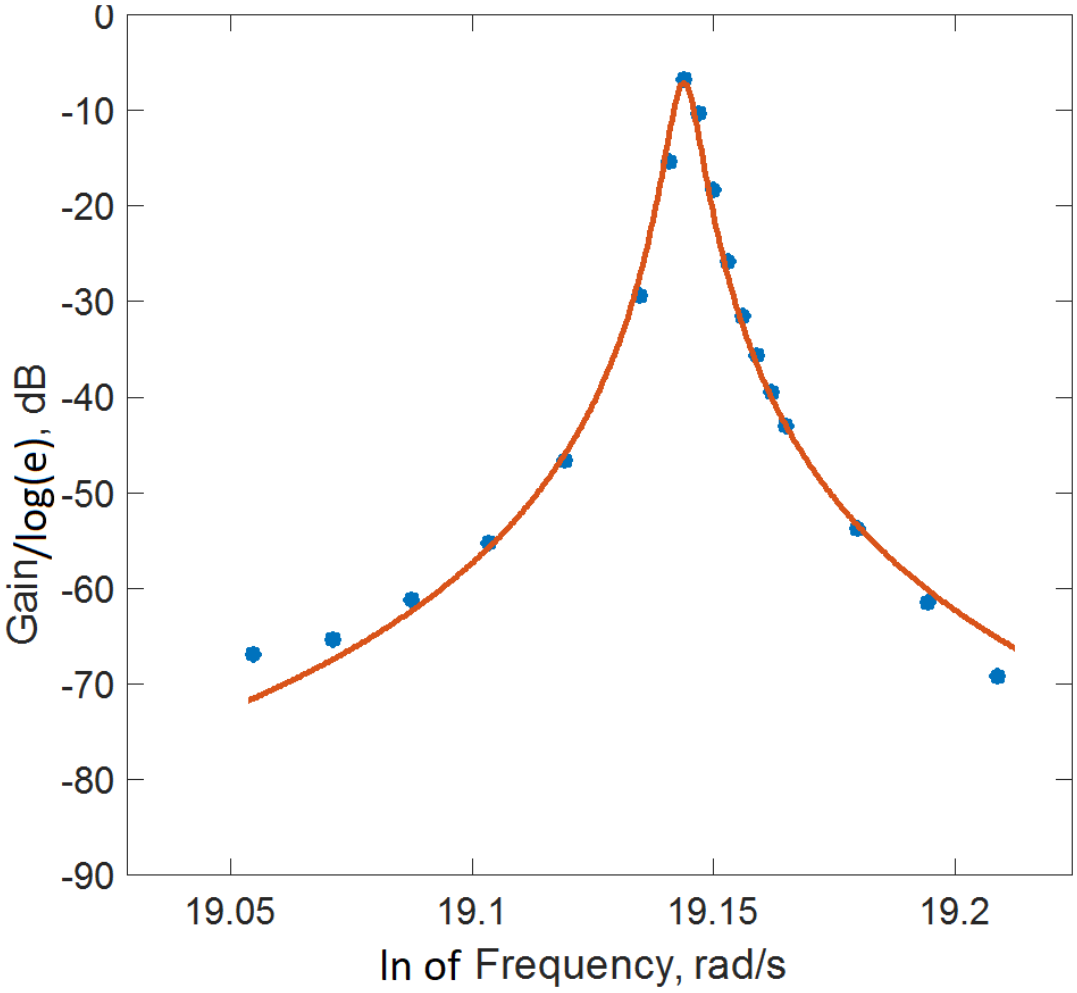

Fig. 2.27: Helical resonator frequency response after lid modification.

The transfer function model used for fitting this response data is the same as equation (2.19) with quality factor $Q = 140$, resonance frequency $\omega_n = 2\pi(32.8\text{ MHz})$ and the dc gain $b = 0.7$. There is a 1.6% deviation in resonance frequency between the two characterization approaches outlined above, which we believe can be reduced by further by taking more data points to refine the model parameters.

2.5 LC Resonator

Another resonator (LC) was built to serve as our backup resonator ready to kick in when needed for ion trapping purpose. A passive LC resonator is arguably one of the simplest and quickest resonator to construct with lumped elements. In its series configuration an LC resonator, as shown in Fig. 2.28 below, has a response similar to that of a low pass filter with an added resonant peak response.

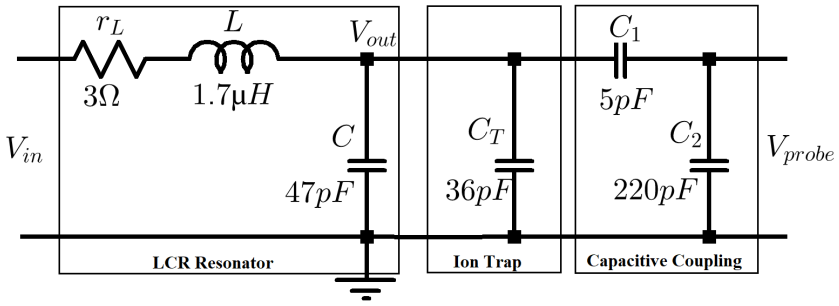

Fig. 2.28: A circuit model of an LC resonator with a capacitively coupled probe.

The circuit model in Fig. 2.28 above was simulated in LTSpice, as shown in Fig. 2.29 below, with component parameters ($C = 47$ pF, $C_1 = 5$ pF, $C_2 = 220$ pF, $C_T = 36$ pF, and $L = 1.7$ μH with $r_L = 3\ \Omega$) chosen to give resonance frequency of $\omega_0 = 1/\sqrt{L(C+C_T)} \approx 2\pi(13.40\ \text{MHz})$ and quality factor $Q = r_L^{-1}\sqrt{L/(C+C_T)} \approx 47.7$. The expected ratio between trap voltage V_{out} and probe voltage V_{probe} is given by $V_{out}/V_{probe} = (C_1+C_2)/C_1 = 45$ which is about 33 dB difference between V_{out} and V_{probe} powers in Fig. 2.29 below. The 5 pF capacitor together with the 220 pF capacitor form a capacitive probe whose job is to couple out a small fraction of the output voltage V_{out} without severely distorting the dynamics of the LC resonator on the left.

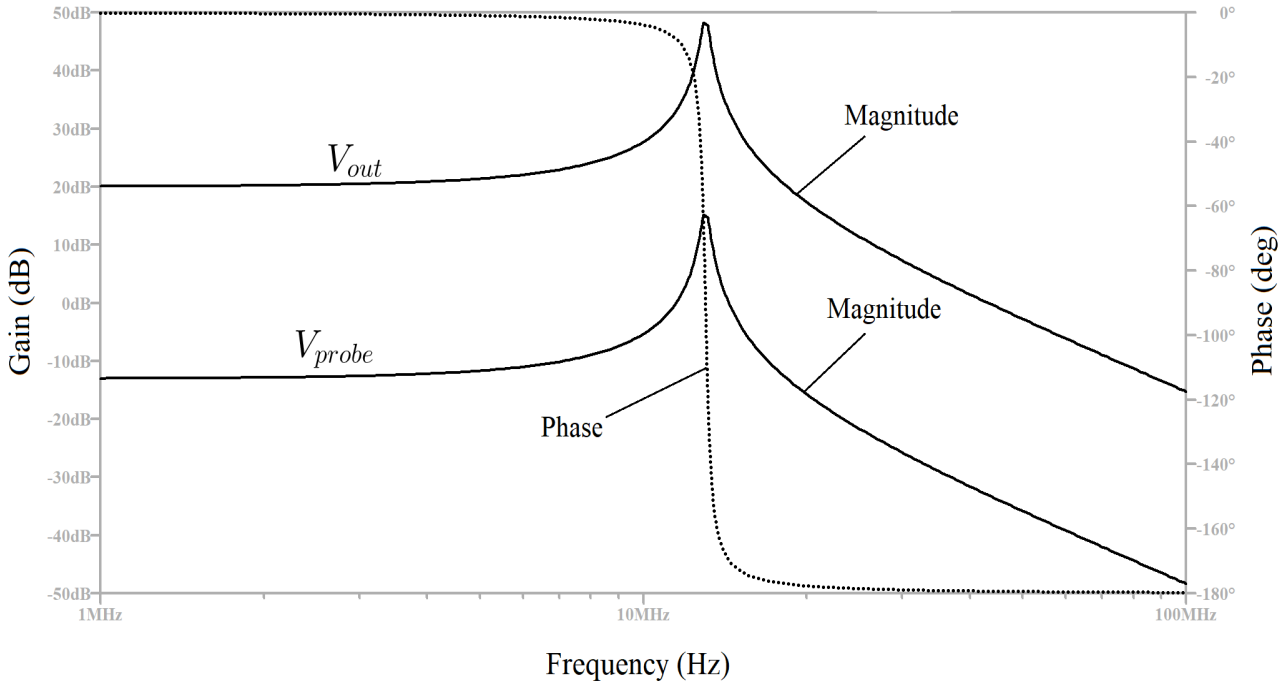

Fig. 2.29: Frequency response of an LC resonator model from Fig. 2.28 above.

The strength of capacitive coupling dictates how close to one another are V_{out} and V_{probe} responses. For amplification, both the dc gain and quality factor are important. The dc gain is the amount of gain that a signal would experience in the absence of resonance effect (low frequencies) hence higher dc gains lead to more signal amplification. The resonance effect adds more gain on top of the dc gain and this gain is equivalent to the value of the quality factor itself. As a backup plan in our lab, an LC resonator was constructed and characterized with the ion trap as the load C_T. Fig. 2.30 below shows the picture of LC resonator implemented based on the model simulated above.

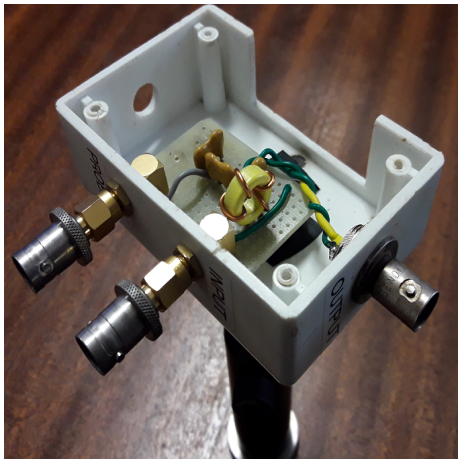

Fig. 2.30: LC Resonator Circuit Schematic and the picture of the circuit.

The LC resonator was loaded with a trap and Fig. 2.31 below shows the corresponding frequency response. It is worth mentioning that at the time of this experiment the trap capacitance had changed to a new value of $C_T = 36$ pF after some modifications were made on the trap.

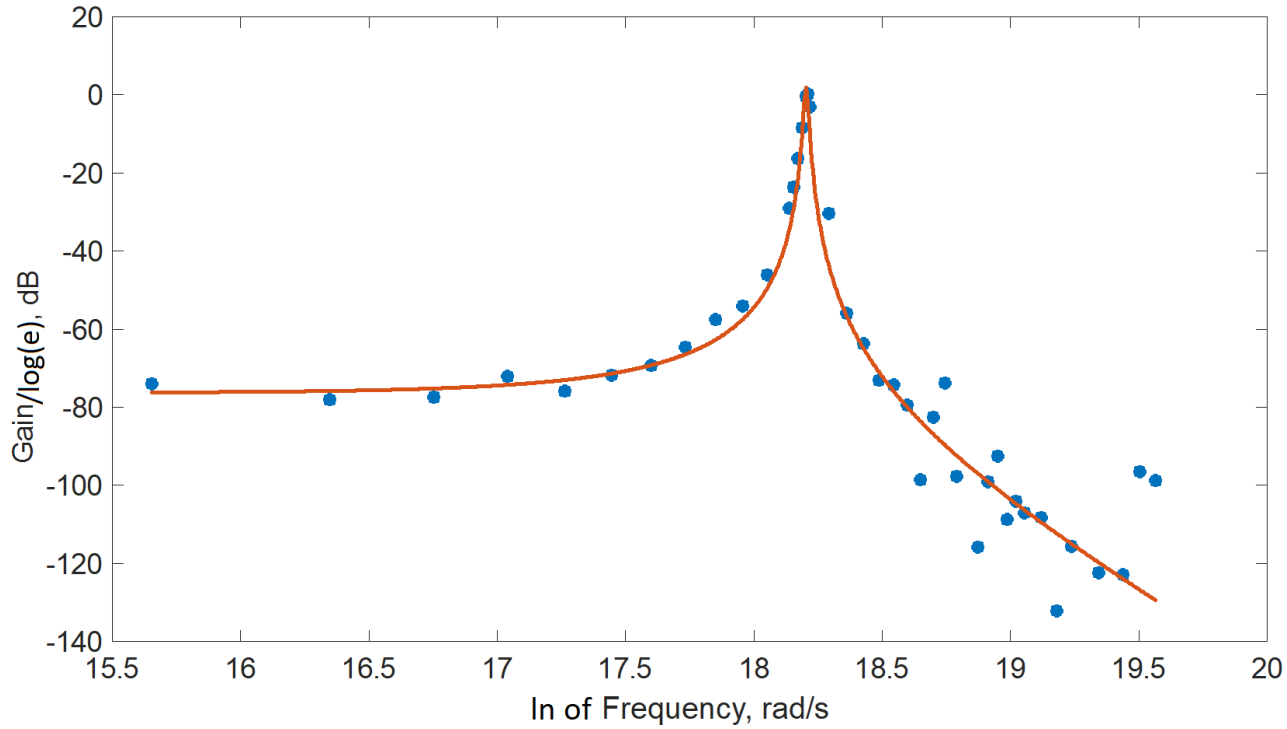

Fig. 2.31: LC Resonator Loaded frequency response showing voltage gain in decibels from input voltage to probe voltage plotted against frequency in radians per second.

The model used for fitting the data is described by the following transfer function,

$$G(s) = \frac{k\omega_n^2}{s^2 + \frac{\omega_n}{Q}s + \omega_n^2} \tag{2.42}$$

and the resulting parameters are resonance frequency $\omega_n = 2\pi(12.8\text{ MHz})$, quality factor $Q = 50$ and dc gain $k = 0.022$. The resonance frequency is off by 4.5% from the predicted value above. Also the quality

factor is off by 4.8% from the predicted value. In the previous paragraphs we established that the step up from the probe to the resonator output is 45 which is the same step up for the helical resonator discussed in earlier sections. The gain at the resonance peak is around 0.8 dB for LC resonator and around -10 dB for the helical resonator which means the input to output gain of our LC resonator is higher than that of our helical resonator. The higher peak gain for LC resonator could be attributed to the dc gain k providing a base upon which resonance peak sits, hence if k is high the resonance peak will be shifted up proportionally in gain. Even though the helical resonator has a lower peak gain, it has a higher quality factor compared to the LC resonator. As mentioned briefly earlier, a designer is faced with a choice of whether to go for higher gain (i.e. LC resonator) or higher quality factor (i.e. helical resonator).

2.6 Summary

In this chapter we outlined some of the pre-requisites and principles involved in ion trapping. This includes the dynamics of ions confined in quadrupole field traps, the assembly of a linear Paul trap and the radio frequency potential generation and filtering using helical and lumped element resonators. It should be noted from the presented resonator theory above that a resonance effect is such that it adds an additional amplitude gain relative to the static gain (i.e. k). This additional gain is proportional to the value of quality factor Q as shown by equation (2.18).

Chapter 3

Trapping Ytterbium Ions

Ions with a single electron in the valence shell have a relatively simple and manageable electronic level structure which simplifies the laser-cooling of such alkali-like ions. Among the good candidates there Be^+, Mg^+, Ca^+, Sr^+, and Ba^+ from group A II earth alkalies, Zn^+, Cd^+ and Hg^+ from group B II transition metals and Yb^+ from Lanthanide series. More details of the required electronic configuration can be found in [45]. The method whereby any of these can be used as a qubit depends on the detailed electronic structure. One type of trapped ion qubit is the optical qubit [24] which makes use of the electronic ground state and a metastable excited electronic state of a trapped ion as the qubit's ground and excited states respectively. The energy difference between these two electronic states matches the energy of the photon from a driving optical laser. Fig. 3.1 below shows a typical structure of an optical qubit.

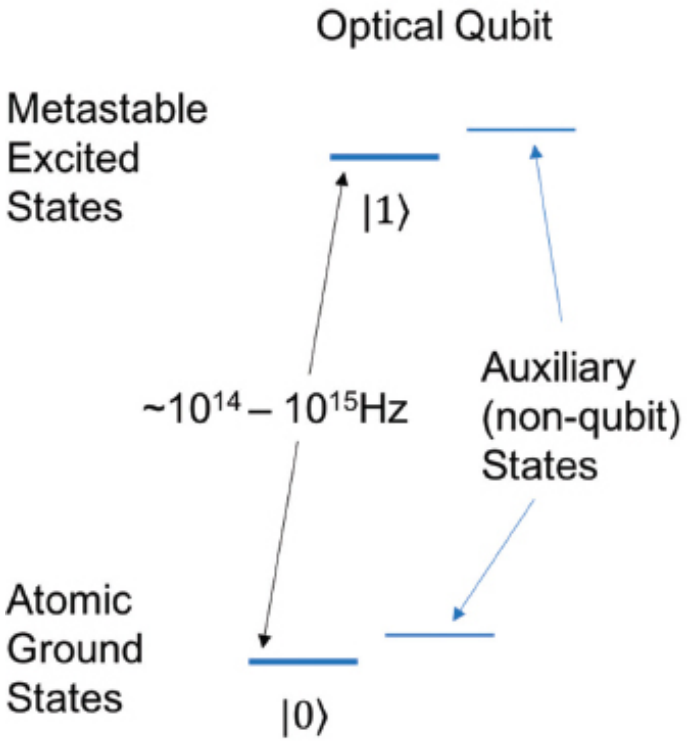

Fig. 3.1: Optical qubit energy levels.

Optical qubits, such as one realized from Calcium ion, have coherence times in the range of 1 to 30 seconds and the efficiency in their preparation and detection exceeds 99.9% [24]. Ions with low-lying D level have the possibility of encoding a qubit in the $S \rightarrow D$ optical transition. However, the D level natural spectral width (a few Hz) requires laser fractional frequency stability of the order of 10^{-14} and this difficulty renders the optical ion qubit choice less common [45].

Ions with zero nuclear spin have only two Zeeman states in the $S_{1/2}$ level, which correspond to the valence electron spin pointing parallel and anti-parallel to the external magnetic field direction [45–47]. Encoding a qubit in a pair of $S_{1/2}$ levels has the advantage of a practically infinite spontaneous decay time. Fig. 3.2 below shows a typical Zeeman qubit level structure.

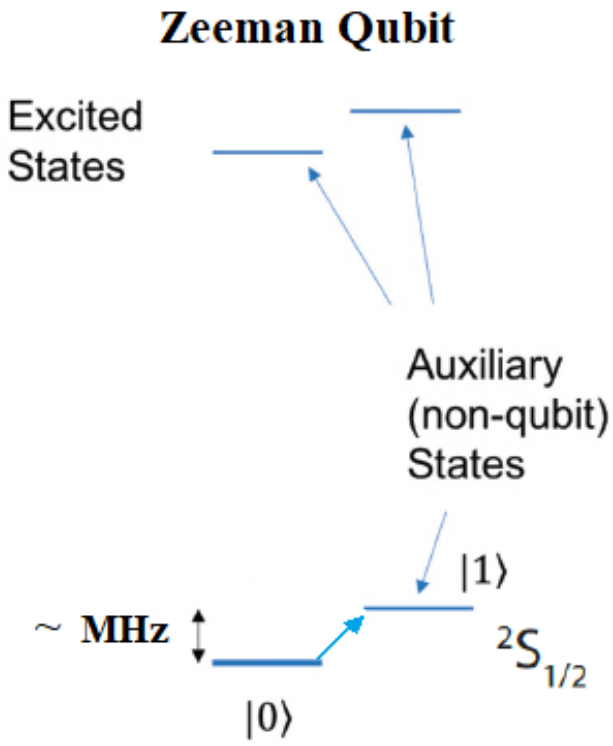

Fig. 3.2: Zeeman qubit energy levels.

An advantage of choosing this qubit is that since the qubit levels are the only levels in the $S_{1/2}$ manifold, optical pumping out of the qubit manifold does not occur however, the disadvantage of the Zeeman qubit is that since the energy difference between the two qubit states depends linearly on the magnetic field, magnetic field noise will cause dephasing [47]. Furthermore, at low magnetic fields the frequency separation between the two qubit states is smaller than the P level natural spectral width and therefore, state selective fluorescence cannot be directly applied for qubit state detection [45].

In odd isotopes or even isotopes with non-zero nuclear spin, the $S_{1/2}$ is split into different m_F states within the different F-hyperfine manifolds with the energy separations in the gigahertz for common ions like ytterbium 171. A qubit can be encoded in any pair of hyperfine states [45]. Fig. 3.3 below shows an example of a hyperfine qubit levels for ytterbium 171.

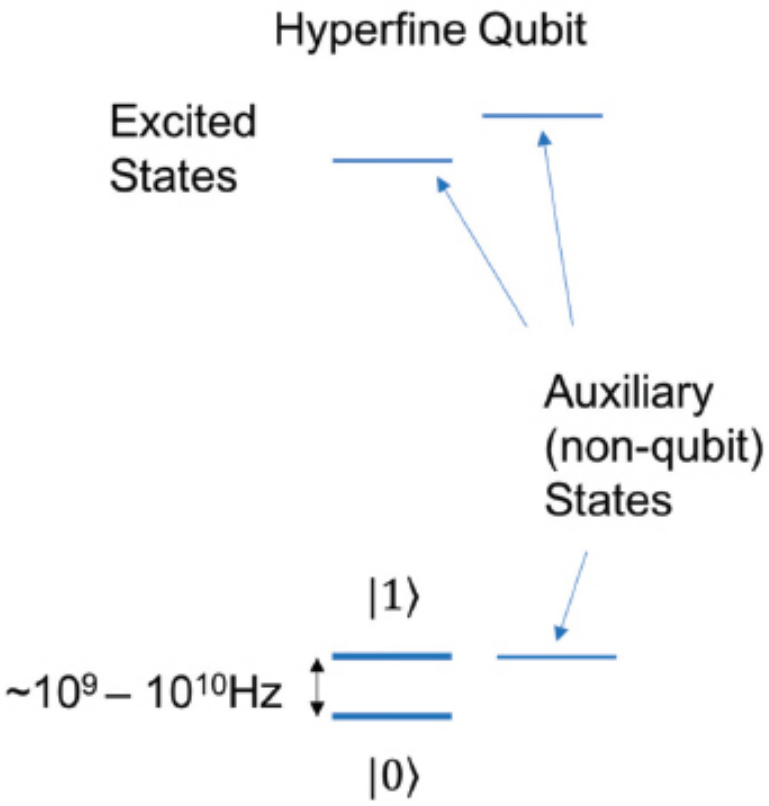

Fig. 3.3: Hyperfine qubit energy levels.

An advantage of the hyperfine qubit choice is that pairs of levels can be found such that their energy separation does not depend, to first order, on the magnetic field [45]. This chapter covers the concepts and techniques involved in trapping, cooling and manipulating Ytterbium ions. Although ytterbium has many isotopes we focus mainly on $^{171}Yb^{+}$ and $^{174}Yb^{+}$ since trapping these two isotopes is convenient for individual ion addressing which is essential for realizing two qubit entanglement and implementing unsharp measurements among other things.

Most of this chapter covers the interaction of an ion with laser and Section 3.1 gives some theoretical background on how such an interaction takes place. Section 3.2 gives a detailed account on isotope-selective ionization process of ytterbium atoms. Trapping parameters and laser cooling are discussed in Sections 3.3 and 3.5 respectively. Section 3.6 demonstrates $^{171}Yb^{+}$ qubit by showing Rabi flops with a small ion cloud. Section 3.7 concludes this chapter with some remarks and future work.

3.1 Magnetic Dipole Transitions

Electromagnetic radiation can be used to operate on the qubit state, in which resonant optical fields drive optical qubit states while the hyperfine qubit states are driven by resonant microwave fields or by a pair of lasers detuned from each other by the qubit microwave frequency (Raman transitions) [24]. The following account on the magnetic dipole transitions is adopted from [4] and similar accounts using electric dipole moment appear in other references including [48, 49]. Since our system uses ytterbium hyperfine

qubits, we describe the physics of magnetic dipole allowed transitions. The perturbative Hamiltonian due to the radiation is given by,

$$\hat{H}_I = -\hat{\mu}_z B_0 \cos(\omega t + \delta_0) \tag{3.1}$$

with $\hat{\mu}_z$ as the z-component of the atom's magnetic moment, ω is the applied radiation angular frequency, B_0 is the amplitude of the radiation, and δ_0 is the phase. Considering small perturbation to the system, and expanding the system's wave function in terms of unperturbed Hamiltonian eigenstates we get,

$$|\psi(t)\rangle = \sum_m c_m(t) e^{-iE_m t/\hbar} |m\rangle \tag{3.2}$$

Substituting into the time-dependent Schrodinger equation we get,

$$i\hbar \dot{c}_n e^{-iE_n t/\hbar} = \sum_m c_m e^{-iE_m t/\hbar} \langle n| \hat{H} |m\rangle \tag{3.3}$$

with $\hat{H} = \hat{H}_0 + \hat{H}_1$, with $\hat{H}_0 |m\rangle = E_m |m\rangle$. In the magnetic dipole approximation, the wavelength of the magnetic radiation is much larger than the spatial extent of the atomic wave function and we can write $\langle n| \hat{H} |m\rangle = -B_0 \cos(\omega t + \delta_0) \langle n| \hat{\mu}_z |m\rangle$. The quantity $\langle n| \hat{\mu}_z |m\rangle$ is non-zero only for $n \neq m$ due to odd parity. We focus on a transition of the two-level system $|0\rangle$ and $|1\rangle$ such as one shown in Fig. 3.4 below whereby equation (3.3) above results in the following set of coupled differential equations,

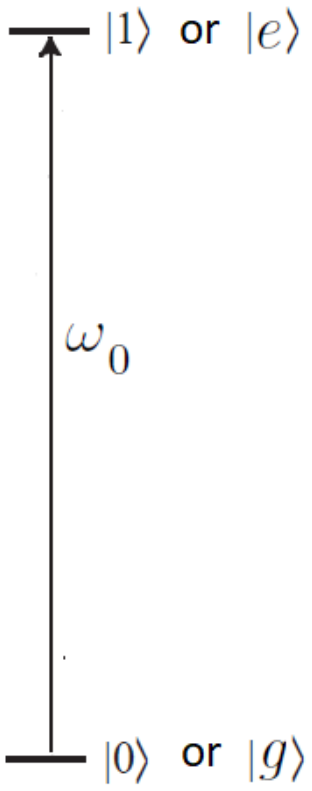

Fig. 3.4: Schematic level structure of a two level system.

$$i\hbar\dot{c}_0 = -c_1 d_{10} B_0 e^{-i\omega_{10}t}\cos(\omega t + \delta_0)$$
$$i\hbar\dot{c}_1 = -c_0 d_{10}^* B_0 e^{i\omega_{10}t}\cos(\omega t + \delta_0)$$

with $\omega_{10} = (E_1 - E_0)/\hbar$ and d_{10} as the magnetic dipole matrix element. In the rotating wave approximation we get the following,

$$\dot{c}_0 = -\frac{i\Omega}{2} c_1 e^{i(\triangle t + \delta_0)} \tag{3.4}$$
$$\dot{c}_1 = -\frac{i\Omega}{2} c_0 e^{-i(\triangle t + \delta_0)}$$

with $\Omega = \frac{d_{10}\cdot B_0}{\hbar}$ as the Rabi frequency, $\triangle = \omega - \omega_{10}$ is the detuning and ω is the laser frequency. Further algebra yields the following second differential equation,

$$\ddot{c}_1 + i\triangle\dot{c}_1 + \left|\frac{\Omega}{2}\right|^2 c_1 = 0$$

whose solution is given by,

$$c_1(t) = e^{-i\triangle t/2}(ae^{-i\Omega_R t/2} + be^{-i\Omega_R t/2}) \tag{3.5}$$

with $\Omega_R = \sqrt{\Omega^2 + \triangle^2}$ as the generalized Rabi frequency, a and b can be obtained from initial conditions. Given an ion that starts in the ground state $|0\rangle$ at time $t = 0$, with initial conditions $c_0(0) = 1$ and $c_1(0) = 0$, hence $b = -a$, we get,

$$c_1(t) = -2aie^{-i\triangle t/2}\sin(\Omega_R t/2)$$

From the initial conditions ($c_0(0) = 1$ and $c_1(0) = 0$) we arrive at the solution,

$$c_1(t) = \frac{i\Omega^*}{\Omega_R} e^{-i(\triangle t/2 + \delta_0)}\sin(\frac{1}{2}\Omega_R t)$$
$$c_0(t) = e^{i\triangle t/2}[\cos(\frac{1}{2}\Omega_R t) - \frac{i\triangle}{\Omega_R}\sin(\frac{1}{2}\Omega_R t)]$$

On the flip side ($c_1(0) = 1$ and $c_0(0) = 0$) the solution becomes,

$$c_0(t) = \frac{i\Omega}{\Omega_R} e^{i(\triangle t/2+\delta_0)} \sin(\frac{1}{2}\Omega_R t)$$
$$c_1(t) = e^{-i\triangle t/2}[\cos(\frac{1}{2}\Omega_R t) + \frac{i\triangle}{\Omega_R} \sin(\frac{1}{2}\Omega_R t)]$$

These two solution sets can be used to describe arbitrary microwave operations on the qubit. Any arbitrary initial state is simply a superposition of $|0\rangle$ and $|1\rangle$; e.g. $|\psi\rangle = \alpha|0\rangle + \beta|1\rangle$. The arbitrary operation $R_{\mu W}$ acting on $|\psi\rangle$ is then $R_{\mu W}|\psi\rangle = \alpha R_{\mu W}|0\rangle + \beta R_{\mu W}|1\rangle$. Thus, if we know the action of $R_{\mu W}$ on $|0\rangle$ and $|1\rangle$, we know the action of $R_{\mu W}$ on any state. If we write the states as matrices

$$|0\rangle = \begin{bmatrix} 1 \\ 0 \end{bmatrix} \quad \text{and} \quad |1\rangle = \begin{bmatrix} 0 \\ 1 \end{bmatrix}$$

Suppose the microwave operation matrix has these elements

$$R_{\mu W} = \begin{bmatrix} a_R & b_R \\ c_R & d_R \end{bmatrix}$$

Acting on the ground state we find,

$$\begin{aligned} R_{\mu W}|0\rangle &= \begin{bmatrix} a_R & b_R \\ c_R & d_R \end{bmatrix} \begin{bmatrix} 1 \\ 0 \end{bmatrix} = \begin{bmatrix} a_R \\ c_R \end{bmatrix} \\ &= \begin{bmatrix} e^{i\triangle t/2}[\cos(\frac{1}{2}\Omega_R t) - \frac{i\triangle}{\Omega_R}\sin(\frac{1}{2}\Omega_R t)] \\ \frac{i\Omega^*}{\Omega_R} e^{-i(\triangle t/2+\delta_0)} \sin(\frac{1}{2}\Omega_R t) \end{bmatrix} \end{aligned}$$

Again acting on the excited state we find

$$\begin{aligned} R_{\mu W}|1\rangle &= \begin{bmatrix} a_R & b_R \\ c_R & d_R \end{bmatrix} \begin{bmatrix} 0 \\ 1 \end{bmatrix} = \begin{bmatrix} b_R \\ d_R \end{bmatrix} \\ &= \begin{bmatrix} \frac{i\Omega}{\Omega_R} e^{i(\triangle t/2+\delta_0)} \sin(\frac{1}{2}\Omega_R t) \\ e^{-i\triangle t/2}[\cos(\frac{1}{2}\Omega_R t) + \frac{i\triangle}{\Omega_R}\sin(\frac{1}{2}\Omega_R t)] \end{bmatrix} \end{aligned}$$

The full microwave operation matrix acting on an arbitrary qubit state has the following form,

$$R_{\mu W} = \begin{bmatrix} e^{i\triangle t/2}[\cos(\frac{1}{2}\Omega_R t) - \frac{i\triangle}{\Omega_R}\sin(\frac{1}{2}\Omega_R t)] & \frac{i\Omega}{\Omega_R} e^{i(\triangle t/2+\delta_0)} \sin(\frac{1}{2}\Omega_R t) \\ \frac{i\Omega^*}{\Omega_R} e^{-i(\triangle t/2+\delta_0)} \sin(\frac{1}{2}\Omega_R t) & e^{-i\triangle t/2}[\cos(\frac{1}{2}\Omega_R t) + \frac{i\triangle}{\Omega_R}\sin(\frac{1}{2}\Omega_R t)] \end{bmatrix} \tag{3.6}$$

This microwave operation matrix rotates the Bloch vector on the Bloch sphere shown in Fig. 3.5 below.

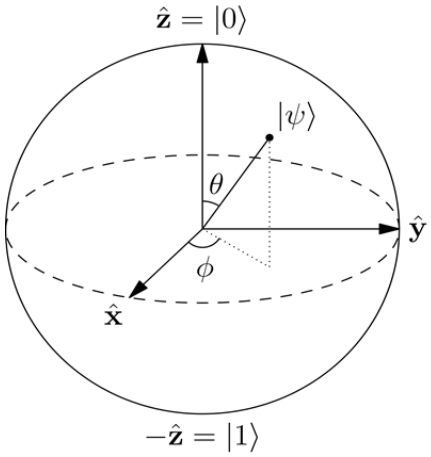

Fig. 3.5: Rotations on the Bloch sphere.

Rotations about the $y-$axis of the Bloch sphere correspond to $\delta_0 = 3\pi/2$, and we denote these by $R_y(\theta)$, where $\theta = \Omega_R t$ is the rotation angle. Rotations about the $x-$axis then correspond to $\delta_0 = \pi$ and we denote them as $R_x(\theta)$. Below we have on-resonance $(\triangle = 0)$ $\pi-$rotations and $\pi/2-$rotations:

$$
\begin{aligned}
R_y(\pi)\,|0\rangle &= |1\rangle \\
R_y(\pi)\,|1\rangle &= -\,|0\rangle \\
R_y(\frac{\pi}{2})\,|0\rangle &= \frac{1}{\sqrt{2}}(|0\rangle + |1\rangle) \\
R_y(\frac{\pi}{2})\,|1\rangle &= \frac{1}{\sqrt{2}}(-\,|0\rangle + |1\rangle)
\end{aligned}
$$

and

$$
\begin{aligned}
R_x(\pi)\,|0\rangle &= -i\,|1\rangle \\
R_x(\pi)\,|1\rangle &= -i\,|0\rangle
\end{aligned}
$$

$$
\begin{aligned}
R_x(\frac{\pi}{2})\,|0\rangle &= \frac{1}{\sqrt{2}}(|0\rangle - i\,|1\rangle) \\
R_x(\frac{\pi}{2})\,|1\rangle &= \frac{1}{\sqrt{2}}(-i\,|0\rangle + |1\rangle)
\end{aligned}
$$

Near resonance we have $\triangle \ll \Omega$, hence $\triangle/\Omega_R \approx 0$ and $\Omega/\Omega_R \approx 1$. In addition, this means that during the typical time of a microwave operation (order π/Ω) that the phase factor $e^{i\triangle t/2} \approx 1$. The microwave

rotations are implemented experimentally by generating 12.642812118466 GHz pulses with Rhode & Schwarz signal generator and sending the amplified signal into the trap through a vacuum chamber window with a microwave horn. The microwave horn can be re-oriented to optimize the coupling. The greater the power into the trap the bigger the Rabi frequency.

The selection rules for magnetic dipole transitions can be derived from the following relation, as outlined in [50],

$$A \propto \langle g| \hat{\mathbf{L}} + 2\hat{\mathbf{S}} |e\rangle \tag{3.7}$$

where $|g\rangle$, $|e\rangle$, $\hat{\mathbf{L}}$, $\hat{\mathbf{S}}$ are the ground state, excited state, total orbital angular momentum operator and total spin angular momentum operator respectively. A transition $|g\rangle \rightarrow |e\rangle$ is magnetic dipole allowed if the matrix elements of either total orbital angular momentum operator $\hat{\mathbf{L}}$ or total spin angular momentum operator $\hat{\mathbf{S}}$ are nonzero. The following is a list of these selection rules as summarized in [50],

(a). No change in electronic configuration,

(b). Parity is unchanged,

(c). $\triangle J = 0, \pm 1$,

(d). $\triangle M_J = 0, \pm 1$,

(e). $\triangle J = 0$ together with $\triangle M_J = 0$ is not allowed (in particular $J = 0 \leftrightarrow 0$ is not allowed),

(f). $\triangle L = 0$,

(g). $\triangle S = 0$.

where L, S, J and M_J are the orbital angular momentum, spin angular momentum, total angular momentum and its projection respectively.

3.2 Ytterbium Photoionization

Electron impact ionization was a widely used method of ionization in the early days of ion trapping and laser cooling, however, photoionization later took over as a preferred method of ionizing neutral atoms due to some advantages it offers, including its relatively high efficiency, no excess charge introduced in the trap as well as its ability to be isotope selective [51–54]. In [3] Yb atoms are singly ionized using the photoionization laser (398.9 nm) locked to fluorescence signal of a collimated atomic beam. The first 398.9 nm photon excites a transition $6s^2\ ^1S_0 \rightarrow 6s6p\ ^1P_1$ and the second 398.9 nm photon takes the electron close to the continuum where the field ionization by trap rf field (> 1000 V/cm) pushes the electron into the continuum. Alternatively, after the first 398.9 nm photon excites a transition $6s^2\ ^1S_0 \rightarrow 6s6p\ ^1P_1$,

a second photon ($\leq$ 394.5 nm) sends the electron into the continuum [3, 51]. These two photoionization approaches are shown in Fig. 3.6 below.

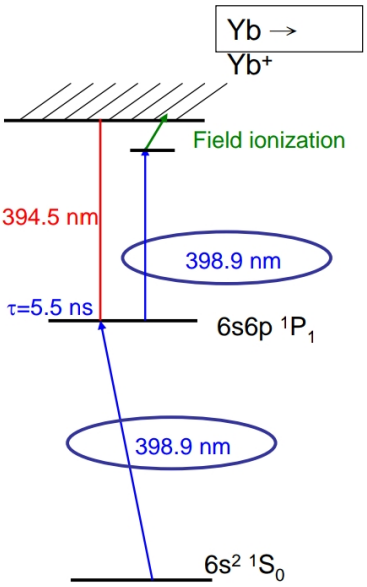

Fig. 3.6: Two ways to photoionize ytterbium atoms [3].

In [55, 56] a continuous-wave (CW) titanium-sapphire laser is used to generate, in second harmonic, 399 nm laser beam which excites the $6s^2\ {}^1S_0 \rightarrow 6s6p\ {}^1P_1$ transition in neutral ytterbium atoms. Another laser kicks the electron into the continuum which result in the ionization of ytterbium atom. The loading rate of ytterbium into the trap through photoionization is measured using the electric resonance detection of the secular motion of the trapped ytterbium ions. The electric resonance detection could be carried by driving the trapped ions on resonance with electric pulses applied on the trap electrodes and measuring their response by camera or PMT or by electrical image-current detection. A closely related experiment based on image current detection is proposed and explain in Chapter 4. The number of ions in the trap is estimated based on the measured loading rate. In [51] isotope selective two-photon ionization (369 nm and 399 nm), of neutral ytterbium atoms, that allows for efficient loading of ion traps with ytterbium ions. The ionization efficiency is compared with that of electron impact ionization. It is also demonstrated that nearly deterministic loading of a desired number of ions into a linear Paul trap is achievable.

Our strategy for trapping ions is to first produce neutral atoms inside the trapping volume and then photoionize them to achieve trapping. A beam of neutral Yb atoms is produced thermally and sprayed into the linear Paul trap by resistively heating one of our two neutral atom ovens. Each of our ovens is made of stainless steel hypodermic tubing that is bent in a $'U'$ shape with an opening in one corner to form a nozzle as shown in Fig. 3.7 below. Thin strips are cut from Ytterbium sheet and stuffed carefully into the needle resulting a loaded oven. The ovens are mounted on the side of the trap with nozzles facing towards the trap center and connected via an electrical feed-through to a current source outside the vacuum chamber. As the current passes through the oven, it heats up the oven resistively, thus, releasing a spray of neutral Ytterbium atoms into the trap.

Fig. 3.7: Ytterbium ovens.

These atoms are then ionized through photo-ionization which is a two-photon process. Upon reaching the trap center, first the atoms are hit with a continuous-wave (CW) Moglab diode laser beam tuned at 398.91 nm, to be on resonance with the ${}^1S_0 \leftrightarrow {}^1P_1$ transition of neutral Yb. The linewidth of this isotope selection laser is reported in its manual as < 100 kHz. The second laser beam is tuned to 369.53 nm, from a frequency-doubled CW laser source and drives the atom's electron into the continuum where background gas can easily kick it off thus, leaving behind an ionized Yb atom. That is, the 398.91 nm laser beam excites Yb atoms from the ${}^1S_0$ to the ${}^1P_1$ level, from which the 369.53 nm laser beam can promote the electron to the continuum as shown in Fig. 3.8 [4].

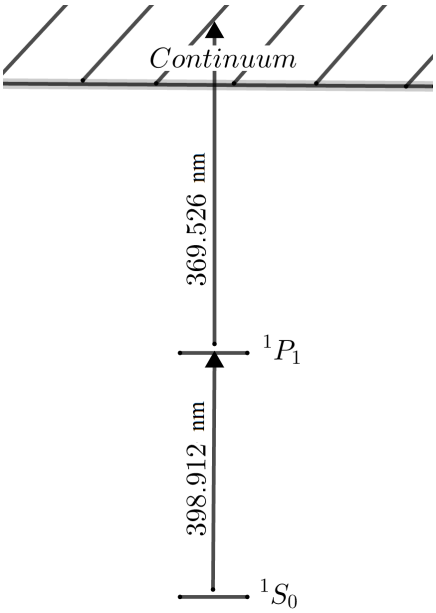

Fig. 3.8: Ytterbium Photoionization.

The atomic source ovens are aligned such that the propagation direction of the neutral Yb atoms is approximately perpendicular to the 398.91 nm beam to minimize Doppler shifts thus, favorable for isotopically selective loading. The 369.53 nm laser beam comes in at three different angles one of which is roughly perpendicular to the 398.91 nm beam while the other one is co-propagating with it. The 398.91 nm diode laser outputs about 4mW of which 0.2mW gets to one entrance window of the vacuum chamber. A second beam near 369.53 nm is generated by frequency-doubling the light produced by a cw amplified diode laser near 739.05 nm. Approximately 375 mW of 739.05 nm light is sent to a resonant cavity containing a critically phase-matched LBO crystal, producing more than 14 mW at 369.53 nm. One Yb oven is switched on at time by applying approximately 2 A from the current source. Scanning the isotope selection laser we were able to clearly distinguish different isotopes on the following wavelengths; 398.91080 nm, 398.91100 nm, 398.91114 nm, 398.91156 nm and 398.91170 nm. Moving from one wavelength to the next there was nothing loaded into the trap by photoionization and this explains how sensitive the photoionization was to this laser beam wavelength. The photoionization was insensitive to the scanning of the 369.53 nm laser wavelength as expected.

3.3 Trapping Parameters

Our RF supply for trapping consists of the function generator, generating a sine wave which is amplitude modulated externally to control the trap depth. We use external amplitude modulation to tune the amplitude since tuning the amplitude directly on the function generator make some voltage clicks which result in the loss of trapped ions. The voltage clicks could be caused by the function generator probably turning off the output to switch to a different gain regime as one tunes the output amplitude. The function generator feeds an rf power amplifier which in turn feeds a helical resonator that connects straight to the trap electrodes. A directional coupler is connected between the amplifier and the resonator to monitor the back-reflected voltage which calls for tuning of resonator coupling if too much back-reflection is observed. The resonance frequency of our helical resonator sits at about 28 MHz when unloaded and 16.04 MHz when loaded with the trap. The resonator has two probes coupling out its output for monitoring purposes. One probe is a built-in inductive probe while the other one is a detachable capacitive probe which is usually used for calibration purposes.

In one of our many successful trapping cases, after empirical searching through tuning of various parameters, we had our function generator set up for 16.04 MHz continuous sine wave with 4 Vpp and the inductive probe measured 5.04 V. This made the voltage at the trap electrodes to be around 227 V since the step-up ratio from the inductive probe to the resonator output measured 45. The back-reflection levels was around 600 mV. After some rough trap compensation the endcap electrode voltages were 50 V and 58 V while the compensation electrode voltages were both 200 V. The oven current was set at 2.1 Amp and the starting vacuum chamber pressure was $1.2E-10$ Torr. We observed that it helps to lower rf drive voltage amplitude all the way down and bring it up slowly in cases where trapping seems to be tricky. The ions resided in a two-coil magnetic field of about 3.4 Gauss, powered from a current source at 1 Amp, for defining the quantization axis.

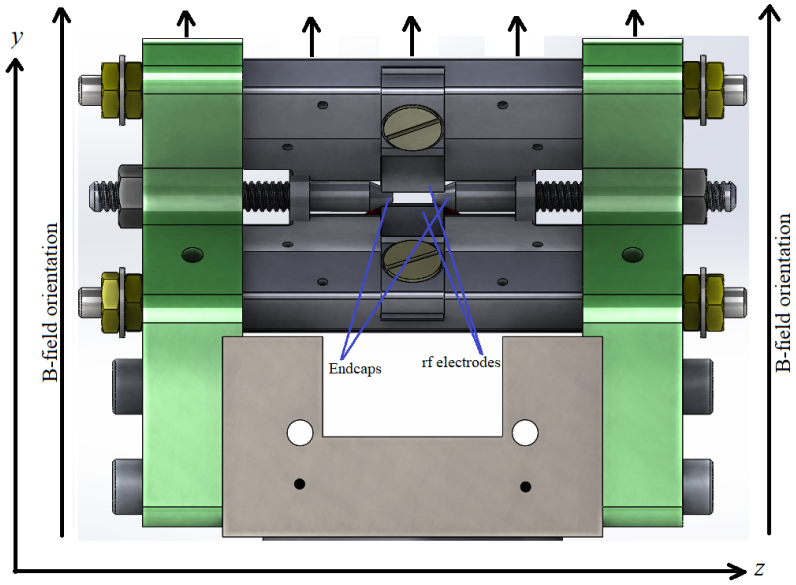

Fig. 3.9: The direction of magnetic field relative to the trap.

Fig. 3.9 above shows the magnetic field due to the two coils (one above and another below the trap respectively) is along the vertical or $y-$axis in relation to our trap.

3.4 Laser Beam Geometry

The laser beams enter the chamber through three different windows as shown in Fig. 3.10 below. The laser beam combination (Beam 1) going through the big window is horizontal and makes an azimuthal angle of about 20^0 with the trap axis. The laser beams at this window include the 369 nm, 638 nm and 935 nm laser beams. The laser beam combination (Beam 2) going through the medium window is horizontal and makes an azimuthal angle of about 70^0 with the trap axis. The laser beams at this window include the 369 nm, 398 nm, 638 nm and 935 nm laser beams.

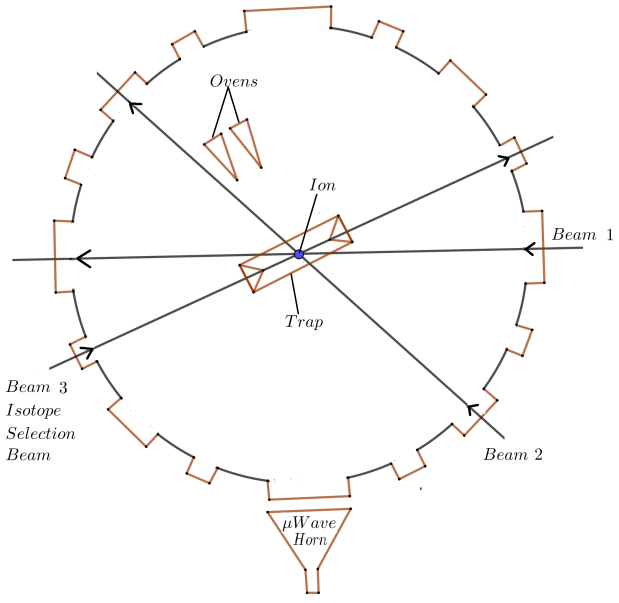

Fig. 3.10: Laser beams into the chamber.

This angle is preferable for Doppler cooling ions since it is almost perpendicular to ions motion along the trap axis. The laser beam combination (Beam 3) going through the small top window makes an angle of about 45^0 to the horizontal and is azimuthaly aligned with the trap axis as it goes through the trap center from above and exits underneath the trap. The laser beams at this window include the 369 nm, 398 nm, 638 nm and 935 nm laser beams. This direction of these laser beams makes a right angle with the direction of neutral atom beam thus, making this an ideal angle for isotope selective photoionization.

3.5 Doppler Cooling of Ytterbium Ion

A confined Yb^+ ion is Doppler-cooled with the 369 nm laser beam by slightly red-detuning it relative to the $^2S_{1/2} \leftrightarrow ^2P_{1/2}$ transition shown in Fig. 3.11 below.

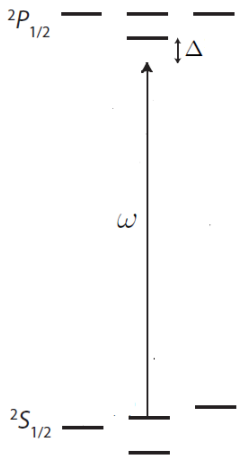

Fig. 3.11: The red-detuned 369 nm laser on the $^2S_{1/2} \leftrightarrow ^2P_{1/2}$ transition.

The photon scattering rate of the atom is affected by the laser frequency detuning and this is the key principle in Doppler cooling as shown below, [4]:

$$\Gamma_{sc} = \frac{\frac{I}{I_{sat}}\frac{\Gamma}{2}}{1 + \frac{I}{I_{sat}} + \frac{4\triangle_l^2}{\Gamma^2}}$$

with Γ_{sc}, Γ, I, I_{sat} and $\triangle_l$ as ion's scattering rate, spontaneous emission rate of the transition, incident laser beam intensity, saturation intensity and incident laser beam detuning respectively. Detuning the incident light to thee red of the transition's resonance, an atom moving towards the light will scatter more photons than it does while moving in the opposite direction and this allows a trapped ion to be cooled. It is favorable to setup the incident cooling laser beam such that is has non-vanishing spatial components in all of the principle axes of the trap, so that a single beam of incident light can cool the motion of trapped ions in all directions. With Doppler cooling it can be shown that the minimum temperature T_{Dmin} achievable is at a detuning $\triangle_l = -\Gamma/2$, and is given by,

$$T_{Dmin} = \frac{\hbar\Gamma}{2k_B}$$

The $^2S_{1/2} \leftrightarrow ^2P_{1/2}\, Yb$ transition yields a theoretical Doppler cooling limit of 470 μK. In the experiment, we typically Doppler cool the Ytterbium atom on the $^2S_{1/2} \leftrightarrow ^2P_{1/2}$ transition with 369.53 nm laser beam. Using only 369 nm laser beam to cool trapped ions is not efficient precisely because the $^2P_{1/2}$ state does not only decay to the $^2S_{1/2}$ level but also decays to the metastable $^2D_{3/2}$ level about 0.5% of the time. To remedy this problem an optical pumping laser beam at 935.2 nm is used to drive the ion from the $^2D_{3/2}$ to the $^3[3/2]_{1/2}$ level, from which it quickly decays back to $^2S_{1/2}$ level in the cooling transition. The trapped ion can also fall into the $^2F_{7/2}$ state and another optical pumping laser beam near 638.6 nm is used to depopulate the $^2F_{7/2}$ level, returning the ion back to the cooling cycle [57]. Fig. 5.7 below (from [4]) shows transitions involved during the Doppler cooling process of $^{171}Yb^+$.

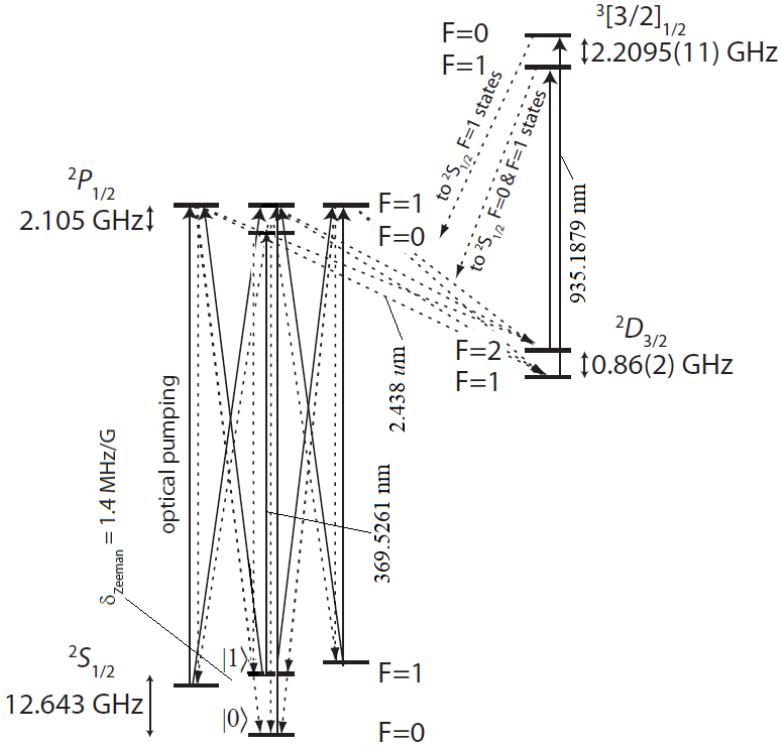

Fig. 3.12: Summary of the cooling cycle [4].

In the case of $^{171}Yb^+$ ion there is addition of the hyperfine structure. In this case off-resonance scattering in the Doppler cooling transition $^2S_{1/2}|F=1\rangle \leftrightarrow ^2P_{1/2}|F=0\rangle$ ends up populating the dark state $^2S_{1/2}|F=0\rangle$. To prevent this during cooling intervals, the 369.53 nm is passed through a 14.7 GHz resonant travelling wave Qubig (EO-WG14.7M2) EOM to generate sidebands 14.7 GHz away from the carrier 369.53 nm. The blue sideband drives the transition $^2S_{1/2}|F=0\rangle \leftrightarrow ^2P_{1/2}|F=1\rangle$ which brings the ion back to the cooling cycle. Population trapping in the $^2D_{3/2}|F=1\rangle$ manifold is avoided by application of a laser at 935.2 nm, which rapidly returns the atom to the cooling cycle via the transition $^2D_{3/2}|F=1\rangle \leftrightarrow ^3[3/2]_{1/2}|F=0\rangle$. The $^3[3/2]_{1/2}|F=0\rangle$ decays preferentially to $^2S_{1/2}$. About 600 uW of 935.2 nm light is sent into the trap, focused to a spot with waist approximately 200 μm. When the ion is excited off-resonantly to the $^2P_{1/2}|F=1\rangle$ manifold during cooling, the ion may decay to $^2D_{3/2}|F=2\rangle$. We depopulate this level by using a fiber EOM driven at 3.0695 GHz which adds sidebands on 935.2 nm light, one of which is resonant with the $^2D_{3/2}|F=2\rangle \leftrightarrow ^3[3/2]_{1/2}|F=1\rangle$ transition. Fig. 3.13 shows a schematic of 935 nm laser beam passing through the fiber EOM on its way to the trap.

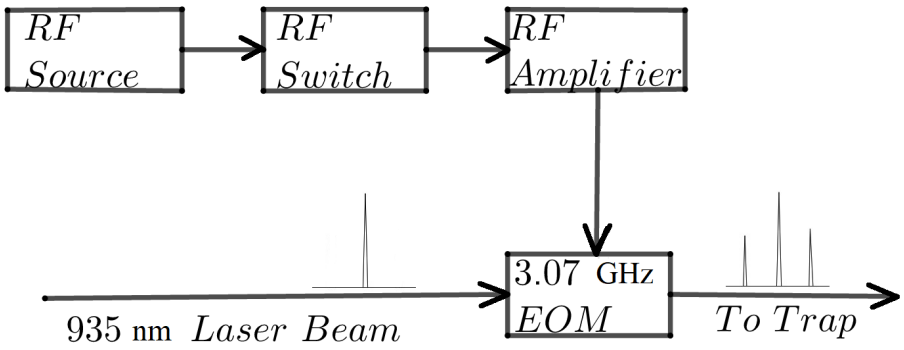

Fig. 3.13: Schematic of 935 nm laser beam through the 3.07 GHz EOM.

A Fabry-Perot and oscilloscope were used to observe the generated sidebands on the 935 nm beam. Fig. 3.14 below shows the sidebands generated on 935 nm laser beam.

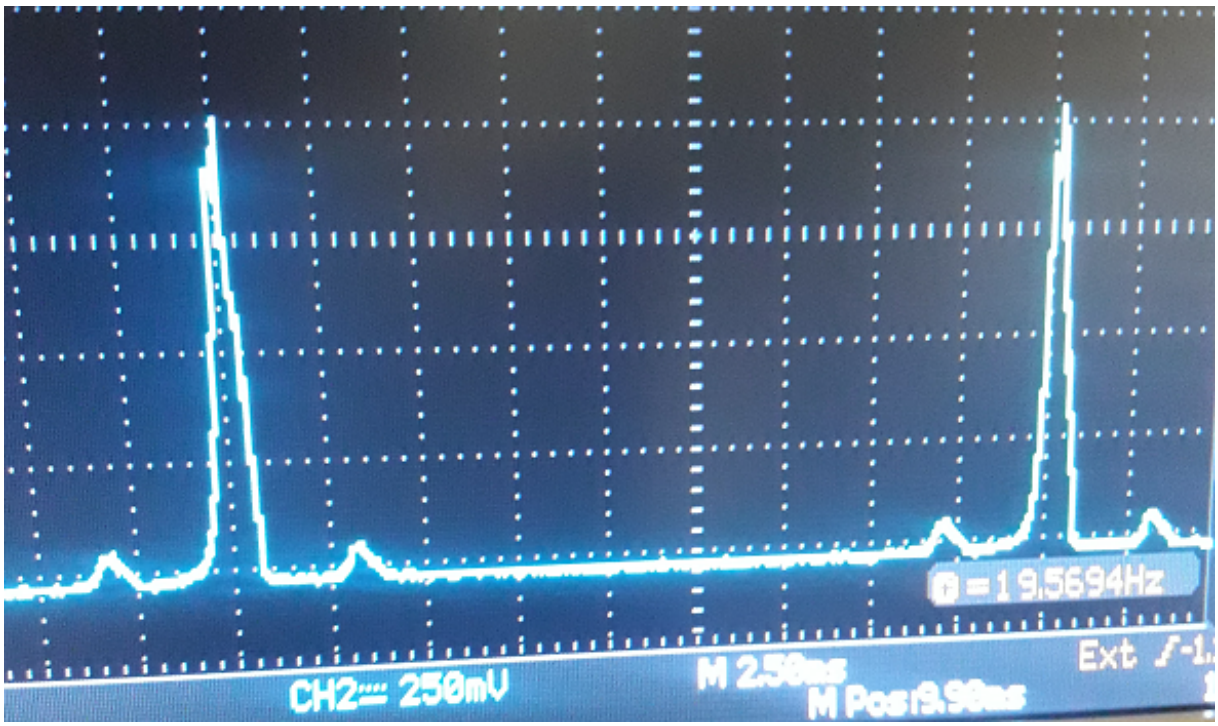

Fig. 3.14: 3.07 GHz EOM sidebands.

Finally the $^2F_{7/2}$ hyperfine levels are depopulated by laser light switched between 638.6102 nm and 638.6151 nm to drive the transitions $^2F_{7/2}|F=3\rangle \leftrightarrow^1 [5/2]_{5/2}|F=2\rangle$ and $^2F_{7/2}|F=4\rangle \leftrightarrow^1 [5/2]_{5/2}|F=3\rangle$ respectively. Nearly 1 mW of 638.6 nm light is present at the trap, focused to about 200 μm.

3.6 Ytterbium 171 Qubit

The odd isotopes of Ytterbium have a hyperfine structure which can be used for qubit realization [58]. For instance, $^{171}Yb^+$ ion has a level structure shown in Fig. 3.15 which shows hyperfine structure in the $^2S_{1/2}$ manifold. The transition $^2S_{1/2} \leftrightarrow^2 P_{1/2}$ is good for both state detection and Doppler cooling. In

this section we manipulate the trapped $^{171}Yb^{+}$ ion qubit with microwave pulses and demonstrate Rabi oscillations with a cloud of trapped ions. We note that, to our knowledge, this is the first demonstration of coherent manipulation of memory qubits in South Africa. To date the only other realization of qubits were in the form of entangled photons [59].

We abbreviate the hyperfine states $^2S_{1/2}|F=0\rangle$ and $^2S_{1/2}|F=1,m_F=0\rangle$ as qubit states $|0\rangle$ and $|1\rangle$ respectively. The presence of other transitions on Fig. 3.15 is indicative of the need for re-pumping and cooling cycle lasers. EOMs are required to switch on and off some sidebands during the experiments which involve four phases of cooling, state preparation, state evolution and state detection. These three phases are outlined next in an experiment aimed at demonstrating Rabi oscillations. A 369.53 nm laser beam is split into two beams each of which is double-passed through one of two AOMs resulting in two beams shifted by 220 MHz on second pass.

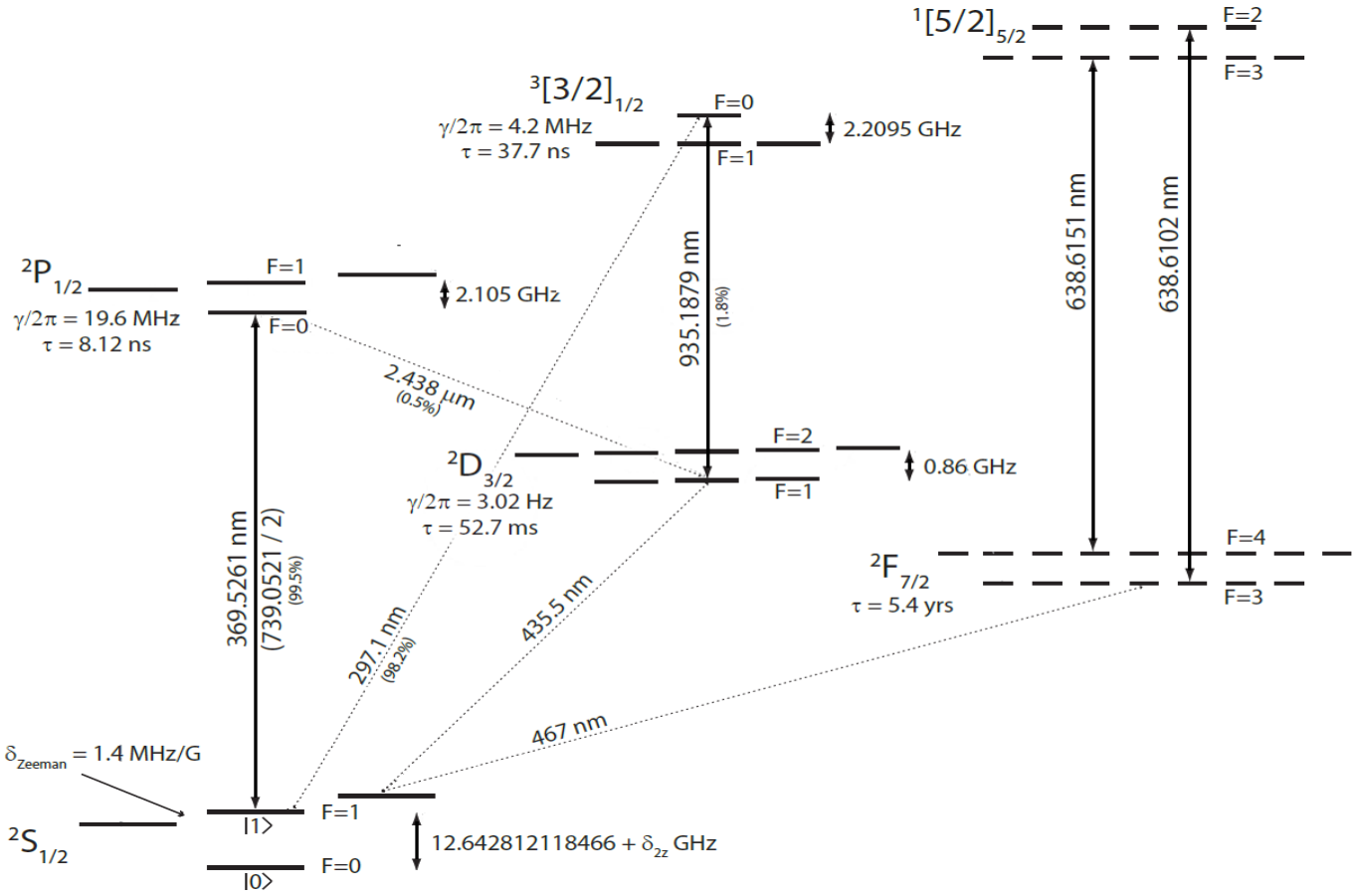

Fig. 3.15: Level structure for Yb 171 ion.

In our implementation the purpose of the AOMs is not necessarily to shift the laser frequency but rather to provide a switching control mechanism for the laser beam. That is, each of the two laser beams can be switched on and off independently using an FPGA program which controls the RF supply going to the AOMs.

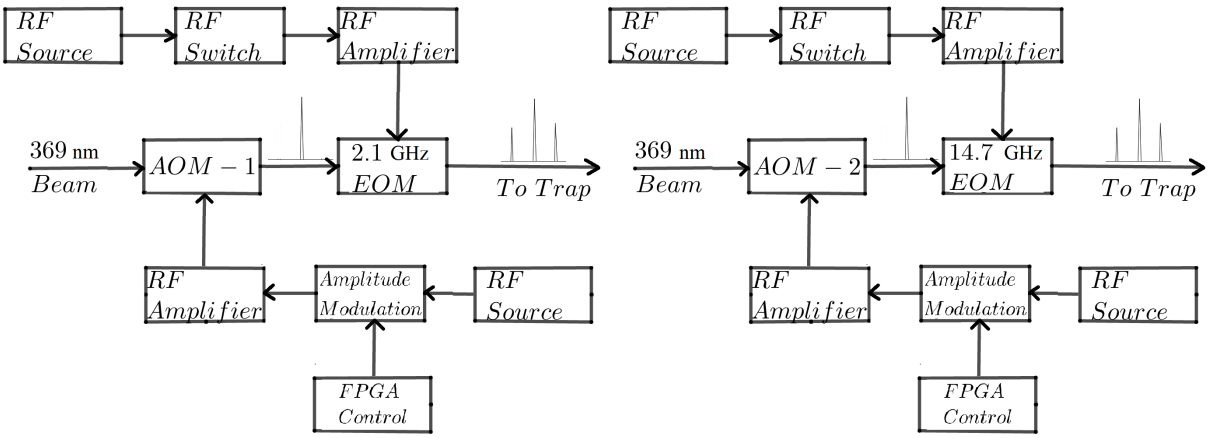

Fig. 3.16: Schematics of the 369 nm beam pathway through 2.1 GHz and 14.7 GHz EOMs to the trap.

One beam from the AOMs is passed through the 2.1 GHz Qubig (E0-T2100-M3) EOM, while the other beam is passed through a 14.7 GHz Qubig (EO-WG14.7M2) EOM to generate necessary sidebands before reaching the trapped ions. Fig. 3.16 shows the schematic of the 369 nm beam pathway through AOMs and EOMs on its way to the trap. Each of the EOMs has an rf supply and an FPGA-controlled rf switch. The rf switches allow the sidebands to be turned on and off independently through the FPGA program. Fig. 3.17 below shows the sidebands for both EOMs measured with a Fabry-Perot and oscilloscope.

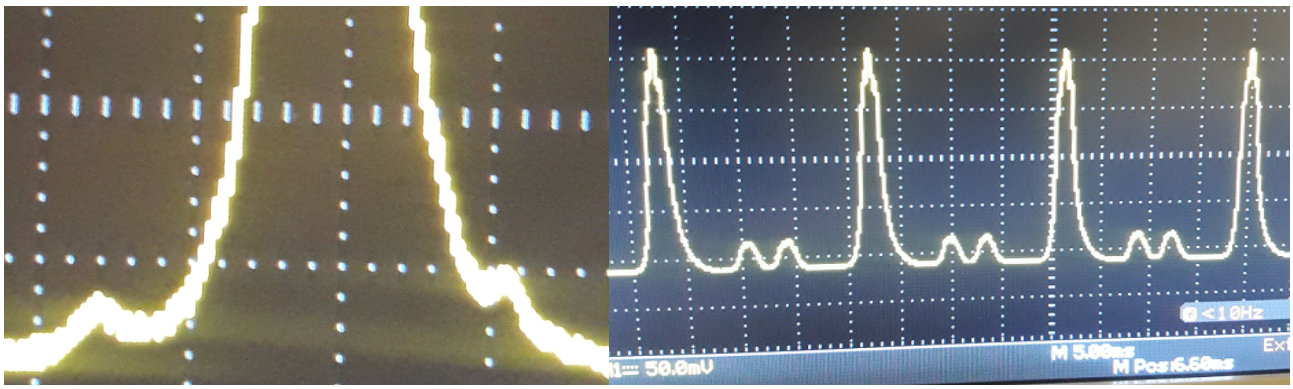

Fig. 3.17: Left: 2.1GHz sidebands on 369nm laser beam. Right: 14.7GHz sidebands on 369nm laser beam.

3.6.1 State Preparation

The aim of optical pumping in this stage of the experiment is to prepare the state of the $^{171}Yb^{+}$ qubit into the dark state $|0\rangle$. To prepare in the dark state the 14.7 GHz sidebands are turned off so that ions in the dark state do not get rescued out. Also the 2.1 GHz EOM is turned on for an efficient coupling/scattering to the $^{2}P_{1/2}|F=1\rangle$ level which then decays to the dark state. That is the EOM generates a blue sideband resonant with the transition $^{2}S_{1/2}|F=1\rangle \leftrightarrow^{2} P_{1/2}|F=1\rangle$. The 3.07 GHz EOM is also turned on to depopulate the metastable $^{2}D_{3/2}$ level as a means to facilitate efficient state preparation with high fidelity and so it does not get stuck there. Fig. 3.18 below gives a summary of involved transitions during state preparation [4].

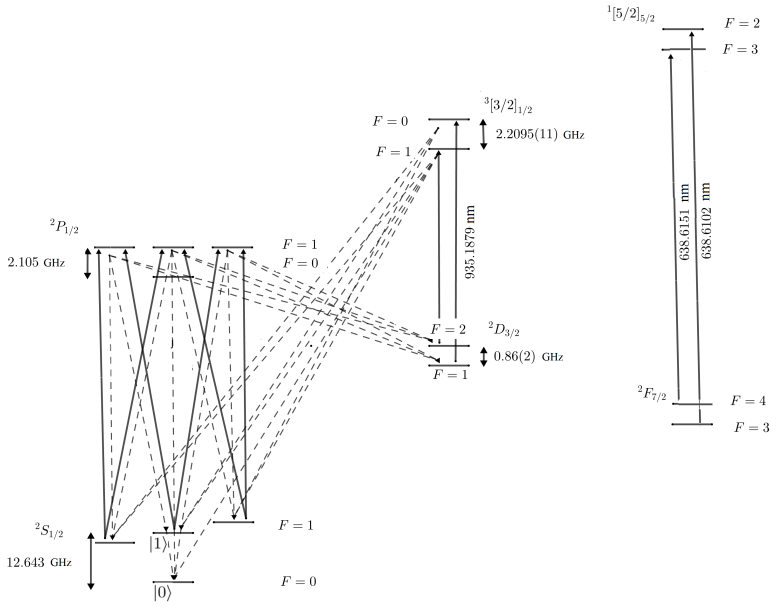

Fig. 3.18: State preparation into the dark state.

In our Rabi oscillations experiment we state-prepared for 100 μs after cooling for 100 ms.

3.6.2 State Evolution

As explained in Section 3.1, we can rotate the state of the ion between $|0\rangle$ and $|1\rangle$ by applying microwaves resonant with the 12.643 GHz transition in $^2S_{1/2}$ manifold. Fig. 3.19 below shows the evolution of qubit state back and forth between these two states.

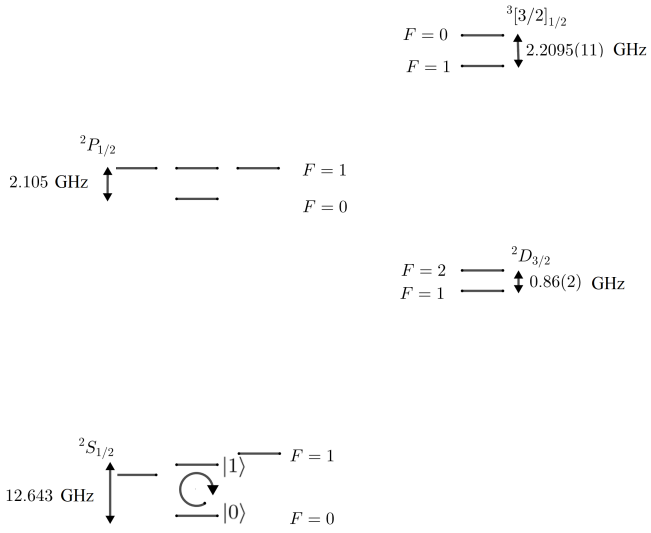

Fig. 3.19: State evolution with the microwaves.

We apply these microwave pulses for varying times to trace out the evolution of the qubit state. In our experiment we start with a microwave duration of zero seconds and keep incrementing by 1 μs. For each time increment we made 50 measurements and averaged them before introducing another time increment. And for each measurement we cool, state prepare, state evolve and state detect. During state

evolution both the 14.7 GHz EOM and 369 nm laser beam are is switched off so as to avoid creating a pathway for ions out of the $|0\rangle \longleftrightarrow |1\rangle$ state evolution transition. The 2.1 GHz EOM was also off but that does not matter much. The 369 nm laser beam was turned on and off using the AOMs instructed by the FPGA program.

3.6.3 State Detection

A critical step in quantum computation and communication protocols is detection of the qubit state. In ytterbium 171 ion, state detection is accomplished using standard ion fluorescence techniques. The 369.53 nm light of the detect beam is tuned to be nearly on resonance with the $^2S_{1/2}|F=1\rangle \leftrightarrow ^2P_{1/2}|F=0\rangle$ transition. Fig. 3.20 below shows the involved transitions during state detection [4]. If the ion is prepared in the $|0\rangle$ state, this incident light is detuned from $^2P_{1/2}|F=1\rangle$ by 14.7 GHz, and thus, the ion scatters very few photons. The state of the ion is determined by the number of photons observed by the PMT (setup as shown in Fig. 1.6 and Fig. 1.4) during the detection interval.

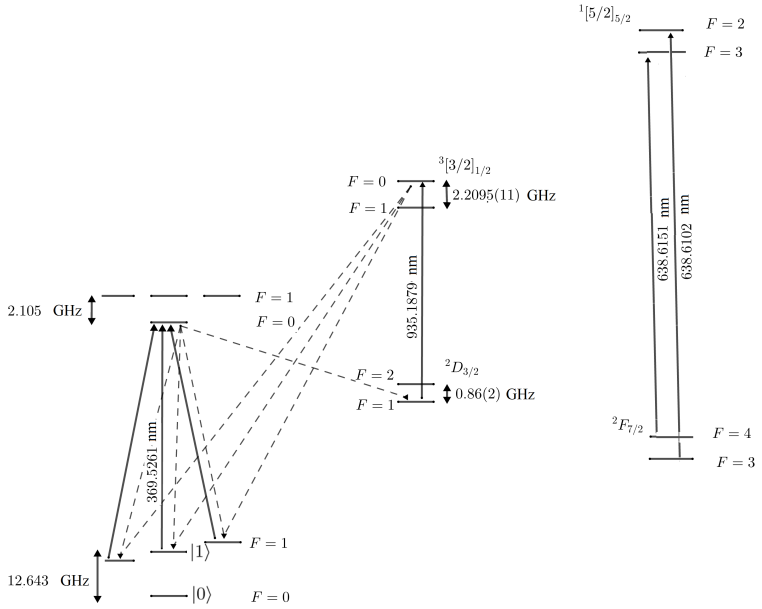

Fig. 3.20: State detection with 369*nm* laser.

Since the initial state is $|0\rangle$, the incident light is detuned from the $^2P_{1/2}|F=1\rangle$ manifold by 14.7 GHz and transitions to the $^2P_{1/2}|F=0\rangle$ level are forbidden by selection rules. Taking into account decay into the $^2D_{3/2}$ level in this calculation reduces the total number of 369.53 nm photons scattered by the ion. In addition, off-resonant coupling to the $^3[3/2]_{1/2}|F=1\rangle$ level may occur while depopulating the $^2D_{3/2}|F=1\rangle$ manifold.

3.6.4 Rabi flops

Fig. 3.21 below shows the Rabi oscillation produced by the experiment described above with time steps (for microwave pulse duration) of 1 μs, cooling time of 100 ms, state preparation time of 100 μs and

state detection time of 10 ms. The working laser wavelengths were parked (free running) at 398.91095 nm, 638.614 nm, 739.0524 nm and 935.1878 nm while the pressure was 1.50×10^{-9} Torr. This is about two orders of magnitude higher pressure than an intended target of $\sim 10^{-11}$ Torr. At this 1.50×10^{-9} Torr pressure, when trapping a few ions in a cooled crystal, one observes frequent crystal rearrangements which we interpret as a result of collisions with background gas molecules and the repeatative heating and cooling of ions by free running (i.e. unlocked) 739.0524 nm laser. The Rabi oscillations curve below has a decaying amplitude which we attribute not to loss of coherence, but rather to loss of ions from the trap as a consequence of chemistry with the background gas molecules. We conclude this firstly because we expect the coherence time of the ion to be significantly longer since we are driving a clock transition and our microwave source is locked to Stanford Research Systems FS725 Rubidium Atomic clock. And secondly, because loss of coherence should lead to a loss of oscillation contrast that tends to the halfway point between maximum and minimum fluorescence, rather than damping out completely. We lost the whole cloud at around 286 μs, however, the Rabi oscillations are clearly evident with a period of 34.7 μs approximately.

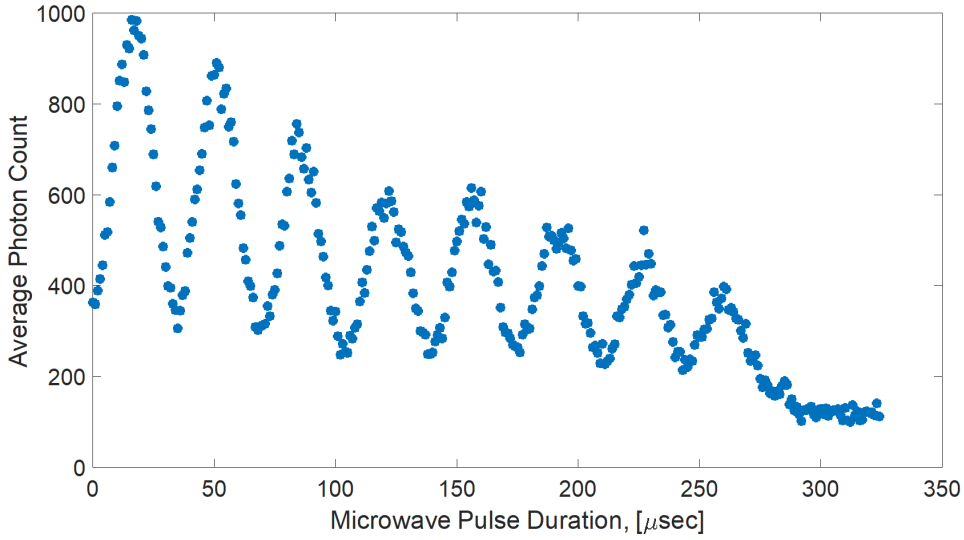

Fig. 3.21: $^{171}Yb^{+}$ Rabi flops.

In this experiment the initial total fluorescence count in 10 ms of fluorescence collection was ~1160 photon counts, with a background count of ~130 photons. The Rabi oscillation in Fig. 3.21 clearly do not attain full contrast oscillations between these two limits. This indicates that we likely have imperfect initial state preparation, and that quantum state of the ions is best described by a mixed state density matrix at the beginning of the experiment. In other words, some (classical) fraction of the ions remain in the upper state at the end of the optical pumping step. To properly interpret the dynamics mathematically we have to adapt the wavefunction description at the beginning of the chapter to the density matrix picture. To that end we define the following variables

$$\begin{aligned} \tilde{c}_0 &= c_0 e^{-i\triangle t/2} \\ \tilde{c}_1 &= c_1 e^{i\triangle t/2} \end{aligned} \tag{3.8}$$

and substitute them in equation set (3.4) to obtain,

$$\begin{aligned} \dot{\tilde{c}}_0 &= -\tfrac{i}{2}(\triangle\tilde{c}_0 + \Omega\tilde{c}_1\exp(i\delta_0)) \\ \dot{\tilde{c}}_1 &= -\tfrac{i}{2}(\Omega\tilde{c}_0\exp(-i\delta_0) - \tilde{c}_1\triangle) \end{aligned} \tag{3.9}$$

We now define a density matrix $\rho(t)$ as follows,

$$\rho(t) = \begin{bmatrix}\tilde{c}_0 \\ \tilde{c}_1\end{bmatrix}\begin{bmatrix}\tilde{c}_0^* & \tilde{c}_1^*\end{bmatrix} = \begin{bmatrix}|\tilde{c}_0|^2 & \tilde{c}_0\tilde{c}_1^* \\ \tilde{c}_1\tilde{c}_0^* & |\tilde{c}_1|^2\end{bmatrix} = \begin{bmatrix}\rho_{00} & \rho_{01} \\ \rho_{10} & \rho_{11}\end{bmatrix} \tag{3.10}$$

with ρ_{00} and ρ_{11} as percentage populations for ground and excited states respectively, ρ_{01} and ρ_{10} are associated with coherence. Using equation sets (3.8), (3.9) and equation (3.10) we obtain the following set of first order differential equations in density matrix elements,

$$\begin{aligned} \dot{\rho}_{11} &= -\dot{\rho}_{00} = 2\tilde{c}_1\dot{\tilde{c}}_1^* = \tfrac{i\Omega}{2}(\rho_{10}\exp(i\delta_0) - \rho_{01}\exp(-i\delta_0)) \\ \dot{\rho}_{01} &= \dot{\rho}_{10}^* = \tilde{c}_0\dot{\tilde{c}}_1^* + \dot{\tilde{c}}_0\tilde{c}_1^* = -\triangle\rho_{10} + \tfrac{i\Omega}{2}\exp(i\delta_0)(\rho_{00} - \rho_{11}) \end{aligned} \tag{3.11}$$

From equation set (3.11) we can arrive the following set of equations (by setting $\exp(\pm i\delta_0) = 1$ and $\triangle = 0$ i.e on-resonance excitation) which is similar in form to equation set (7.42) in [48].

$$\begin{aligned} \tfrac{d\rho_{01}}{dt} &= \tfrac{d\rho_{10}^*}{dt} = i\tfrac{\Omega}{2}(\rho_{00} - \rho_{11}) \\ \tfrac{d\rho_{11}}{dt} &= -\tfrac{d\rho_{00}}{dt} = i\tfrac{\Omega}{2}(\rho_{10} - \rho_{01}) \end{aligned} \tag{3.12}$$

with Ω as the Rabi frequency. The previous set of equations can be rewriten as the following second order differential equation in ρ_{11},

$$\frac{d^2\rho_{11}}{dt^2} + \Omega^2\rho_{11} - \frac{\Omega^2}{2} = 0 \tag{3.13}$$

Solving this second order differential equation (with initial conditions $\rho_{11}(t=0) = a$, $\frac{d}{dt}\rho_{11}(t=0) = 0$) we obtain the following solution,

$$\rho_{11} = \frac{1}{2}((2a-1)\cos(\Omega t) + 1) \tag{3.14}$$

To account for the ion loss from our cloud we consider $N(t)$ ions at time t in the cloud and assume the ion loss rate due to collisions is proportional to the number of ions. In other words,

$$\frac{dN}{dt} = -\frac{N}{\tau} \tag{3.15}$$

whose solution is given by,

$$N(t) = N_0 \exp(-\frac{t}{\tau}) \tag{3.16}$$

Multiplying equations (3.13) and (3.16) we obtain the fraction of ions $N(t)\rho_{11}(t)$ in the excited state and and this quantity is proportional to the average photon count $P_c(t)$,

$$P_c(t) = N(t)\rho_{11}(t) = \frac{N_0}{2}\exp(-\frac{t}{\tau})((2a-1)\cos(\Omega t)+1)+P_{c0} \tag{3.17}$$

The model in equation (3.17) above was used to fit the average photon count data, with $P_c(t)$ being the average photon count as function of microwave pulse duration, t. Fig. 3.22 below shows the plot of the data along with the fitting model as described by equation (3.17).

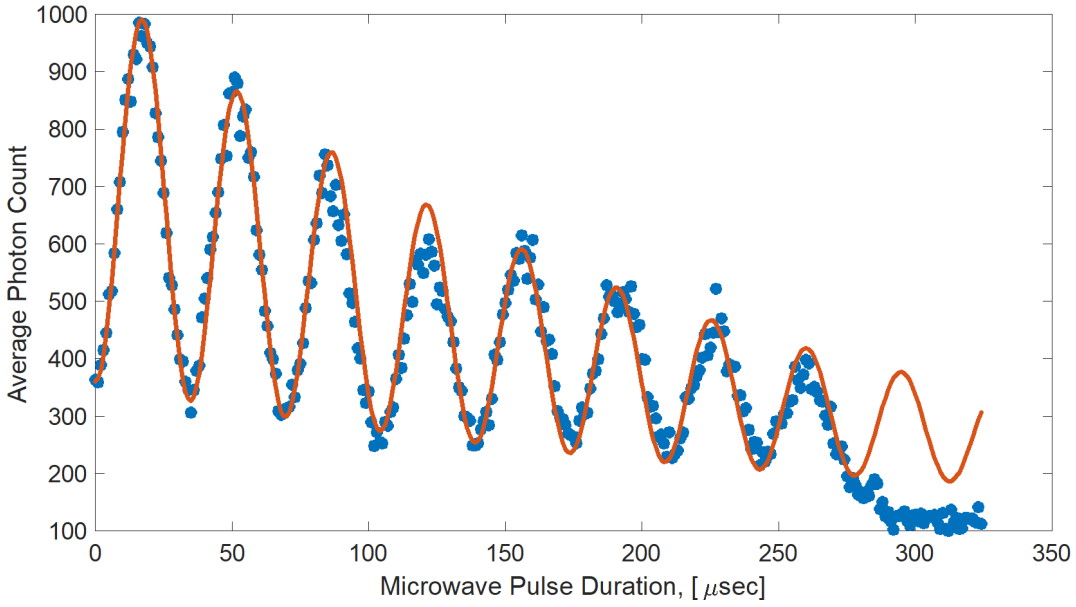

Fig. 3.22: $^{171}Yb^{+}$ Rabi flops.

The initial cloud was composed of approximately $N_0 = 1160$ photons (i.e. at $t = 0$ sec). Time constant $\tau = 4500^{-1}$ seconds is related to the time it takes ions to be lost from the trap, Rabi frequency $\Omega = 181$ kilorad/s, the percentage of initial ions in the excited state was $a = 230/N_0$ and the average background photon count $P_{c0} = 130$ photons.

A different approach to the timing of our measurements would allow us to see longer lived oscillations even in the presence of the ion loss, albeit with reduced initial amplitude. Instead of taking 50 measurements at one point in time and averaging those measurements before stepping in time to the next point, we propose to take one measurement per point and only after completing the trajectory do we repeat the measurements tracing out another trajectory until we have 50 trajectories to average. In this way the misfortune of ion loss is distributed almost evenly across the trajectory instead of only towards the end of the trajectory.

3.7 Summary

In this chapter we have presented the dynamics of interactions between laser radiation and a confined atom or ion. Laser beams were setup and aligned in a way to allow for isotope selective photoionization of Yb atoms as a two photon process involving 398 nm and 369 nm laser. The cooling laser beam was made present at various angles to allow for Doppler cooling in different modes. The manipulation of $^{171}Yb^{+}$ qubit with microwaves was also demonstrated in the Rabi flops experiment which involved a repetition of Doppler cooling, state preparation with the help of the 2.1 GHz EOM, state evolution with microwaves and state detection with 369 nm laser fluorescence scattering captured by the PMT for enhancement. To our knowledge, this is the first realization and demonstration of coherent manipulation of trapped ion memory qubits in South Africa.

Chapter 4

Image Current-based Ion Detection

In this chapter we discuss an alternative method of ion detection which is based on detecting image current induced by an oscillating trapped ion on nearby electrodes. This alternative detection method is currently being investigated and implemented in our lab with a look towards future work. This tool is expected to open several new avenues of investigation including feedback cooling, pressure sensing, and potentially even qubit state detection if single ion image current detection can be achieved. Analysis of the methods of image current amplification and filtering flows naturally from the tools developed in earlier chapters to characterize resonators for the rf trapping fields. It is worth mentioning that this method is commonly used in Penning traps which usually trap a larger number of ions than Paul traps hence leading to stronger image current for detection. This is because the strength of the image current signal scales with the number of ions (or amount of charge) oscillating coherently inside the trap as will be shown by equation (4.7) relating signal to noise ratio to other parameters in later sections.

There are actually two contributions to the total current due to an oscillating ion in the trap. One contribution is due to mutual inductance between oscillating ion and the nearby trap electrodes. This current contribution only exists if the ion is accelerating (or decelerating). The second contribution is due to charge of the trapped ion being imaged into the nearby trap electrodes. As the ion moves (not necessarily accelerating) its image in the electrodes also moves thus, generating imaging current on the electrodes. Throughout this chapter these two contributions are together loosely termed “image current”.

The next section gives some background on ion detection techniques and elaborate more on image current technique, coupling out and enhancing detected image current. Section 4.2 gives some thoughts on the tickling experiment (in which ions are motionally excited with some rf signal at the secular frequency) and signal enhancement recommended for future work. Subsequent sections point out some new developments in our trap to enable a more efficient detection of image current based on proximity of probes to trapped ions. A transimpedance amplifier is tested with a dummy signal to determine the threshold current which gives out a detectable signal on the spectrum analyzer. This chapter concludes with a summary in Section 4.5.

4.1 Ion Detection With Image Current

The methods used for ion detection can be classified as destructive and non-destructive methods. Destructive methods do not conserve the ion count since they detect ions by causing a partial destruction of ion sample. In some experiments however, destructive detection methods may not be preferable perhaps because one hopes to repeatedly detect some property of the ion continuously in real-time without losing that ion. As explained in [60], the choice of detection method is contingent upon a number of technicalities including the ion species, its sample size, trap dimensions, the environment, dynamics and intended experiment. For instance, some trapped ion species cannot be made visible by resonant laser excitation for various reasons such as difficulty in getting lasers with the right wavelength or lack of a closed fluorescence cycle to give sufficiently large number of scattered photons. Such a challenge demands experimenters to opt for an alternative, and more convenient, detection scheme.

In [60] various electronic detection techniques, together with the corresponding electronic instruments, are presented in details. These encompass both destructive and non-destructive detection techniques. Some destructive detection techniques addressed therein include ion loss, depletion techniques and ejection techniques, among others, which all share the same feature of losing a fraction of ion from the trap and have them picked up by some detector apparatus. The non-destructive detection technique addressed is one that makes use of image currents induced on trap electrodes by the oscillating trapped ions. This image current can then be picked up by some appropriate circuitry from the trap electrodes. This detection method is non-destructive in the sense that the presence of trapped ions can be detected without any loss of some ions from the ion trap thus, preserving the trapped ions for further detection rounds.

The image current detection technique presented in [61–63] is based on detecting the image current induced on one trap electrode which is the picked up from the electrode for further processing. On the other hand in [60,64,65] a differential detection is considered which is given by measuring image current from two opposite electrodes (i.e. endcaps). This way of measuring the image current differentially across a pair of two opposing electrodes is advantageous for a few reasons, one being that the common mode noise occurring in both detector electrodes is reduced by subtraction. Another important reason is that the image current induced on these two electrode pair is 180^0 out of phase with respect to each other, given that the ions oscillate coherently, and this lead to an increase in measured signal strength in a differential mode compared to a non-differential mode of measurement.

In [66] the differential measurement is setup in a similar fashion to resistive cooling whereby a resistor is connected across the endcap electrodes. With resistive cooling this resistor serves to dissipate the energy due to image current on the electrodes induced by oscillating trapped ions. As a non-destructive detection technique, the resistor serves to as a current to voltage converter whereby the detected signal is picked up as the voltage across the resistor. Since this voltage is typically minute the authors suggest making the electrodes part of a high Q resonant circuit. In so doing, the presence of oscillating ions in the trap will be witnessed by the lowering of the circuit Q factor as the energy is absorbed from the circuit. From [63] the image current induced on the trap electrode by the ion of charge e moving at the velocity $\mathbf{v}$ is given by;

$$I_i = e\mathbf{E}_i(\mathbf{r}) \cdot \mathbf{v} \tag{4.1}$$

where $\mathbf{E}_i$ is the electric field on the electrode due to the ion a distance of $\mathbf{r}$ away. The corresponding induced charge is $q_i = -e\mathbf{E}_i(\mathbf{r})$. In [64] an attempt is made to model the ion-endcaps setup as a resonant circuit driven by some noisy voltage source as shown in Fig. 4.1 below. The induced charge in then given by;

$$q_i = \frac{\alpha_i e z_i}{d_i}$$

with z_i as the axial displacement of the ion from its equilibrium position, d_i is the separation between the electrodes and α_i as a geometrical factor of order unity.

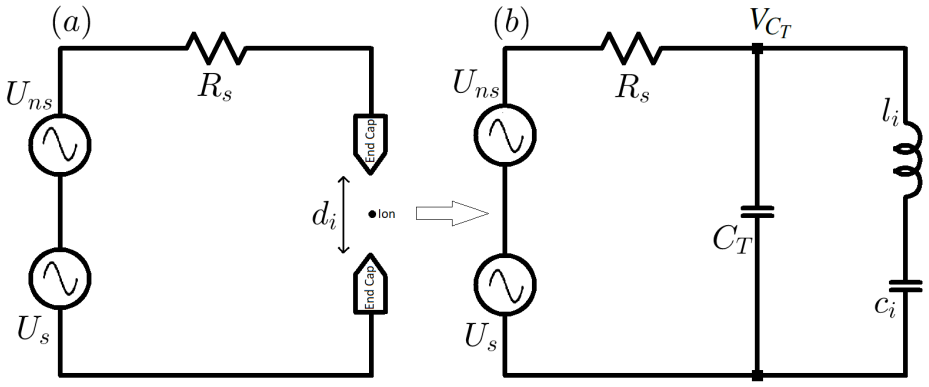

Fig. 4.1: Modeling the ion-endcaps setup as a driven resonant circuit.

In this figure U_s is the voltage source and U_{ns} is the voltage noise source. The trapped ion and its induced current can be shown to be electrically equivalent to to a series LC circuit which shunts the endcaps and the corresponding inductance and capacitance are given by

$$\begin{aligned} L_i &= m_i(d_i/\alpha_i e)^2 \\ C_i &= (\omega_i^2 L_i)^{-1} \end{aligned}$$

where m_i is the mass of an ion and ω_i is the resonance frequency. Under some mild assumptions ($R_s \ll (\omega_i^2 C_T)^{-1}$) the effect of trap capacitance C_T can be neglected thus, resulting in a damped oscillator which can be described quantum mechanically as follows;

$$\begin{aligned} \dot{\hat{a}}_i &= -(i\omega_i + \gamma/2)\hat{a}_i + \hat{f}_n(t) + \hat{f}_s(t) \\ \dot{\hat{a}}_i^\dagger &= (i\omega_i - \gamma/2)\hat{a}_i^\dagger + \hat{f}_n^\dagger(t) + \hat{f}_s^\dagger(t) \end{aligned} \tag{4.2}$$

where $\hat{f}_n(t)$ and $\hat{f}_s(t)$ are the operators associated with the source terms U_{ns} and U_s respectively. The damping rate γ of the oscillator is give by $\gamma = R_s/L_i$. The operators $\hat{a}_i^\dagger$ and $\hat{a}_i$ are the creation and

annihilation operators respectively and together they give the induced charge operator $\hat{q}_i$ on the trap electrode as follows;

$$\hat{q}_i = \sqrt{\frac{\hbar}{2\omega_i L_i}}(\hat{a}_i^\dagger + \hat{a}_i) \tag{4.3}$$

The mean number of quanta $\langle \hat{n}_i \rangle = \left\langle \hat{a}_i^\dagger \hat{a}_i \right\rangle$ in the circuit at time t_m is given by;

$$\langle \hat{n}_i(t_m) \rangle = \langle \hat{n}_i(0) \rangle e^{-\gamma t_m} + \bar{n}(1 - e^{-\gamma t_m}) + \frac{|u_{s0}|^2}{2\hbar\omega_i \gamma^2 L_i}(1 - e^{-\gamma t_m/2})^2 \tag{4.4}$$

with u_{s0} associated with the source terms. The authors of [64] point out the measurement of this absorbed quanta as another alternative to measuring ion presence in the trap. More details on this approach of modeling the detection and further developments of it can be found in [64]. Looking closely at this circuit one can describe it with the following transfer function relating the input voltage U_s with voltage V_{C_T} across the inductor L_i and capacitor C_i,

$$H(s) = \frac{V_{C_T}}{U_s} = \frac{s^2 L_i C_i + s r_i C_i + 1}{s^3 R_s L_i C_i C_T + s^2(r_i R_s C_i C_T + L_i C_i) + s(r_i C_i + R_s(C_i + C_T)) + 1} \tag{4.5}$$

with r_i as the parasitic resistance of the inductor L_i. The above transfer function models the dynamic voltage or potential response of a trapped ion due to an applied input voltage on the electrode pair. From the transfer function it is clear that there are two resonances contributed by the zeros polynomial as well as the poles or characteristic polynomial. The bandstop resonance response due to the zeros polynomial occurs at the frequency $\omega_i = \frac{1}{\sqrt{L_i C_i}}$ with selectivity $Q_i = \frac{1}{r_i}\sqrt{\frac{L_i}{C_i}}$. The bandpass resonance, due to the characteristic polynomial, occurs at the frequency

$$\omega_0 = \frac{Q_0}{3aG}(2bG + 3ac - G^2 - b^2) = \omega_i \sqrt{1 + \frac{R_s^2 C_i C_T}{R_s^2 C_T^2 + L_i C_i - r_i R_s C_i C_T}}$$

with selectivity

$$Q_0 = \sqrt{\frac{3(G - b^2 + 3ac)^2 + (G^2 - 2bG + b^2 - 3ac)}{4(G^2 - 2bG + b^2 - 3ac)}} = \frac{\omega_0^3 R_s C_T}{\omega_0^2(\omega_i^2 r_i R_s C_i C_T + 1) - \omega_i^2}$$

and the following constants;

- $a = R_s L_i C_i C_T$, $b = r_i R_s C_i C_T + L_i C_i$,
- $c = r_i C_i + R_s C_i + R_s C_T$, $d = 1$,
- $F = \sqrt{(2b^3 - 9abc + 27a^2 d)^2 - 4(b^2 - 3ac)^3}$ and
- $G = \sqrt[3]{0.5(F + 2b^3 - 9abc + 27a^2 d)}$.

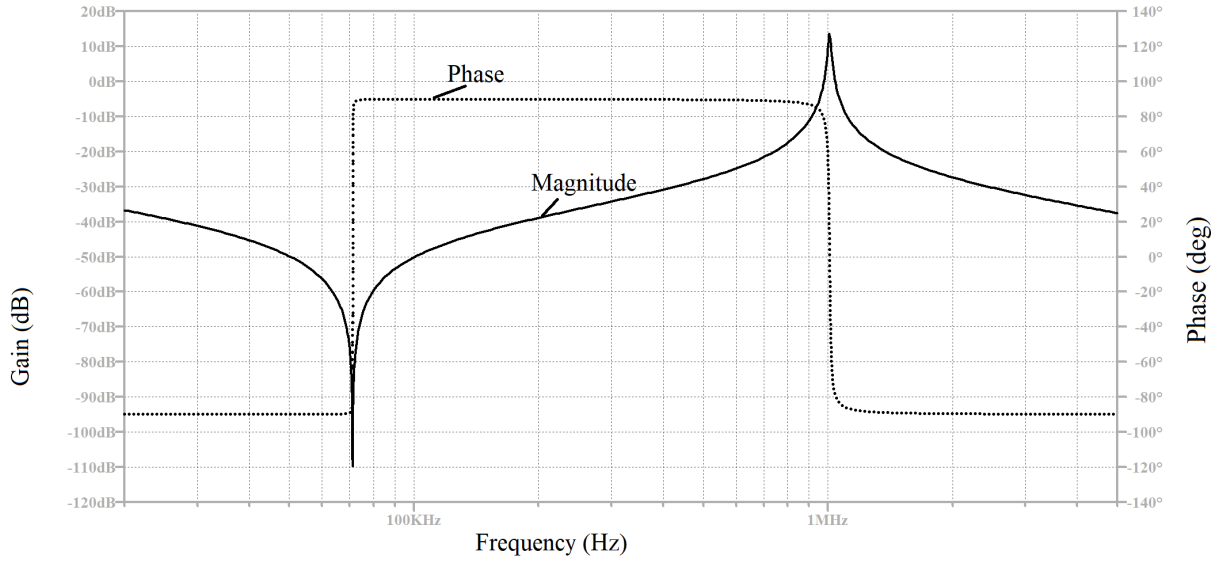

Fig. 4.2: Illustration of the frequency response of transfer function $H(s)$ above.

Fig. 4.2 above shows the frequency response associated with the transfer function $H(s)$ above for arbitrarily chosen values of $R_s = 5\ \text{k}\Omega$, $r_i = 2\ \text{m}\Omega$, $L_i = 10\ \mu\text{H}$, $C_i = 500\ \text{nF}$ and $C_T = 2.5\ \text{nF}$. The two resonances at 71.2 kHz (with $Q_i = 2236$) and 993.4 kHz (with $Q_0 = 78$) can clearly be observed from the illustration above and show that frequency components around 71.2 kHz are significantly filtered by the bandstop resonance response while frequency components around 993.4 kHz are selected by the bandpass resonance response. Thus, care must be taken during image current or voltage detection to avoid detecting around 71.2 kHz where the signal is relatively suppressed. For Ytterbium ion however, the values for are quite different from known common values with $L_i \approx 15.36$ MH and $C_i \approx 1.65 \times 10^{-9}$ pF for resonances $\omega_0 \approx \omega_i = 1$ MHz and a relatively large trap capacitance ($C_T \gg C_i$), i.e. $C_T \approx 29$ pF in our case. Fig. 4.3 below shows the response corresponding to these values of inductance and capacitances.

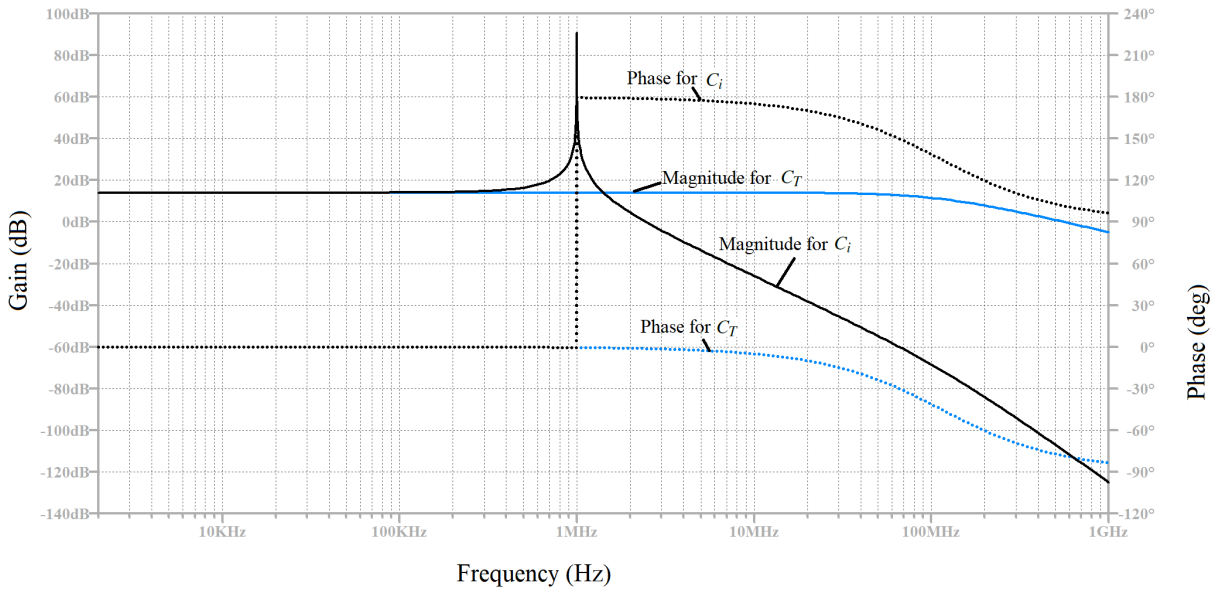

Fig. 4.3: Illustration of the frequency response of $H(s)$ with actual values based on trapped Ytterbium ion.

The black curve shows the response as measured across the capacitor C_i while the the blue curve shows

the response as measured across the electrode pairs (i.e. capacitor C_T). The resonance response seems to be suppressed across the trap electrodes and this may imply that the resonance effects are unlikely to be detected at 1 MHz.

4.1.1 Resonant Coupling

For this current or voltage signal, generated by the trapped ion, to be detected it first needs to be coupled out through some nearby electrodes. The coupling via nearby electrodes can be thought of as both capacitive and inductive. In the inductive case the ion needs to be accelerating or decelerating to create a time-varying flux which induces current in the nearby electrodes. The capacitive coupling case is primarily based on image charge, and hence image current, created by the trapped ion on the nearby electrodes. In this case the trapped ion is not required to be accelerating or decelerating. In both cases one can think of a transformer (inductive or capacitive) linking the current created by an oscillating trapped ion to the nearby conducting electrodes. The electrodes can then be part of a resonant circuit which feeds the scope or amplifiers before the scope. We can model this with the following electrical circuit,

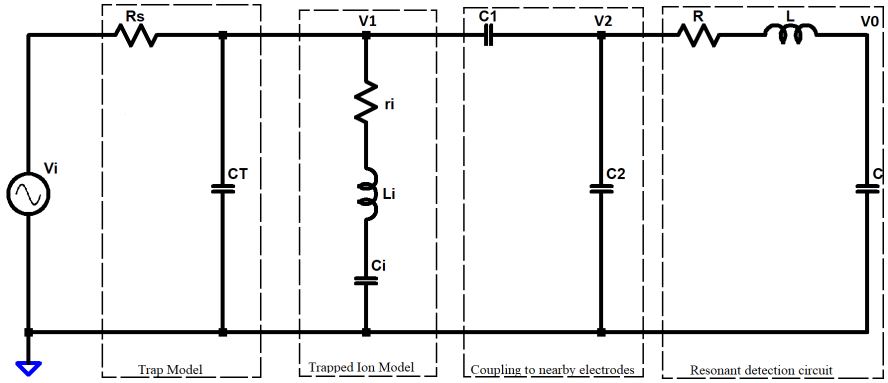

Fig. 4.4: Image current detection circuit model.

Fig. 4.4 above shows an image current detection circuit model with C_1 and C_2 modeling a coupling transformer between the ion model (left side of C_1 and C_2) and the probing electrodes connected to a resonant filtering circuit on the right hand side. Assuming that $C_2 \gg C_1$ the network of C_1 and C_2 mimics a buffering capacitive transformer ($1:k$ with $k = C_1(C_1+C_2)^{-1}$) with very high input impedance and small output impedance. This allows us to approximate the response of V_0 relative to V_i using the following third order transfer function model;

$$H(s) = \frac{V_o}{V_i} = \frac{k(s^2 + \frac{\omega_1}{Q_1}s + \omega_1^2)}{(s+p)(s^2 + \frac{\omega_2}{Q_2}s + \omega_2^2)(s^2 + \frac{\omega_3}{Q_3}s + \omega_3^2)} \tag{4.6}$$

with p as the only real pole. By choice, the resonance frequencies ω_2 and ω_3 can be chosen to be identical ($\omega_2 = \omega_3 = \omega_0$) in order to improve the overall selectivity (i.e. $Q_0 = Q_2 Q_3$). Fig. 4.5 below shows the response of V_0 relative to input drive voltage V_i for the case of $\omega_2 = \omega_3 = \omega_0$.

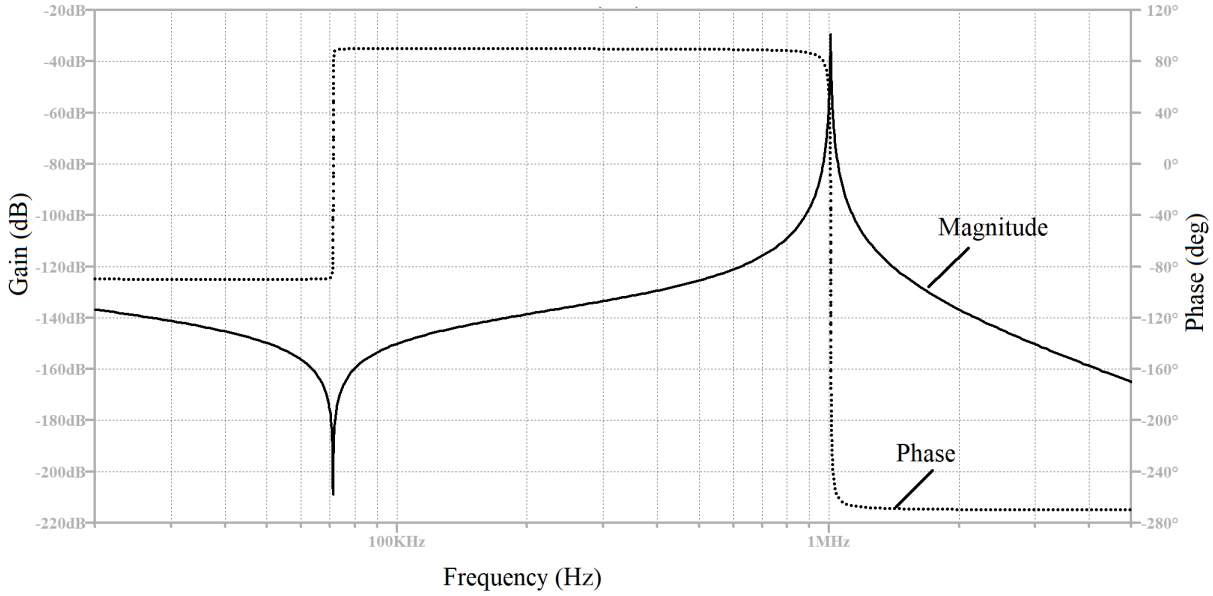

Fig. 4.5: Frequency response of resonant out-coupling voltage V_0 relative to input voltage V_i.

The component values used here are similar to those used in Fig. 4.2 and additionally $C_1 = 2$ pF, $C_2 = 200$ nF, $R = 200$ mΩ, $L = 25$ μH and $C = 1$ nF. It can be seen from Fig. 4.5 above that the response changed from that in Fig. 4.2, of V_{C_T} (or equivalently V_1 in Fig. 4.5) relative to the input voltage V_i, by just an overall scaling factor proportional to the logarithm of k as well as the selectivity around 1 MHz resonance. The increase in selectivity of resonance around 1 MHz is due to the contribution of the ion model resonance (as seen previously in Fig. 4.2) as well as the contribution of the resonant out-coupling RLC circuit resonating in sync at 1 MHz. The resulting selectivity becomes the product of the individual contributions. Using the realistic values for Ytterbium ($L_i \approx 15.36$ MH, $C_i \approx 1.65 \times 10^{-9}$ pF and $C_T \approx 29$ pF) the response measured at V_0 looks like the one in Fig. 4.6 below.

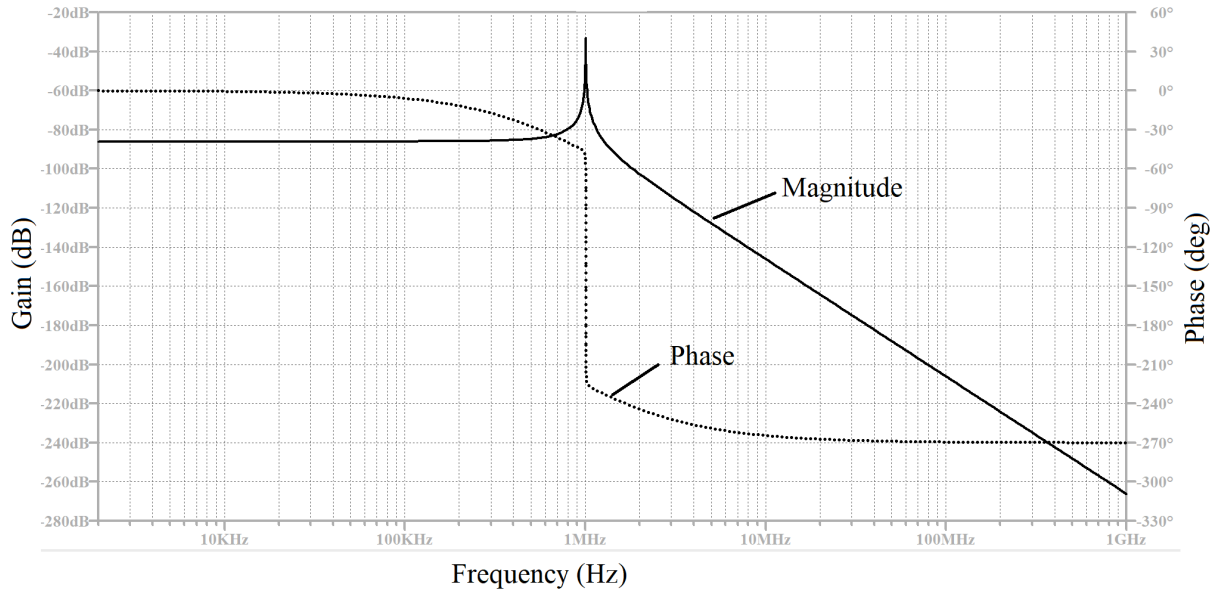

Fig. 4.6: Frequency response of resonant out-coupling voltage V_0 relative to input voltage V_i with inductance and capacitance values corresponding to Ytterbium ion.

The observed resonance response at 1 MHz is mainly due to the out-coupling resonant circuit.

4.1.2 Signal and Noise

In [60] the signal to noise ratio expression for the differential mode detection is given by;

$$SNR = \frac{\sqrt{\pi}}{2}\frac{r_{ion}}{d}Z\sqrt{\frac{\nu}{\triangle\nu}}\sqrt{\frac{Q}{k_BTC}} \tag{4.7}$$

where r_{ion} and Z are the ion's motional radius and its charge, d, T, C and Q are the effective electrode distance, temperature, capacity, and quality factor of detection system respectively. The ratio $\frac{\nu}{\triangle\nu}$ describes the ion's motional frequency relative to its width. It is clear also that the larger the amplitude of oscillation of the ion r_{ion}, the larger the signal to noise ratio. Increasing the amplitude of ion's oscillation amounts to increasing the pulse voltage used to drive the ion on resonance. Also cooling the detection circuit and trap will lower temperature T which in turn improves the signal to noise ratio. The induced image current can be as low as a few hundred femtoampere as the number of trapped ions approaches one. The dependence of the signal to noise ratio on temperature implies that better results can be obtained by cooling the detection electronics. The quality factor Q reported in this paper had a value of a few thousands. The image current was detected by the proportional voltage drop across the trap electrodes. The voltage was amplified and Fourier transformed to obtain the frequency spectrum. In [65] the differential detection method is employed and implemented using electrically isolated pins embedded inside the two endcaps. The detection pins/electrodes are isolated from the endcaps using Teflon insulation. The differential detection experiment proceeds sequentially according to the steps shown in Fig. 4.7 below.

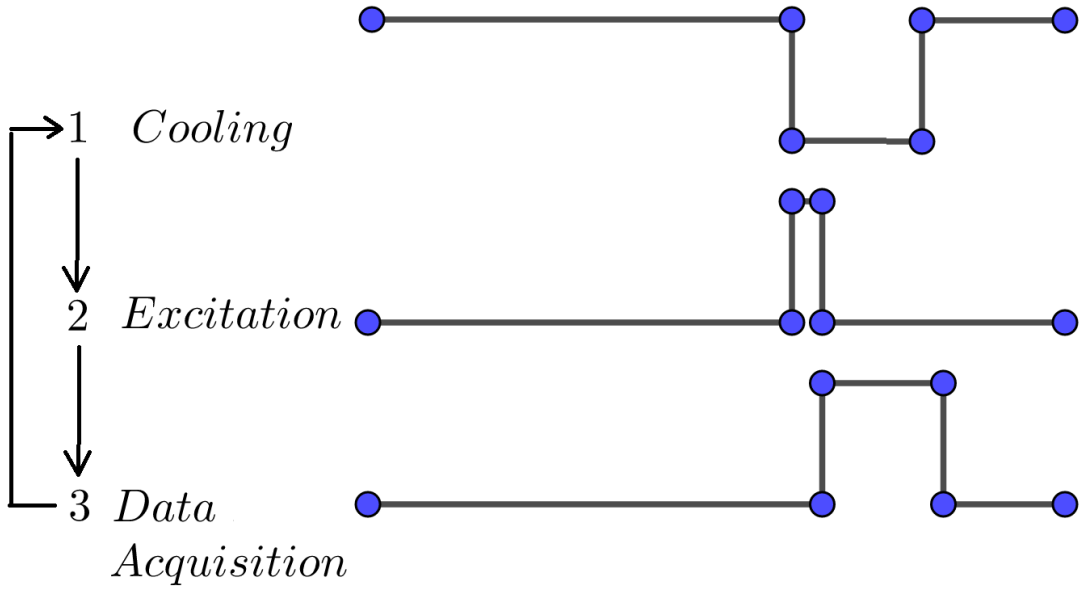

Fig. 4.7: Steps of detecting ion presence via image current measurement.

First the RF trapping potential is switched on and stays on for the duration of the experiment cycle. Ionization of neutral atoms follows after which cooling of ions commence for some time (20 ms to 2 s). After the cooling phase a dc excitation pulse is switched on to kick the ions and have them oscillating resonantly at their secular frequency. Data acquisition phase follows immediately after the excitation dc

pulse and in this phase the image current is detected on the pin detector electrodes, amplified, filtered and Fourier transformed to obtain an intensity vs frequency spectrum. The image currents from the end caps were each passed through a field-effect transistor (FET). Then the currents were fed into a low noise pre-amplifier (with gain in the range 1 to 50000) via differential inputs. The differential signal out of the pre-amplifier was band-pass filtered and then amplified further (gain of 100) before displayed on the oscilloscope in time and Fourier transform. The TTL pulses were used for synchronously triggering all necessary phases of this experiment. In the results of [65] it was reported that in the differential detection mode the systematic background noise was greatly reduced and almost negligible except for low frequency $1/f$ noise. Also the signal intensity of the atomic peaks were increased.

4.1.3 Transimpedance Amplification and Detection

One option of detecting the ion's image current from the probes is by using the transimpedance amplifier [67, 68]. This amplifier is useful in other buffering and current measurement applications such as in the amplification of photocurrent in optical receivers [69–71]. In [72] an ultra-low-noise ($4fA/\sqrt{Hz}$ at $\pm 200pA$ range) transimpedance amplifier is used to detect currents in the picoampere (pA) range with bandwidth greater than 10 kHz. The transimpedance amplifier basically converts current signal to voltage signal using a large resistance as a conversion gain. A typical circuit of a transimpedance amplifier is shown in Fig. 4.8 below.

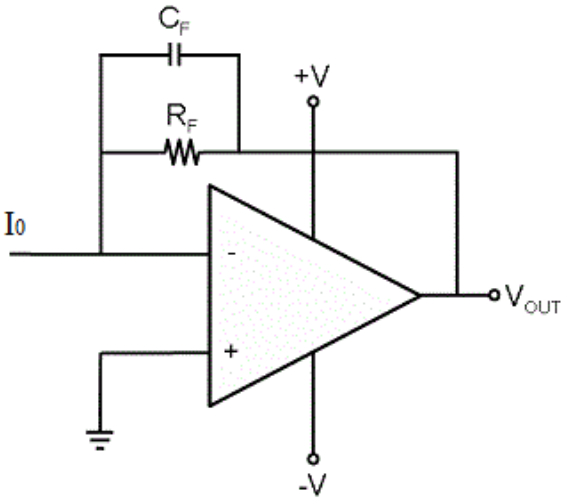

Fig. 4.8: Transimpendance amplifier circuit.

The design procedure starts with determining the range of input current as well as the desired output voltage range. Suppose we wish to convert input current in the range $[0\text{ nA},\ 5\text{ nA}]$ to output voltage in the range $[0\text{ mV},\ 5\text{ mV}]$. The required feedback resistance R_f will then be given by:

$$\begin{aligned} R_f &= \frac{V_{0Max}-V_{0Min}}{I_{iMax}-I_{iMin}} = \frac{5\text{ mV}-0\text{ mV}}{5\text{ nA}-0\text{ nA}} \\ &= 10^6\ \Omega = 1\ \text{M}\Omega \end{aligned} \tag{4.8}$$

The feedback capacitor C_f, for some given operating frequency ω_0, is selected such that the following circuit bandwidth condition holds:

$$C_f \leq (\omega_0 R_f)^{-1} \tag{4.9}$$

For instance, with $\omega_0 = 2\pi(1\text{ MHz})$ we get the upper bound for feedback capacitor as:

$$C_f \leq (\omega_0 R_f)^{-1} = (2\pi(1\text{ MHz})(1\text{ M}\Omega))^{-1} \approx 1.59\text{ pF} \tag{4.10}$$

For an op amp with the combined input capacitance of $C_i \approx 6$ pF its gain-bandwidth product (GBW) must satisfy the following condition:

$$GBW > \frac{C_i + C_f}{2\pi R_f C_f^2} \tag{4.11}$$

For $C_i \approx 6$ pF the gain-bandwidth product must be greater than 48 MHz. There are other variations in the design of transimpedance amplifiers and some of these different topological designs can be found in [69–71]. One advantage of the trasimpedance amplifier, with regard to signal to noise ratio, is that the output voltage signal varies linearly with the feedback resistor while the output noise signal varies linearly with the square root of the feedback resistor, hence large resistor values are preferable [73]. In our lab we used a transimpedance amplifier circuit shown in Fig. 4.9 below with a conversion gain on the order of $\sim 10^8\ \Omega$.

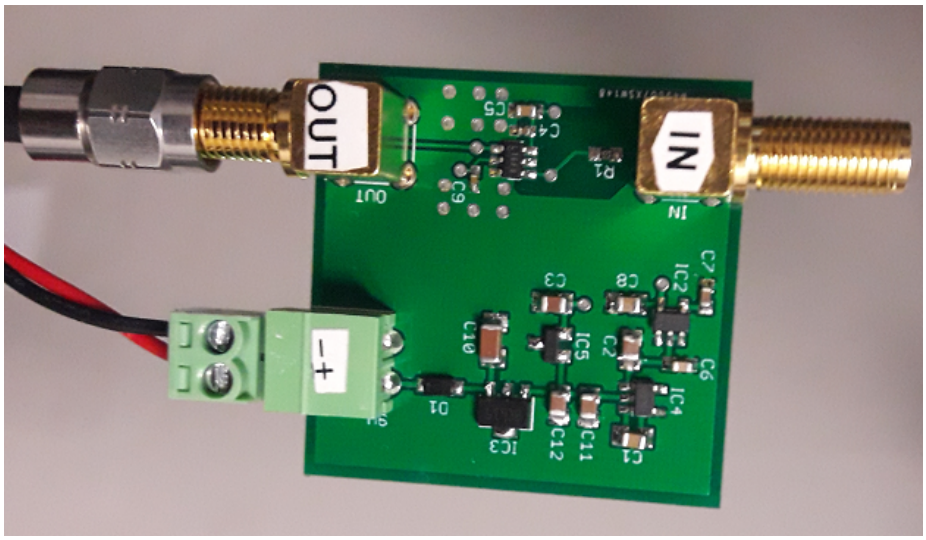

Fig. 4.9: Custom made transimpedance amplifier circuit.

In the previous section we looked at the resonant out-coupling of the voltage generated on the probe electrodes due to oscillating ions in the trap. In this section we consider current, rather than voltage, as our signal of interest to be coupled out of the trap. The image current on the probe electrodes due to an oscillating charge in the trap is a result of inductive and capacitive coupling. As the charge oscillates it

periodically perturbs the electric field and can be seen as small voltage source which then couples to the probe electrodes capacitively as shown in the circuit model in Fig. 4.10 below.

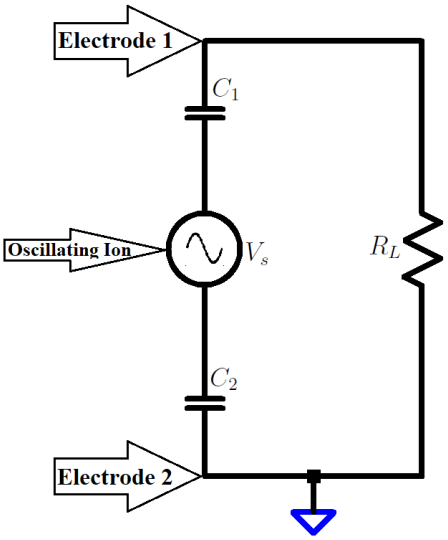

Fig. 4.10: Oscillating ions as a voltage small source.

The capacitors C_1 and C_2 form a coupling between ions and probe electrodes and V_s is the perturbative potential due to the ions oscillation. The load resistance R_L here is the input impedance of the detection circuit which will be explained later as the transimpedance amplifier. The circuit in Fig. 4.10 above can be reduced to its equivalent form shown in Fig. 4.11 below.

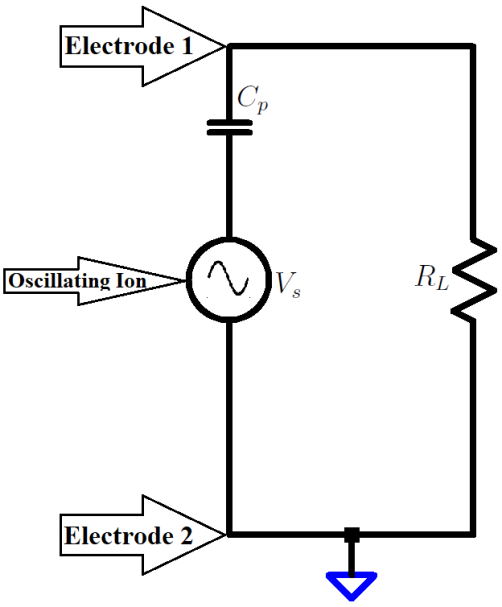

Fig. 4.11: This circuit is equivalent to the one in Fig. 4.10 with the capacitances C_1 and C_2 combined.

The combined capacitance $C_p = C_1C_2/(C_1 + C_2)$ is the capacitance of the probe electrodes. Applying Norton's theorem the on the circuit in Fig. 4.11 above we obtain the circuit with equivalent current source as shown in Fig. 4.12 below.

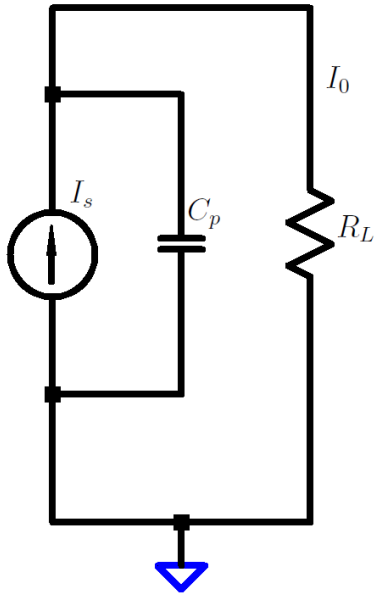

Fig. 4.12: Equivalent circuit model with a current source.

The current source I_s here is the image current given (in terms of V_s) by $I_s = sC_pV_s$ with $s = \sigma + j\omega$ as the Laplace parameter and $j\omega$ as the Fourier parameter in frequency domain. The parameter σ accounts for attenuation and damping in the signal. The frequency $\omega = 2\pi\nu$ is the oscillation frequency of the ion inside the trap and this means that the image current scales linearly with the oscillation frequency of the ion. It is also worth noting that the I_s is 90° out of phase with respect to V_s. This current can be amplified with a transimpedance amplifier with appropriate conversion gain R_L and the resulting transfer function relating I_0 and I_s is given by:

$$\frac{I_0(s)}{I_s(s)} = \frac{1}{sR_LC_p + 1} \tag{4.12}$$

The frequency response of this transfer function is shown in Fig. 4.13 below.

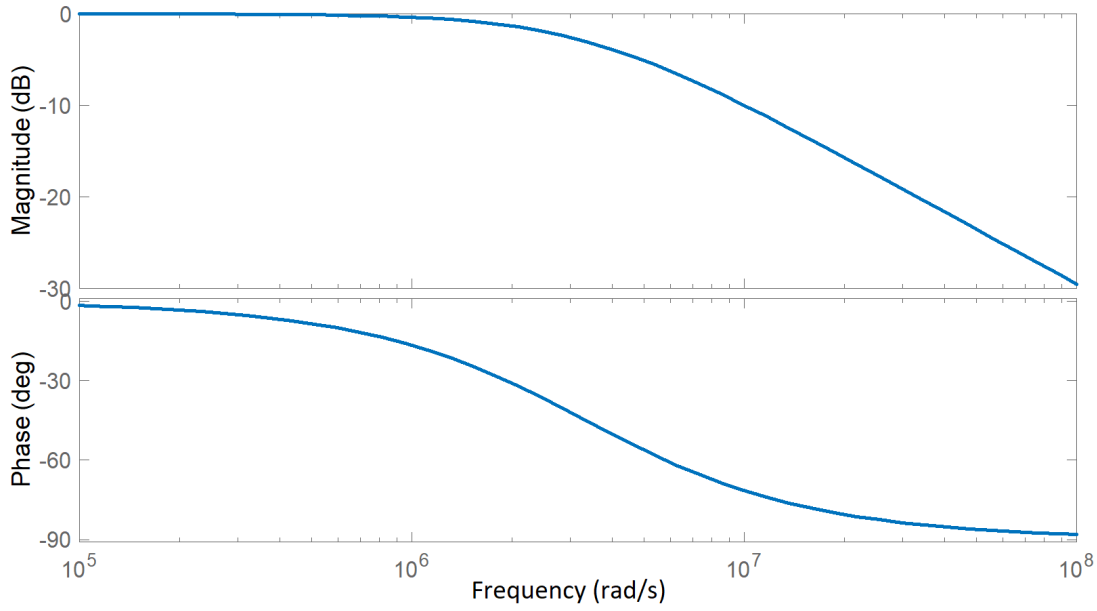

Fig. 4.13: Frequency response of the circuit in Fig. 4.12.

The simulation parameters are $R_L = 10$ kΩ and $C_p = 30$ pF. From the response in Fig. 4.13 there is a dc gain of unity and at high frequencies the gain drops below unit. Another option is to resonantly couple this image current into the load as shown in Fig. 4.14 below.

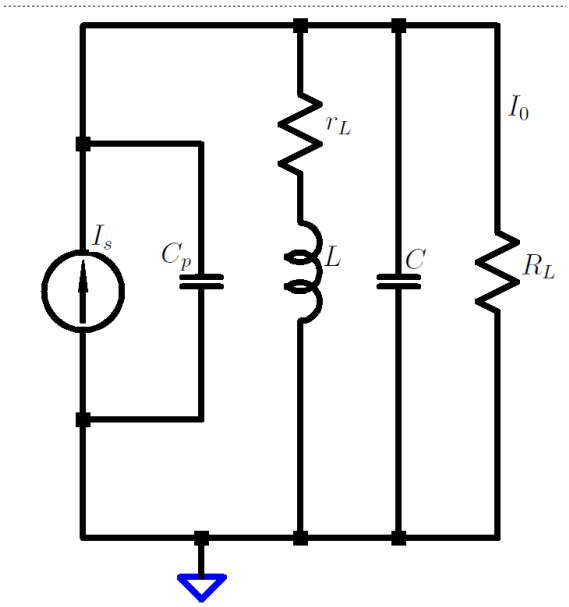

Fig. 4.14: Circuit that resonantly couple image current into the transimpedance amplifier.

The point here is to make the resonant circuit to have a resonance frequency that matches the desired oscillation frequency of the ion such that when the ion oscillates at that frequency it drives the circuit on resonance and take advantage of maximum gain provided by resonance at that frequency. The transfer function relating I_0 and I_s is given by:

$$\frac{I_0(s)}{I_s(s)} = \frac{s\frac{1}{R_L(C+C_p)} + \frac{r_L}{R_L L(C+C_p)}}{s^2 + s(\frac{r_L}{L} + \frac{1}{R_L(C+C_p)}) + \frac{r_L+R_L}{R_L L(C+C_p)}} \tag{4.13}$$

with resonance frequency $\omega_0 = \sqrt{\frac{r_L+R_L}{R_L L(C+C_p)}}$ and quality factor $Q = \frac{\sqrt{R_L L(C+C_p)(r_L+R_L)}}{r_L R_L(C+C_p)+L}$. The parasitic resistance r_L of the inductor puts a limit to on the quality factor of our resonance coupling. In the ideal case whereby $r_L = 0$ Ω the transfer function simplifies to,

$$\frac{I_0(s)}{I_s(s)} = \frac{s\frac{1}{R_L(C+C_p)}}{s^2 + s\frac{1}{R_L(C+C_p)} + \frac{1}{L(C+C_p)}} \tag{4.14}$$

with resonance frequency $\omega_0 = \frac{1}{\sqrt{L(C+C_p)}}$ and quality factor $Q = R_L\sqrt{\frac{C+C_p}{L}}$ hence large values of R_L leads to high quality factor. Fig. 4.15 below show the frequency response of the circuit with $r_L = 0$ Ω and $r_L = 3$ Ω to illustrate the effect of r_L as the limiting factor on quality factor. The simulation parameters are $R_L = 10$ kΩ, $C_p = 30$ pF, $C = 100$ nF and $L = 25.3$ μH.

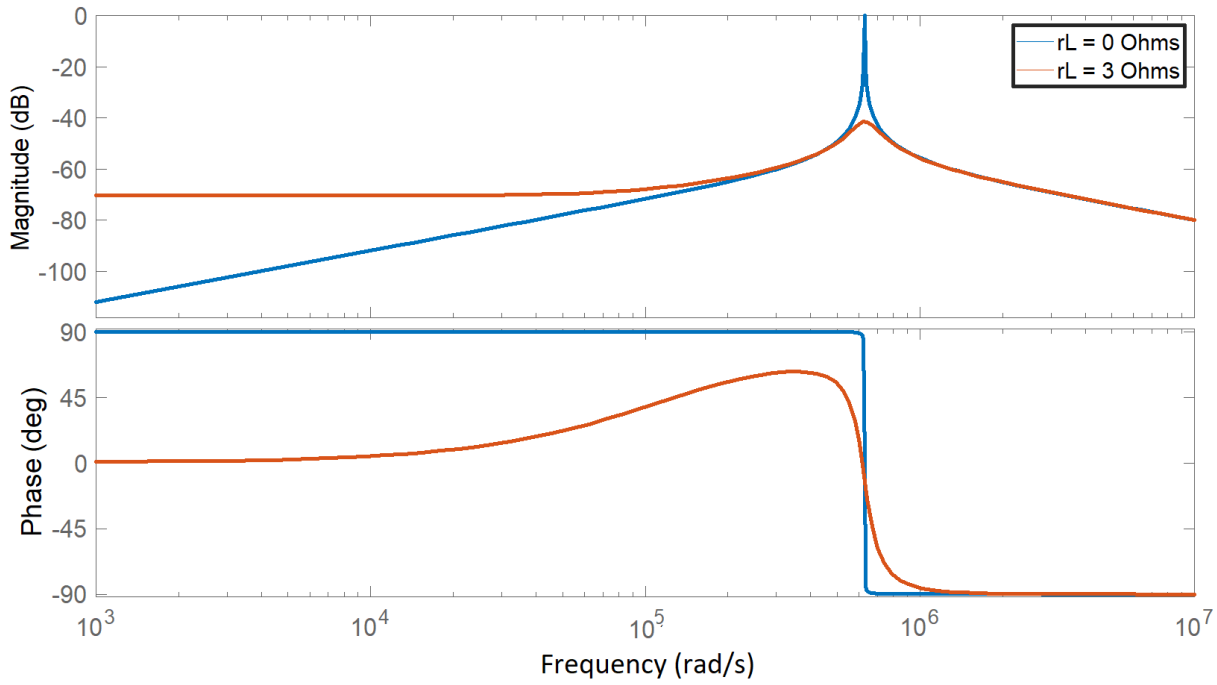

Fig. 4.15: Frequency response of the circuit in Fig. 4.14 for different values of r_L.

It can be seen that even with the ideal case of $r_L = 0\ \Omega$ the gain does not exceed unity thus, this approach does not give any advantage over the first approach shown in Fig. 4.13 with regard to gain. This resonant coupling approach is however, could be preferred for filtering noise in cases where gain is not a primary concern. The output current I_0 from these coupling circuits is fed into a transimpedance amplifier, with a conversion gain of R_f, to give an output voltage $V_0 = R_f I_0$ which can then be displayed on the scope.

4.2 Ion Tickling Experiment

In this experiment we propose to use the differential detection mode to detect the presence of coherently oscillating trapped ion cloud. The ion oscillation is triggered by tickling across the chosen electrodes with either a static voltage pulse or an rf voltage close to the secular frequency of trapped ions. We can adopt the sequential protocol outlined in [65] for carrying out this differential detection experiment. We begin by loading neutral Ytterbium atoms into the trap where they get photoionized by the 398 nm and 369 nm lasers beams. Once ionized, confinement by rf drive voltages takes place and cooling laser beams, switched on by the FPGA program, cool the ions. After a few milliseconds laser cooling is switched off and ion motion excitation by static pulse or rf tickling is switched on immediately for a few microseconds after which the detection step starts and takes a few milliseconds. After detection the process repeats again starting at the cooling step onward.

Our detection of image current could take place on endcaps pair, compensation electrodes pair and rf electrodes pair while taking care to filter out rf drive frequency components. Detecting on these various electrode pairs helps to enhance the detected signal by combining different angles of detection. Unlike with the setup in [65] our detection electrode at the endcaps and compensation electrodes are not electrically isolated from the applied static potential at the endcap and compensation electrodes. A

static voltage pulse or rf tickling voltage is applied to the trap rf electrodes through a resonator input bias port or directly on the endcap or compensation electrode by sending the voltage backwards through the LC filters shown in Fig. 4.16 which isolate static voltage from the detection endpoint and tickling sources. The trapped ions respond to tickling by oscillating which in turn induces some current onto the trap electrodes. This image current on the trap electrodes is very small (on the order of a few hundred femtoamperes for a single ion [65]) and probably dominated by noise thus, presenting a challenge when observing this current as mentioned in the previous sections.

4.2.1 Resonant Coupling

Since the use of amplifiers to enhance the detected image current tends to introduce more excess noise, we built four resonant LC filters as shown in Fig. 4.16 below, in an attempt to enhance detected image current signal and filter out noise.

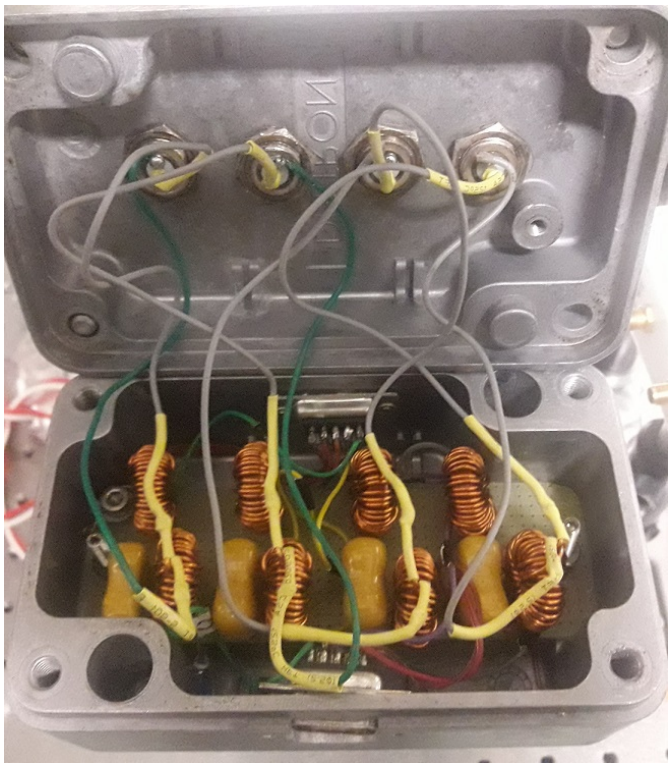

Fig. 4.16: Four LC filter circuits for resonantly coupling out the detected image current from two endcaps and two compensation electrodes.

This circuit is basically four LC resonators (similar to the output stage in Fig. 4.4) each with a transformer at the output. Each detector electrode is connected to resonator with resonance frequency near secular frequency of trapped ions. The output of the resonators could be connected to a differential input of the pre-amplifier which then feeds its differential output signal to the Lockin amplifier. The resonance frequency for our filters is tuned close to the trap frequency, which is approximately 1 MHz. The reason being that we will be tickling at this frequency to excite the motional states of the ions. Fig. 4.17 to Fig. 4.20 below show the frequency response of each of the four simple resonant filters we built.

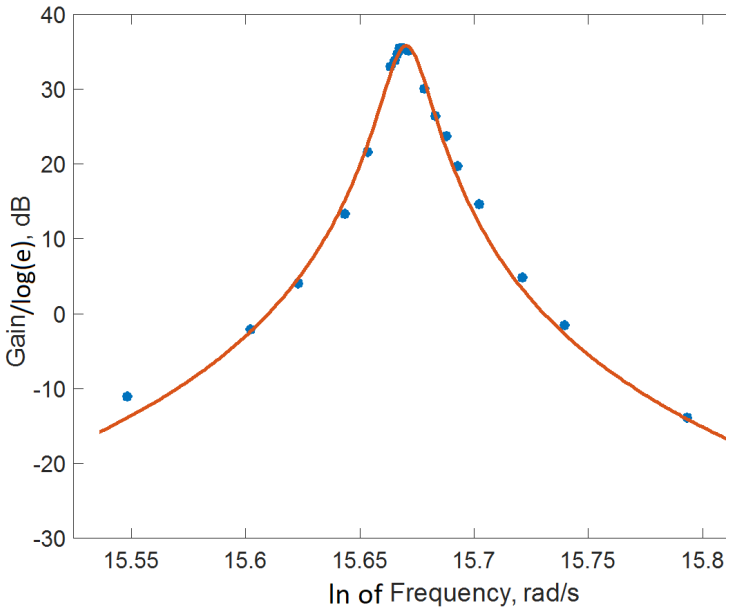

Fig. 4.17: Turbo side End Cap.

Fig. 4.17 shows the frequency response of the resonant filter which couples out the image current from end cap on the turbo side of our setup. This filters has a voltage gain (due to out-coupling step up transformer) that measures 6.0, a quality factor that measuring 49 at the resonance frequency of 1.017 MHz.

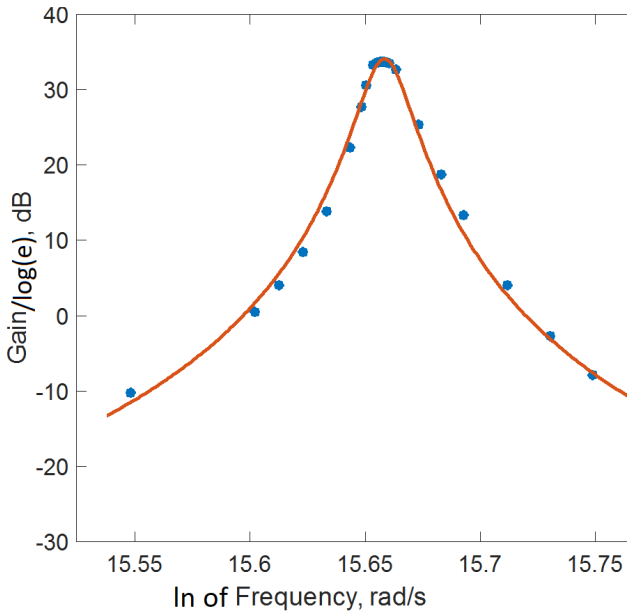

Fig. 4.18: Gauge side End cap.

The measured quality factor is quite small for this application of ion detection, however, we continue with this setup for detection of ion cloud. Fig. 4.18 shows the frequency response of the resonant filter which couples out the image current from end cap on the gauge side of our setup. This filters has a voltage gain (due to out-coupling step up transformer) that measures 5.5, a quality factor that measuring 44 at the resonance frequency of 1.005 MHz. Detecting ions on both endcaps can prove advantageous since the two detected signals will be out of phase with respect to each other and taking their differential can eliminate more uniform noise and enhance the detected differential signal against noise.

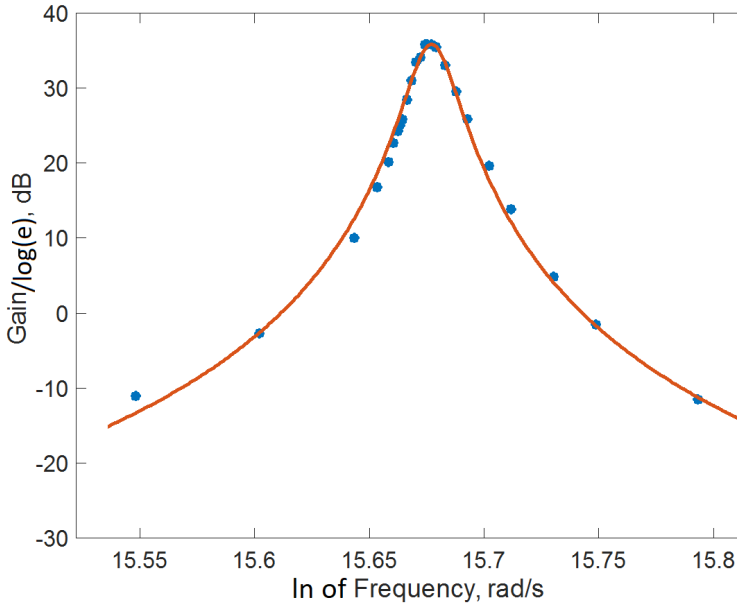

Fig. 4.19: High Comp.

Fig. 4.19 shows the frequency response of the resonant filter which couples out the image current from the high compensation electrode. This filter has a voltage gain (due to out-coupling step up transformer) that measures 6.0, a quality factor that measuring 45 at the resonance frequency of 1.024 MHz. Compensation electrodes are close to the ions than the endcaps and this gives them a better chance of detecting image current.

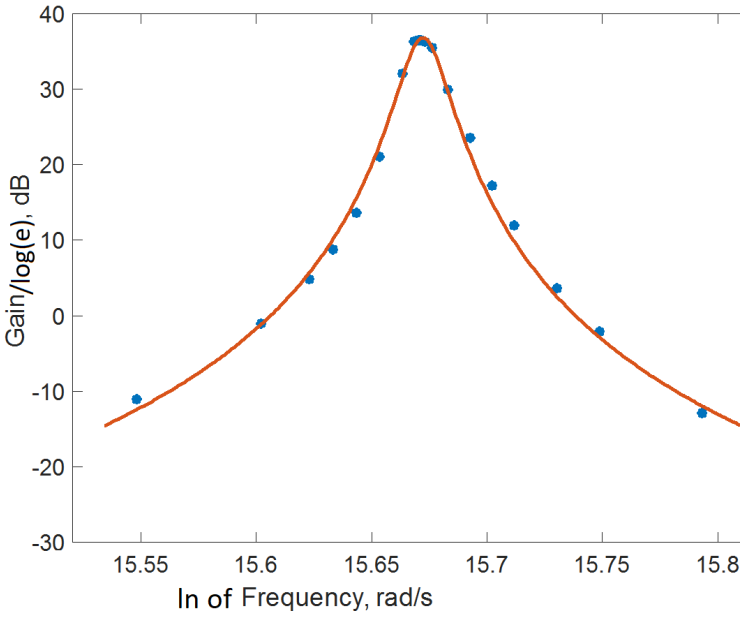

Fig. 4.20: Low Comp.

The closer the probe electrode is to the ions the better the detection of image current signal induced by the oscillating ions. Fig. 4.20 shows the frequency response of the resonant filter which couples out the image current from the low compensation electrode on the side of the ion trap. This filter has a voltage gain (due to out-coupling step up transformer) that measures 6.3, a quality factor that measuring 47 at the resonance frequency of 1.019 MHz. The high and low compensation electrodes are

almost symmetrically located about the trap axis and just as with the two end caps, detection from these two compensation electrodes can prove to be advantageous by minimizing excess homogeneous noise through taking a differential signal from the two compensation electrodes.

The quality factors measured above are pretty small compared to those reported in the literature, for example in [60] the reported quality factor is on the order of ~ 1000. Also our detection electrodes are quite far from the oscillating ions and these factors can lead to weak detection of image current. As part of future work, we suggest improving the quality factor by looking closely as impedance matching techniques and implement detection probes that are closer to the oscillating ions to enhance the detected image current signal. In the next subsection we outline the amplification procedure that could be adopted as part of future work, once the quality factor and detection probes have been improved.

4.2.2 Pre-Amplification and Lock-in Amplifier Setup

A Lock-in amplifier is a very useful device when dealing with detection of very small oscillating signals. It can retrieve signal as small as a few nanovolts buried in noise orders of magnitude larger by using a phase-sensitive detection which make use of the reference frequency and phase source to pick out a signal with a matching phase and frequency.

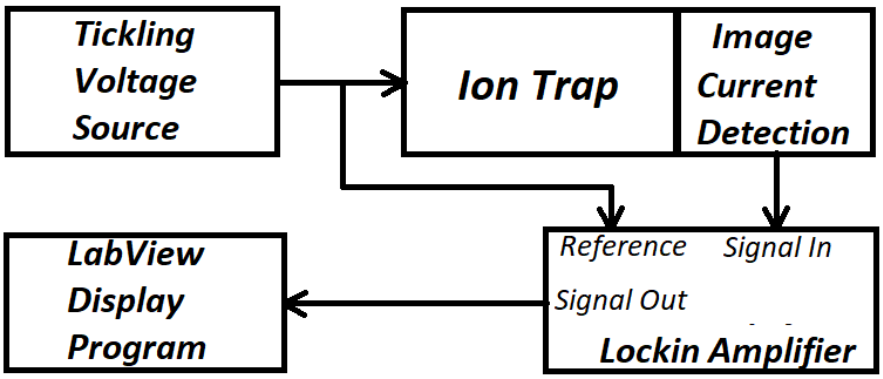

Fig. 4.21: Schematic of Lock-in amplifier setup.

This device is just what we need for our small signal detection problem. In our setup the outputs of the resonant filters are connected to the pre-amplifier to generate an enhanced differential voltage signal which is then fed into the Lockin amplifier input port along with the ticking input source as the reference to the Lock-in amplifier, as shown in Fig. 4.21, for further enhancement and visualization. With everything connected properly the experiment proceeds as follows.

We turn on a tickle source and switch it off for an appropriate time and observe on the Lock-in amplifier display for any change in the profile due to residual ion oscillation. To avoid switching off the reference for the Lock-in amplifier, the tickling source is only switched off for the channel going to the trap electrodes while it remain on for the channel going to the Lock-in amplifier. We use one RF switch to do this selective on/off switching. The observation period should be long enough to observe the ion residual oscillation profile as it dies off after which we repeat the tickling and observation again and again.

4.3 Integrating New Detection Probes

Detecting image current on the endcaps and compensation electrodes was thought to be inefficient since they are relatively far from the oscillating ions in comparison to rf electrodes. We, therefore, integrated two detection probe electrodes positioned next to two diagonal rf electrodes as shown in the schematic diagram in Fig. 4.22 below.. In this configuration the detection probes are as close, to the ions, as the rf electrodes and this could enhance the detection of image current.

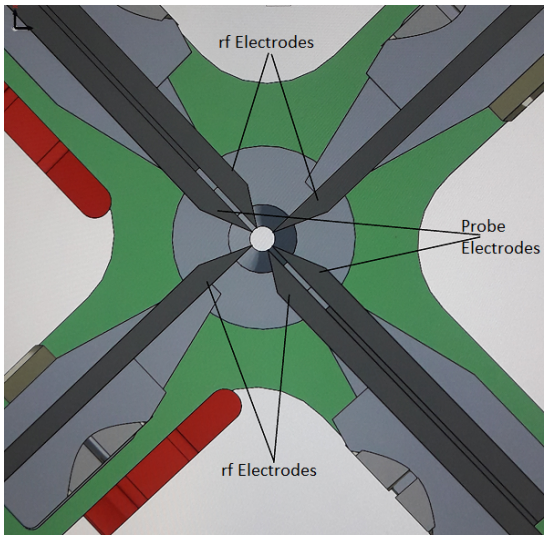

Fig. 4.22: Geometry of our trap with new probes integrated for image current detection.

The separation between diagonal rf electrodes is now $2r_0 = 1$ mm. It is also worth mentioning that holes were drilled through the endcaps to allow the isotope selection laser beam to pass through all the way to the other side. The new endcap to endcap separation after drilling the holes is $l = 13.41$ mm. The capacitance of the new probes was measured using the same technique used in chapter 2 as shown by the least squares fit in Fig. 4.23 below.

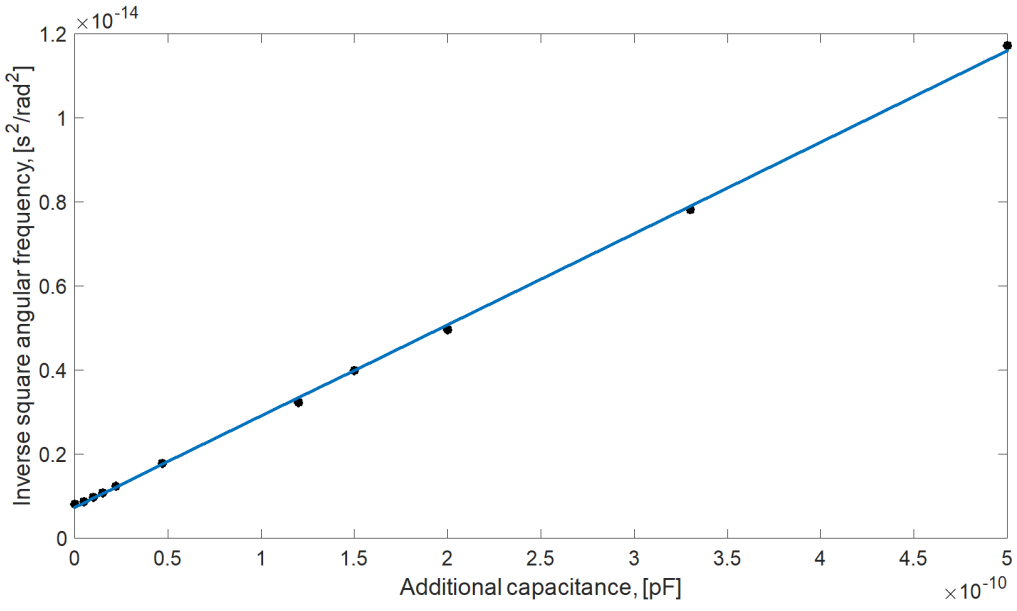

Fig. 4.23: Determining capacitance across two probe electrodes.

A 22 μH inductor was chosen for this experiment. From the plot in Fig. 4.23 the measured inductance is $L = 21.72$ μH and the measured probe capacitance is $C_p = 33.77$ pF. The trap capacitance was also measured after this integration of new probes and Fig. 4.24 below shows the least squares fit for its measurement.

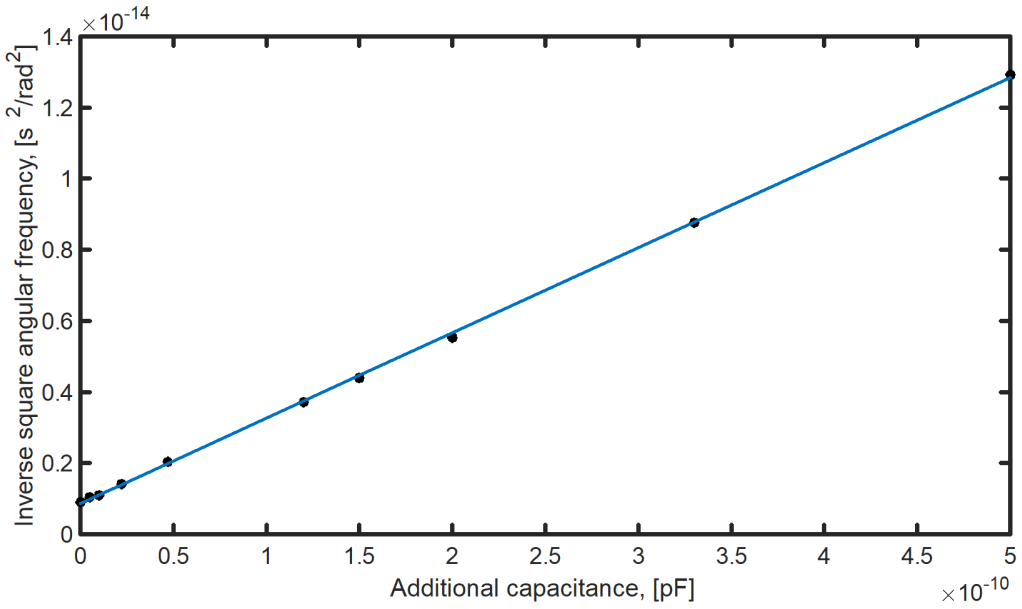

Fig. 4.24: Determining capacitance across trap electrodes.

Similar to the previous experiment, a 22 μH inductor was chosen for this experiment. From the plot in Fig. 4.24 the measured inductance is $L = 23.96$ μH and the measured trap capacitance is $C_T = 36.16$ pF. The probe electrodes can be connected to the transimpedance amplifier in differential mode and observe the output on the oscilloscope or spectrum analyzer. It is preferable, for stability reasons, to keep the input capacitance to the transimpedance amplifier small.

4.4 Testing Transimpedance Amplifier

We connected the probe electrodes to the input port of our transimpedance amplifier and connected the output of the transimpedance amplifier to the oscilloscope and spectrum analyzer. Next, we applied a small rf voltage (100 kHz) on the trap electrodes and swept the voltage up from 20 mVpp to 50 mVpp before detecting a peak (-50 dBm at 100 kHz) at on the spectrum analyzer. With the transimpedance amplifier gain of 10^8 Ω we inferred that the image current on the amplifier input is about 20 pA. From [60], the image current due to a single oscillating ion is on the order of a few hundreds of femtoamperes ($\sim$ 100 fA) and this is a factor of 200 below what we can detect on the spectrum analyzer. This suggests we either get many ions to oscillate coherently in the trap to enhance the image current or we improve the gain of our amplifier and we recommend this suggestion as part of future work. The other limiting factor is the background noise level of the spectrum analyzer which was roughly -55 dBm. If this background level was much less, the peak would be identified at a lower power thus, increasing the sensitivity of our measuring setup. In another different attempt the background noise level was -13.6 dBm and the

peak was distinguished at -13.3 dBm. This further shows the limitation in sensitivity brought by the background noise level.

4.5 Summary

In this chapter we stated the limitation of Ytterbium 174 ion in disposing off a closed fluorescence cycle which gives a large enough number of scattered photons. Based on this limitation we stated some alternative ion detection schemes including destructive and nondestructive ones. We then proposed the use of image current detection method as one of the attractive nondestructive method which preserves our qubit for future observations. We presented the electric circuit model for the trapped ion driven by a periodic potential as well as the detection circuit as a resonant filter. We outlined the procedure for testing the detection scheme using an external tickling source on the ion and observing its effects on the trapped ion cloud.

We integrated the new detection probes positioned much closer to the oscillating ion than the previously used detection electrodes. After this modification we measured the new trap capacitance as well as the capacitance across our new detection probe electrodes. Using these probes we tested a custom-made transimpedance amplifier with a dummy signal and found out that we are only sensitive to image current signals that are about 200 times the reported image current in the literature for a single oscillating ion. The content of this chapter serves mostly as the skeleton for future work on monitoring trapped 174 Ytterbium ions using image current detection technique.

Chapter 5

Power Law Noise Models and Bayesian Filtering

In Chapter 3 we mentioned that our lasers were not locked but the wavelengths were constantly being monitored on the wavelength meter during the Rabi oscillation experiment. In further experiments we plan to lock our lasers to optical cavities. Resonators such as optical cavities are usually affected by some combination of power law noise types and these noise types limit the stability of the optical cavity. It is, therefore, necessary to study these power law noises so as to be able to characterize the noise content associated with our optical cavities and perhaps devise some filtering techniques to suppress some noise components. This chapter is dedicated to the study of power law noise modeling from which estimation and filtering can be based. The chapter serves as an initial step towards handling power law noise which affects optical cavities upon which our lasers will be locked in future. More accurate measurements and interesting experiments can only be sensibly possible when the lasers are locked.

The knowledge of the type of noise affecting a dynamic system and a measurement is vital in smoothing, estimation and prediction applications. In Bayesian filtering whereby Gaussian noise associated with a linear time-invariant (LTI) system, Kalman filtering [74] offers an optimal state estimate and more attractive, the Bayesian filtering problem can be solved in closed form. On the other hand if the noise is non Gaussian and/or the associated system dynamics have nonlinearities, it often becomes a challenge to solve the Bayesian filtering problem in closed form and the resulting filter is often sub-optimal. Extended and unscended Kalman filters [75, 76] are two common derivatives of Kalman filter which deal with nonlinearities in the system dynamics through first order Taylor expansion and statistical linearization respectively. The probability distributions however, are assumed to be approximately Gaussian. In the case of high nonlinearities in system dynamics and nonGaussian distribution these approximate filters do not perform so well and it is common to resort to Sequential Monte Carlo (SMC) approaches such as particle filter [77,78]. The particle filter can handle both the nonlinearities and nonGaussian distributions well however, it offers no analytical closed form solution to the Bayesian filtering problem.

Gaussian mixture models (GMMs) are an alternative approach for approximating nonGaussian distributions. The GMMs give the hope of solving a Bayesian filtering problem with nonGaussian distributions

in a closed form. However, the main challenges with using GMMs for Bayesian filtering are (1) determination of the model size that sufficiently approximates the underlying distribution and (2) the management of a growing number of Gaussian terms on each iteration of the Bayesian update. There are various ways, in the literature, for addressing these challenges such as approaches based on SMC and expectation maximization (EM) algorithm for model size reduction [79]. In this work we adopt the Kullback-Leibler GMM reduction method presented in [79] and [80] for addressing the second challenge. To address the first challenge we restrict our study to a class of noises called power law noise and propose the use of well-known LTI models, Barnes-Jarvis and Mandelbrot models [81–83], for generating these noises as the basis for choosing the model size for GMMs. These power law noise models essentially attempt to generate the power law noise based on a careful aggregation of Gaussian noise components and this allows us to transform the problem of GMM model size into a power law noise model size problem. We can then compare the power spectral density (PSD) of the generated power law noise to the expected one and adjust the model size to achieve acceptable accuracy.

Power law noises are pretty common in various application some of which include electronics and oscillators or resonators. For example in optical atomic clocks the coherence time of the an optical transition is usually longer than that of a driving laser thus, the dominant instabilities are associated with the frequency noise (often power law noise type) in the drive laser which broadens its line-width [84]. In general the instability of most frequency sources can be modeled by a combination of power-law noise having a power spectral density of the form $S_y(f) \propto f^{\lambda}$ where f is the frequency in Hz. Table 5.1 below shows some of these power-law noise types [85].

Table 5.1: Power law noise types.

Noise Type	Exponent λ	PSD $S_y(f)$
White PM	2	-
Flicker PM	1	$h_1 sinc^2(\pi f \tau)$
White FM	0	$h_0 f^{-0}$
flicker	-1	$h_{-1} f^{-1}$
Random walk FM	-2	$h_{-2} f^{-2}$
Flicker walk	-3	$h_{-3} f^{-3}$
Random run	-4	$h_{-4} f^{-4}$

Various combinations of these noise types manifest in oscillators and resonators like optical cavities. In the next section we present the model for a general power law noise and show the transformation from Barnes-Jarvis model to Mandelbrot model using partial fractions. In Section III we outline the Bayesian filtering algorithm using Kullback-Leibler Gaussian mixture model reduction algorithm and the power law noise models outlined in Section II. In section IV we discuss a simulation example of a first order system with flicker noise. Section V concludes this chapter with some remarks and possible future work.

5.1 Power Law Noise Models

5.1.1 Overview

We adopt the frequency domain approach presented in [81] for constructing power law noise generation model. Consider a transfer function $G(s)$ made up of cascade of first order filters as shown below:

$$G(s) = \prod_{i=0}^{m-1} G_i(s) = \prod_{i=0}^{m-1} \frac{\tau s + \beta^i}{\alpha\tau s + \beta^i} \tag{5.1}$$

where s is the Laplace parameter, $\frac{\beta^i}{\tau}$ is the i^{th}- stage zero and $\frac{\beta^i}{\alpha\tau}$ is the i^{th}- stage pole with $\beta > 1$. For each stage it is obvious that the low frequency (DC) gain is unity ($\lim_{s\to 0} G_i(s) = 1$) while the high frequency gain is α^{-1}, ($\lim_{s\to\infty} G_i(s) = \alpha^{-1}$). That means a single stage changes the magnitude of the transfer function by a factor α^{-1}. It is clear then that for an m-stage cascade the magnitude of $G(s)$ changes by a factor α^{-m} in the frequency range $[\frac{\beta^0}{2\pi\tau}, \frac{\beta^m}{2\pi\tau}]$.

The power spectral density $S_y(s)$ of a power law noise has the following general form:

$$S_y(s) = A^2|s|^\lambda \tag{5.2}$$

where A is a constant, $\lambda \in [-2,4]$, i.e. for flicker noise $\lambda = -1$. To mimic this power spectral density the following condition must hold [81]:

$$\beta = \alpha^{-\frac{2}{\lambda}} \tag{5.3}$$

The condition is a direct consequence of the quadratic relationship the power spectral density and the transfer function of a linear time-invariant system and its derivation is shown next. Relating (by means of a ratio) the power spectral density at frequency β^0/τ and the one at frequency β^m/τ using equation (5.2) above we get,

$$\left|\frac{S_y(\frac{j\beta^m}{\tau})}{S_y(\frac{j\beta^0}{\tau})}\right| = \left|\frac{\beta^m}{\beta^0}\right|^\lambda = \beta^{m\lambda} \tag{5.4}$$

Now invoking the quadratic relationship between the power spectral density $S_y(s)$ and the transfer function $G(s)$ we get the following,

$$\left|\frac{S_y(\frac{j\beta^m}{\tau})}{S_y(\frac{j\beta^0}{\tau})}\right| = \left|\frac{G(\frac{j\beta^m}{\tau})}{G(\frac{j\beta^0}{\tau})}\right|^2 \tag{5.5}$$

Using equation (5.1) we find that,

$$\left|\frac{G(\frac{j\beta^m}{\tau})}{G(\frac{j\beta^0}{\tau})}\right|^2 = \alpha^{-2m} \tag{5.6}$$

Given the previous three equations we can conclude, therefore, that,

$$\beta^{m\lambda} = \alpha^{-2m} \tag{5.7}$$

which easily reduces to equation (5.3). It should be noted that while β^m controls the range of frequencies over which the model approximation is valid, τ controls where this range or band of frequencies begins and ends. Next we consider two state space models derived from this general cascade transfer function model. For simulation purposes we need to pick a value, or a few, for λ and here we choose $\lambda = -1$ from now onward, without loss of generality.

5.1.2 Barnes-Jarvis State Space Model

In this section we consider a cascade model from the previous section and show its Bode diagram and power spectral density, which falls approximately as $1/f$ over a frequency interval dictated by the choice of τ and β^m. The transfer function $G(s)$ for this cascade model is shown below:

$$G(s) = \prod_{i=0}^{m-1} \frac{\tau s + \beta^i}{\alpha\tau s + \beta^i} \tag{5.8}$$

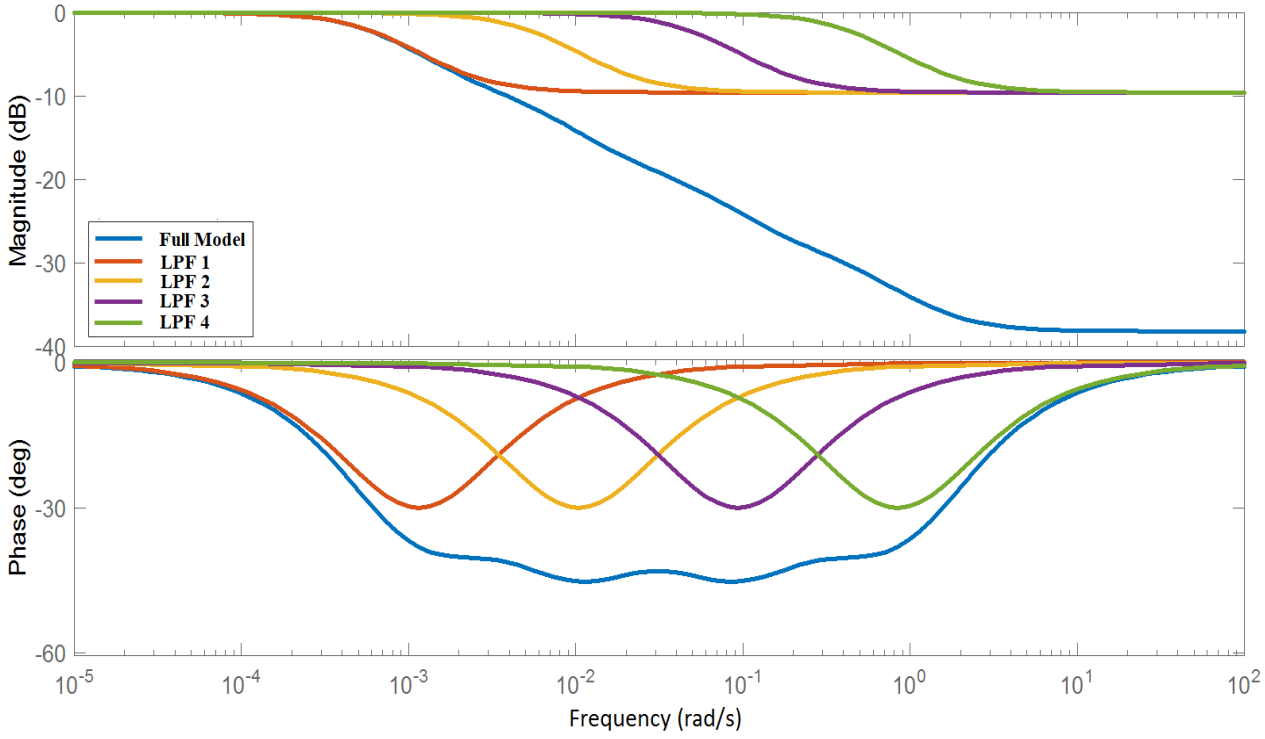

Fig. 5.1: Bode diagram for Barnes-Jarvis cascade model

Fig. 5.1 above shows the Bode plot of this transfer function together with its constituent cascade stages for settings $m = 4$, $\lambda = -1$, $\tau = 500$ s, $\alpha = 3$ and $\beta = 9$. The Bode diagram paints a picture of how individual frequency-shifted low pass filter stages contribute to the overall appearance of a $1/f$ fall-off. Fig. 5.2 below shows the log-log plot of the above model superimposed on the exact/expected flicker noise spectral plot slope.

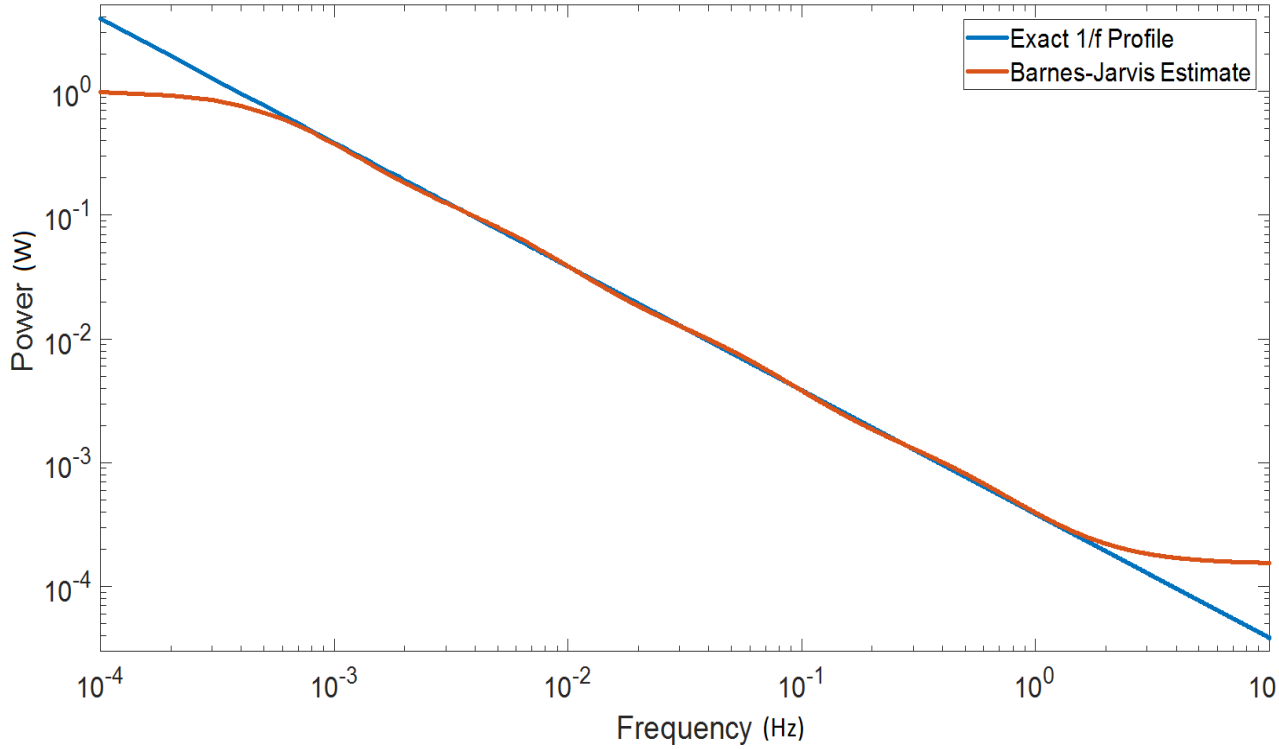

Fig. 5.2: Barnes-Jarvis model power spectral density fit.

Given the desired approximation accuracy, the parameters τ and β^m can be adjusted until the acceptable approximation error is obtained to within the desired range of frequencies by making reference to the power spectral density plot in Fig. 5.2 above. One way to convert the above transfer function to state space is by converting each cascade stage into state space and augment the resulting state space models by noting that the output of one stage becomes the input to the next stage. The cascaded transfer function model in Eq. (5.8) can be converted from frequency domain to time domain by considering this idea that the output of one stage becomes an input to the next stage. This means we only convert the individual stages and connect the results together. The individual i^{th} stage, relating the input $R_i(s)$ and $Y_i(s)$, is converted as follows into the corresponding differential equation:

$$\frac{Y_i(s)}{R_i(s)} = \frac{\tau s + \beta^i}{\alpha\tau s + \beta^i}\frac{Z_i(s)}{Z_i(s)} \tag{5.9}$$

where $Z_i(s)$ represents the i^{th} internal state of the model. Separating the numerators and denominators into separate equations and distributing the internal state throughout we get the following:

$$R_i(s) = \alpha\tau s Z_i(s) + \beta^i Z_i(s) \tag{5.10}$$
$$Y_i(s) = \tau s Z_i(s) + \beta^i Z_i(s) \tag{5.11}$$

Taking the Laplace inverse we get the following state space model for the i^{th} cascade stage:

$$r_i(t) = \alpha\tau \dot{z}_i(t) + \beta^i z_i(t) \tag{5.12}$$
$$y_i(t) = \tau \dot{z}_i(t) + \beta^i z_i(t) \tag{5.13}$$

Rearranging terms and making substitutions we get:

$$\dot{z}_i(t) = \frac{-\beta^i}{\alpha\tau} z_i(t) + \frac{1}{\alpha\tau} r_i(t) \tag{5.14}$$
$$y_i(t) = \frac{(\alpha-1)\beta^i}{\alpha} z_i(t) + \frac{1}{\alpha} r_i(t) \tag{5.15}$$

Now connecting cascade stages means $r_i(t) = y_{i-1}(t)$ and $r_{i+1}(t) = y_i(t)$. From now on we drop off the arguments for convenience. This connection procedure leads to the following coupled differential equations for a model of size m:

$$\dot{z}_0 = -\frac{1}{\alpha\tau} z_0 + \frac{1}{\alpha\tau} r_0 \tag{5.16}$$
$$\dot{z}_1 = \frac{(\alpha-1)}{\alpha^2\tau} z_0 - \frac{\beta}{\alpha\tau} z_1 + \frac{1}{\alpha^2\tau} r_0 \tag{5.17}$$

$$\dot{z}_2 = \frac{(\alpha-1)}{\alpha^3\tau} z_0 + \frac{(\alpha-1)\beta}{\alpha^2\tau} z_1 - \frac{\beta^2}{\alpha\tau} z_2 + \frac{1}{\alpha^3\tau} r_0 \tag{5.18}$$
$$\vdots \tag{5.19}$$
$$\dot{z}_{m-1} = \frac{(\alpha-1)}{\alpha^m\tau} z_0 + \frac{(\alpha-1)\beta}{\alpha^{m-1}\tau} z_1 + \cdots + \frac{(\alpha-1)\beta^{m-2}}{\alpha^2\tau} z_{m-2} - \frac{\beta^{m-1}}{\alpha\tau} z_{m-1} + \frac{1}{\alpha^m\tau} r_0 \tag{5.20}$$
$$y_{m-1} = \frac{(\alpha-1)}{\alpha^m} z_0 + \frac{(\alpha-1)\beta}{\alpha^{m-1}} z_1 + \cdots + \frac{(\alpha-1)\beta^{m-1}}{\alpha} z_{m-2} + \frac{1}{\alpha^m} r_0 \tag{5.21}$$

From here it we can present everything in a compact matrix formalism by considering a state vector $\mathbf{z} = \begin{bmatrix} z_0 & z_1 & \cdots & z_{m-1} \end{bmatrix}^\dagger$ and we get the following compact form of state space model:

$$\begin{aligned} \dot{\mathbf{z}} &= \mathbf{A}_c\mathbf{z}+\mathbf{B}_c r_0 \\ y_{m-1} &= \mathbf{C}^\dagger\mathbf{z}+\mathbf{D}r_0 \end{aligned} \tag{5.22}$$

and the matrices are made up of the coefficients in the coupled differential equations above as shown below:

$$\begin{aligned} \mathbf{A}_c &= \begin{bmatrix} -\frac{\beta^0}{\alpha^1\tau} & 0 & \cdots & 0 & 0 \\ \frac{(\alpha-1)\beta^0}{\alpha^2\tau} & -\frac{\beta^1}{\alpha^1\tau} & \cdots & 0 & 0 \\ \vdots & \vdots & \ddots & \vdots & \vdots \\ \frac{(\alpha-1)\beta^0}{\alpha^{m-1}\tau} & \frac{(\alpha-1)\beta^1}{\alpha^{m-2}\tau} & \cdots & -\frac{\beta^{m-2}}{\alpha^1\tau} & 0 \\ \frac{(\alpha-1)\beta^0}{\alpha^m\tau} & \frac{(\alpha-1)\beta^1}{\alpha^{m-1}\tau} & \cdots & \frac{(\alpha-1)\beta^{m-2}}{\alpha^2\tau} & -\frac{\beta^{m-1}}{\alpha^1\tau} \end{bmatrix} \\ \mathbf{B}_c^\dagger &= \begin{bmatrix} \frac{1}{\alpha^1\tau} & \frac{1}{\alpha^2\tau} & \cdots & \frac{1}{\alpha^m\tau} \end{bmatrix} \\ \mathbf{C}^\dagger &= \begin{bmatrix} \frac{(\alpha-1)\beta^0}{\alpha^m} & \frac{(\alpha-1)\beta^1}{\alpha^{m-1}} & \cdots \frac{(\alpha-1)\beta^{m-1}}{\alpha^1} \end{bmatrix} \\ \mathbf{D} &= \begin{bmatrix} \frac{1}{\alpha^m} \end{bmatrix} \end{aligned} \tag{5.23}$$

In compact form, the resulting continuous-time state space is as follows:

$$\begin{aligned} \dot{\mathbf{z}} &= \mathbf{A}_c\mathbf{z}+\mathbf{B}_c r \\ w &= \mathbf{C}^\dagger\mathbf{z}+\mathbf{D}r \end{aligned} \tag{5.24}$$

where r is the input white noise, w is the estimated output flicker noise, $\mathbf{z}$ is the state vector and the continuous-time matrices $\mathbf{A}_c$, $\mathbf{B}_c$, $\mathbf{C}$ and $\mathbf{D}$ for model size $m = 4$ are given by:

$$\begin{aligned} \mathbf{A}_c &= \begin{bmatrix} -\frac{1}{\alpha\tau} & 0 & 0 & 0 \\ \frac{(\alpha-1)}{\alpha^2\tau} & -\frac{\beta}{\alpha\tau} & 0 & 0 \\ \frac{(\alpha-1)}{\alpha^3\tau} & \frac{(\alpha-1)\beta}{\alpha^2\tau} & -\frac{\beta^2}{\alpha\tau} & 0 \\ \frac{(\alpha-1)}{\alpha^4\tau} & \frac{(\alpha-1)\beta}{\alpha^3\tau} & \frac{(\alpha-1)\beta^2}{\alpha^2\tau} & -\frac{\beta^3}{\alpha\tau} \end{bmatrix} \\ \mathbf{B}_c^\dagger &= \begin{bmatrix} \frac{1}{\alpha\tau} & \frac{1}{\alpha^2\tau} & \frac{1}{\alpha^3\tau} & \frac{1}{\alpha^4\tau} \end{bmatrix} \\ \mathbf{C}^\dagger &= \begin{bmatrix} \frac{(\alpha-1)}{\alpha^4} & \frac{(\alpha-1)\beta}{\alpha^3} & \frac{(\alpha-1)\beta^2}{\alpha^2} & \frac{(\alpha-1)\beta^3}{\alpha} \end{bmatrix} \\ \mathbf{D} &= \begin{bmatrix} \frac{1}{\alpha^4} \end{bmatrix} \end{aligned} \tag{5.25}$$

The corresponding discrete-time state space model has the following form:

$$\begin{aligned} \mathbf{z}_{k+1} &= \mathbf{A}\mathbf{z}_k + \mathbf{B}r_k \\ w_k &= \mathbf{C}^{\dagger}\mathbf{z}_k + \mathbf{D}r_k \end{aligned} \tag{5.26}$$

where k represents the k^{th} time instance at time $t = kT$ for some sampling period T and the discrete-time matrices are given by:

$$\begin{aligned} \mathbf{A} &= e^{\mathbf{A}_c T} \\ \mathbf{B} &= \mathbf{A}_c^{-1}(e^{\mathbf{A}_c T} - \mathbf{I})\mathbf{B}_c \end{aligned} \tag{5.27}$$

Fig. 5.3 below shows the PSD plot of a flicker noise data (as reference) and the above Barnes-Jarvis discrete-time state space model simulation output with; $T = 12$ ms, $\lambda = -1$, $\tau = 500$ s, $\alpha = 3$ and $\beta = 9$. The flicker noise data was produced through a long process of repeatative filtering involving Fourier transform of white noise until the resulting spectral density has a slope of $\lambda = -1$.

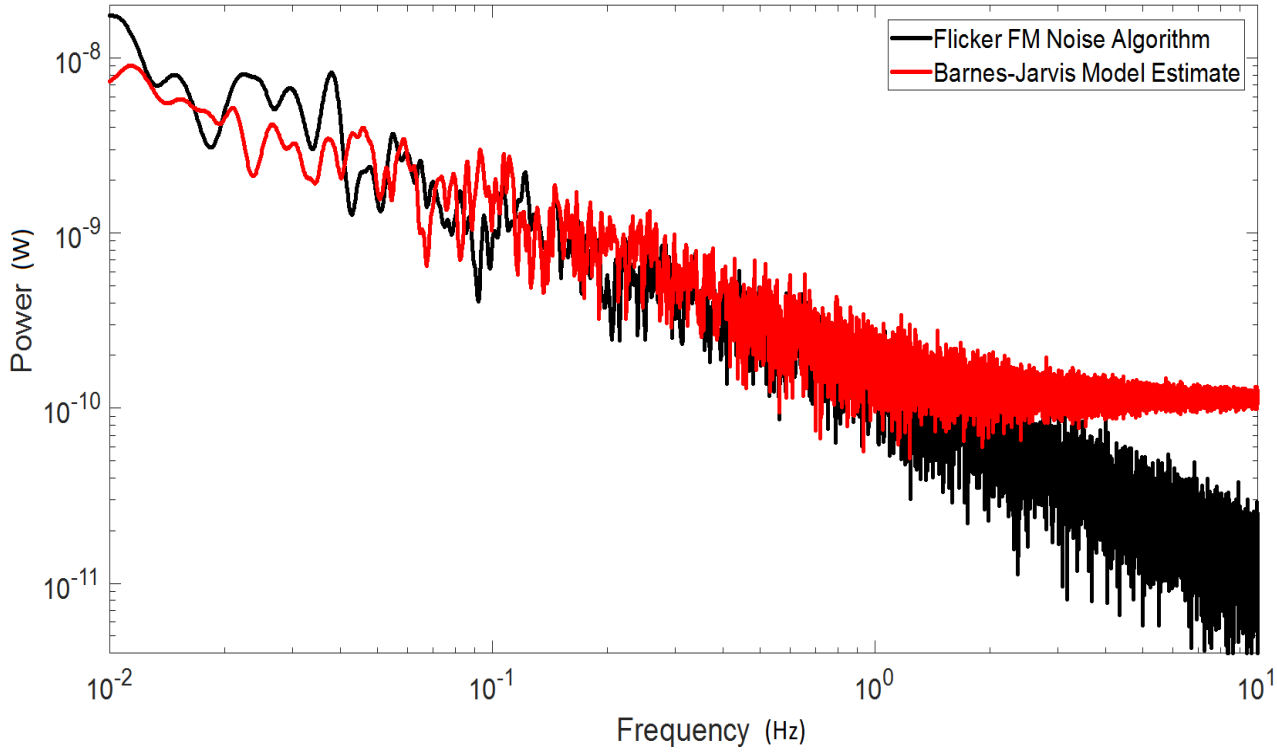

Fig. 5.3: Barnes-Jarvis discrete-time state space model simulation.

In Fig. 5.3 above it can seen that the Barnes-Jarvis model is approximating the flicker noise reasonably well for the first two decades and starts to flattens out afterwards thus, indicating that the Gaussian white noise is taking over the lead. This is also around the same frequency where our model seemed to deviate from the expected flicker noise slope in Fig. 5.1 and Fig. 5.2. From calculations this model should approximate well in the frequency range $[\frac{\beta^0}{2\pi\tau}, \frac{\beta^m}{2\pi\tau}] = [0.32 \text{ mHz}, 2.09 \text{ Hz}]$.

5.1.3 Mandelbrot State Space Model

For the same dynamic process there exists many state space representations which can be transformed from to another through some appropriate linear transforms. In the previous section we presented the state space model with a lower triangular transition matrix $\mathbf{A}_c$ as a consequence of deriving state space directly from Barnes-Jarvis cascade filter model. This transition matrix may not be favorable compared to diagonal transition matrix not just for complicating discretization but also for invoking some coupling among state components which may be preferable if they were identically independent in some probability distribution estimations. In this section we transform the Barnes-Jarvis cascade filter approach into a linear combination of low pass filters (LPFs), which resembles Mandelbrot-like model presented in [83]. This approach will yield a diagonal state transition matrix. We consider again the transfer function $G(s)$ as given in equation (5.8) and argue that the constituent cascade stages can be represented as a linear combination of corresponding low pass filters with the help of partial fractions as elaborated below.

The transfer function from Barnes-Jarvis model, Eq. (5.8), has the same degree in the numerator and denominator. However, before performing partial fractions decomposition the numerator polynomial must be at least one degree less than the denominator. This can be achieved by carrying out the long division which results in a constant quotient K and the remainder polynomial with at least one degree less than the divisor (denominator) polynomial as shown below:

$$\prod_{i=0}^{m-1} \frac{\tau s+\beta^i}{\alpha\tau s+\beta^i} = K + \sum_{i=0}^{m-1} \frac{\gamma_i}{\alpha\tau s+\beta^i} \tag{5.28}$$

with the unknowns s, γ_i and K. To find γ_i we simply multiply the above equation by the denominator $\alpha\tau s+\beta^i$ corresponding to γ_i and substitute the pole $s=-\beta^i/(\alpha\tau)$ throughout as shown below:

$$(\alpha\tau s+\beta^i)\prod_{j=0}^{m-1} \frac{\tau s+\beta^j}{\alpha\tau s+\beta^j}\Big|_{s=\frac{-\beta^i}{\alpha\tau}} = \gamma_i \tag{5.29}$$

The right-hand side leaves γ_i since the rest of the terms are effectively multiplied by zero. Simplifying the left-hand side and rearranging terms we arrive at:

$$\gamma_i = \frac{(\alpha-1)\beta^i}{\alpha^m} \prod_{\substack{j=0 \\ i\neq j}}^{m-1} \frac{\alpha\beta^j-\beta^i}{\beta^j-\beta^i} \tag{5.30}$$

To find K we just choose any of the numerator factor $\tau s+\beta^i$ and substitute its root $s=-\beta^i/\tau$ throughout. This forces the left-hand side of Eq. (5.28) to be zero so that we can express K as follows:

$$K = -\sum_{j=0}^{m-1} \frac{\gamma_j}{\alpha\tau s + \beta^j}\Big|_{s=\frac{-\beta^i}{\tau}} \tag{5.31}$$

$$= \sum_{j=0}^{m-1} \frac{\gamma_j}{\alpha\beta^i - \beta^j} \tag{5.32}$$

The resulting equivalent transfer function is of the following form:

$$G(s) = \prod_{i=0}^{m-1} \frac{\tau s + \beta^i}{\alpha\tau s + \beta^i} \tag{5.33}$$

$$= \sum_{i=0}^{m-1} \frac{\gamma_i}{\alpha\beta^j - \beta^i} + \sum_{i=0}^{m-1} \frac{\gamma_i}{\alpha\tau s + \beta^i}$$

where γ_i is given by

$$\gamma_i = \frac{(\alpha-1)\beta^i}{\alpha^m} \prod_{\substack{j=0 \\ i \neq j}}^{m-1} \frac{\alpha\beta^j - \beta^i}{\beta^j - \beta^i} \tag{5.34}$$

The details of partial fractions procedure for the above model can be found in the Appendix. Fig. 5.4 below shows the Bode plot of this transfer function together with its constituent low pass filters for settings $m = 4$, $\lambda = -1$, $\tau = 500$ s, $\alpha = 3$ and $\beta = 9$.

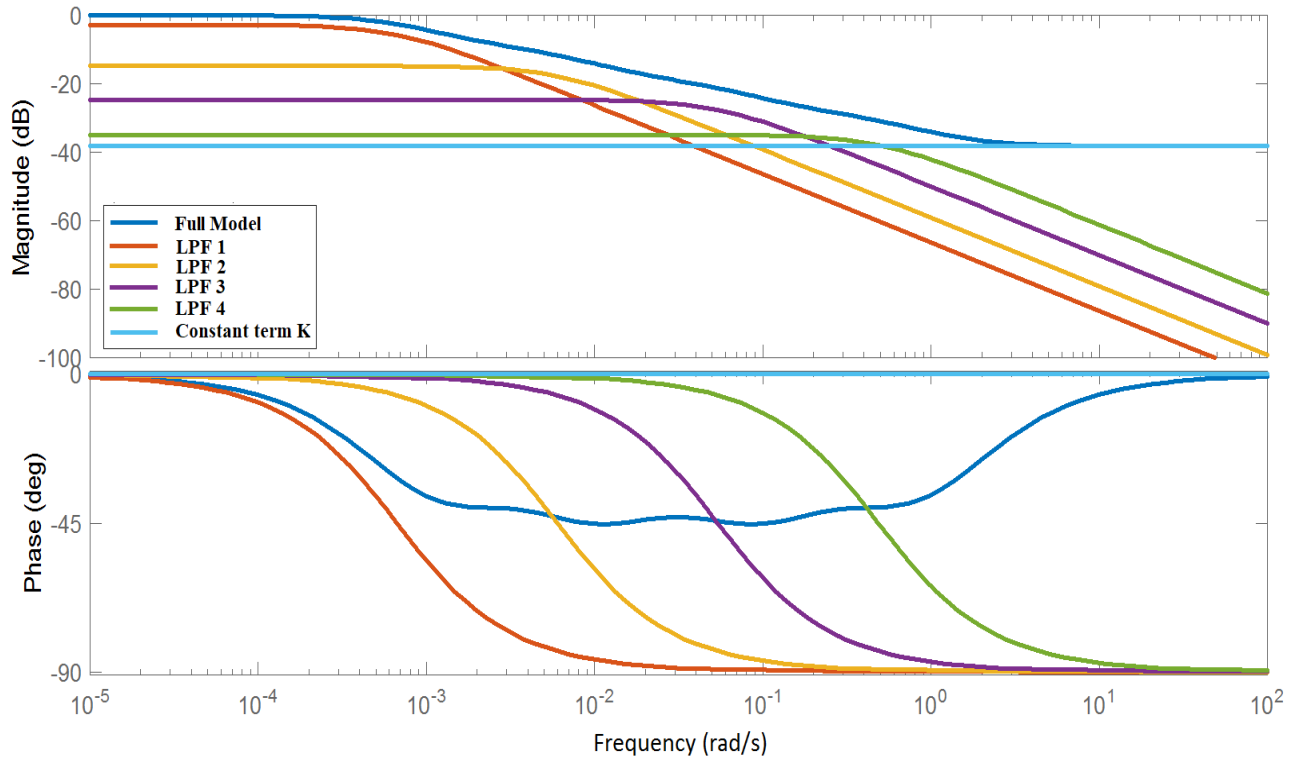

Fig. 5.4: Bode diagram for Mandelbrot model.

Fig. 5.5 below shows the log-log plot of the above model superimposed on the exact/expected flicker noise spectral plot.

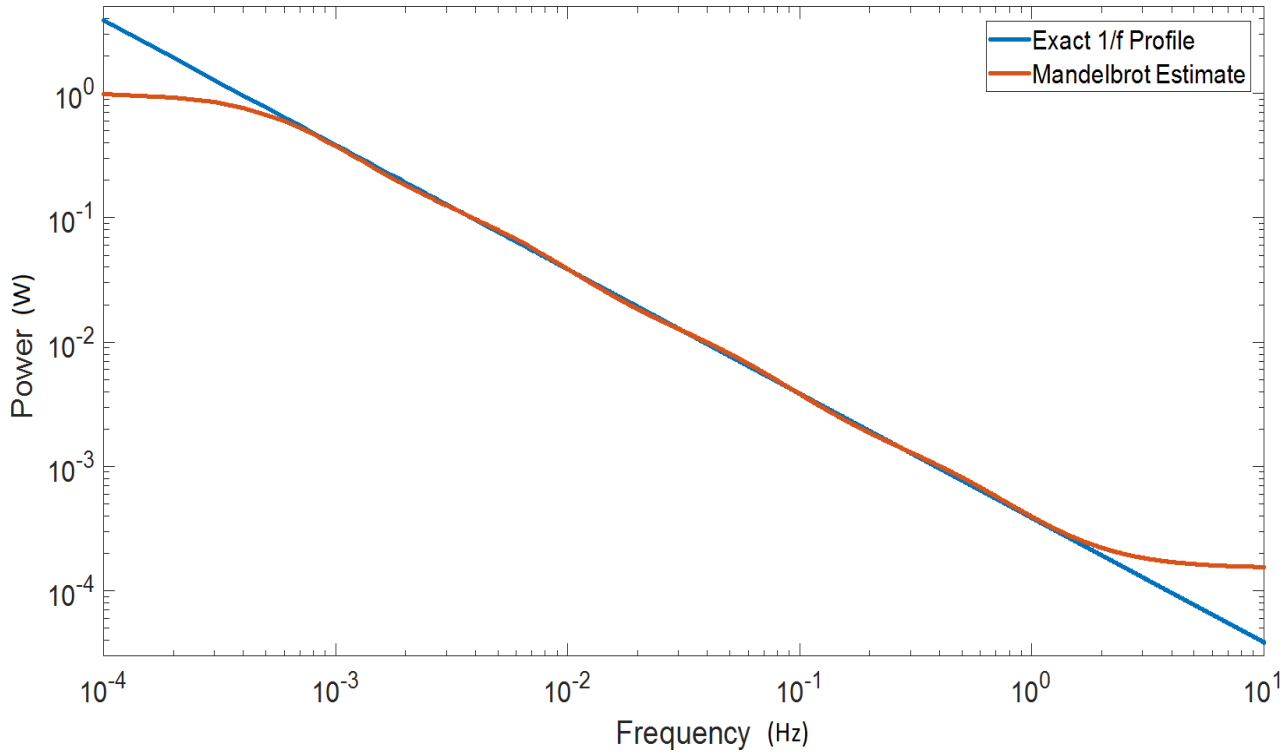

Fig. 5.5: Mandelbrot model power spectral density fit.

Converting the above transfer function to state space is pretty straight forward. We need only convert one low pass filter and copy the procedure to the rest of the low pass filters. To convert the i^{th} component of the Mandelbrot transfer function, Eq. (5.33), from frequency to time domain we follow the same procedure shown previously with Barnes-Jarvis cascade stage. The i^{th} low pass filter component leads to the following:

$$\frac{Y_i(s)}{R_i(s)} = \frac{\gamma_i}{\alpha\tau s + \beta^i}\frac{Z_i(s)}{Z_i(s)} \tag{5.35}$$

Which gives rise to the following state space model:

$$\dot{z}_i(t) = \frac{-\beta^i}{\alpha\tau}z_i(t) + \frac{1}{\alpha\tau}r_i(t) \tag{5.36}$$

$$y_i(t) = \gamma_i z_i(t) \tag{5.37}$$

The constant K gives $y_m(t) = Kr_m(t)$. In this case the internal states $z_i(t)$ are not coupled and the output $y_M(t)$ is given by the sum of all component outputs $y_i(t)$. The resulting equations are as shown below:

$$\dot{z}_0 = -\frac{\beta^0}{\alpha\tau}z_0 + \frac{1}{\alpha\tau}r_0 \tag{5.38}$$

$$\dot{z}_1 = -\frac{\beta^1}{\alpha\tau}z_1 + \frac{1}{\alpha\tau}r_1 \tag{5.39}$$

$$\tag{5.40}$$

$$\dot{z}_2 = -\frac{\beta^2}{\alpha\tau}z_2 + \frac{1}{\alpha\tau}r_2 \tag{5.41}$$

$$\vdots \tag{5.42}$$

$$\dot{z}_{m-1} = -\frac{\beta^{m-1}}{\alpha\tau}z_{m-1} + \frac{1}{\alpha\tau}r_{m-1} \tag{5.43}$$

$$\tag{5.44}$$

$$y_M = \gamma_0 z_0 + \gamma_1 z_1 + \cdots + \gamma_{m-1}z_{m-1} + Kr_m \tag{5.45}$$

In compact form with state vector $\mathbf{z} = \begin{bmatrix} z_0 & z_1 & \cdots & z_{m-1} \end{bmatrix}^\dagger$ and input vector $\mathbf{r} = \begin{bmatrix} r_0 & r_1 & \cdots & r_{m-1} \end{bmatrix}^\dagger$ we get the following:

$$\dot{\mathbf{z}} = \mathbf{A}_c\mathbf{z} + \mathbf{B}_c\mathbf{r} \tag{5.46}$$

$$y_M = \mathbf{C}^\dagger\mathbf{z} + \mathbf{D}r_m \tag{5.47}$$

where the matrices are given by:

$$\begin{aligned}
\mathbf{A}_c &= \frac{-1}{\alpha\tau}diag(\begin{bmatrix} \beta^0 & \beta^1 & \beta^2 & \cdots \beta^{m-1} \end{bmatrix}) \\
\mathbf{B}_c &= \frac{1}{\alpha\tau}diag\begin{bmatrix} 1 & 1 & 1 & \cdots & 1 \end{bmatrix} && (5.48) \\
\mathbf{C}^\dagger &= \begin{bmatrix} \gamma_0 & \gamma_1 & \gamma_2 & \cdots \gamma_{m-1} \end{bmatrix} && (5.49) \\
\mathbf{D} &= \begin{bmatrix} K \end{bmatrix}
\end{aligned}$$

Below we make a simplifying assumption that all input r_i are the same, however, in general they need not be the same. The resulting continuous-time state space model has the following form:

$$\begin{aligned}
\dot{\mathbf{z}} &= \mathbf{A}_c\mathbf{z} + \mathbf{B}_c r \\
w &= \mathbf{C}^\dagger\mathbf{z} + \mathbf{D}r
\end{aligned} \tag{5.50}$$

where the continuous-time matrices for model size $m = 4$ are as follows:

$$\mathbf{A}_c = \frac{-1}{\alpha\tau}diag(\begin{bmatrix} \beta^0 & \beta^1 & \beta^2 & \beta^3 \end{bmatrix})$$

$$\begin{aligned}
\mathbf{B}_c^{\dagger} &= \frac{1}{\alpha\tau}\begin{bmatrix}1 & 1 & 1 & 1\end{bmatrix} \\
\mathbf{C}^{\dagger} &= \begin{bmatrix}\gamma_0 & \gamma_1 & \gamma_2 & \gamma_3\end{bmatrix} \\
\mathbf{D} &= \sum_{j=0}^{3}\frac{\gamma_j}{\alpha\beta^i - \beta^j}
\end{aligned} \tag{5.51}$$

The discretization procedure is the same as done with the Barnes-Jarvis model in the previous section and yields:

$$\begin{aligned}
\mathbf{z}_{k+1} &= \mathbf{A}\mathbf{z}_k + \mathbf{B}\mathbf{r}_k \\
\mathbf{s}_k &= \mathbf{C}^{\dagger}\mathbf{z}_k + \mathbf{D}\mathbf{r}_k
\end{aligned} \tag{5.52}$$

The corresponding discrete-time Mandelbrot model matrices are given by:

$$\begin{aligned}
\mathbf{A} &= \mathrm{diag}(\begin{bmatrix}e^{\frac{-\beta^0 T}{\alpha\tau}} & e^{\frac{-\beta^1 T}{\alpha\tau}} & e^{\frac{-\beta^2 T}{\alpha\tau}} & e^{\frac{-\beta^3 T}{\alpha\tau}}\end{bmatrix}) \\
\mathbf{B}^{\dagger} &= \begin{bmatrix}\frac{1-e^{\frac{-\beta^0 T}{\alpha\tau}}}{\beta^0} & \frac{1-e^{\frac{-\beta^1 T}{\alpha\tau}}}{\beta^1} & \frac{1-e^{\frac{-\beta^2 T}{\alpha\tau}}}{\beta^2} & \frac{1-e^{\frac{-\beta^3 T}{\alpha\tau}}}{\beta^3}\end{bmatrix} \\
\mathbf{C}^{\dagger} &= \begin{bmatrix}\gamma_0 & \gamma_1 & \gamma_2 & \gamma_3\end{bmatrix} \\
\mathbf{D} &= \sum_{j=0}^{3}\frac{\gamma_j}{\alpha\beta^i - \beta^j}
\end{aligned} \tag{5.53}$$

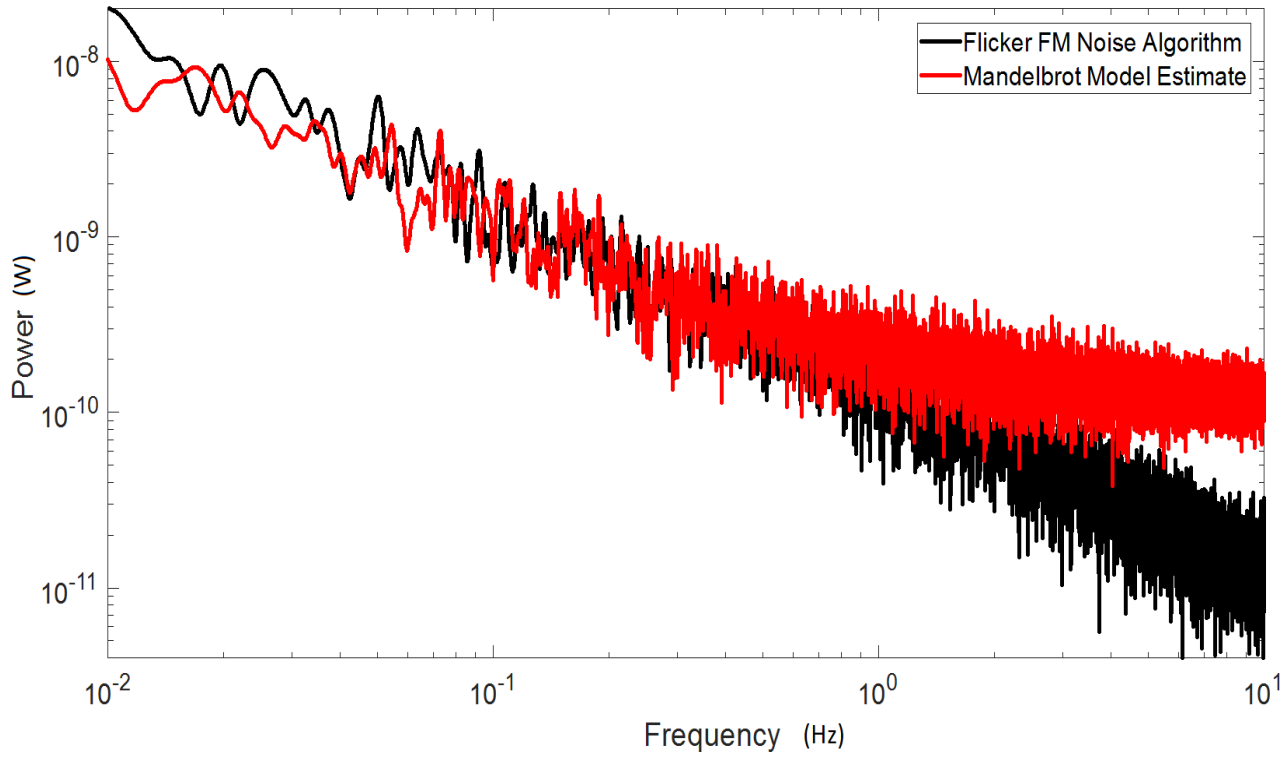

Fig. 5.6: Mandelbrot discrete-time state space model simulation.

An emphasis can be made on the discrete-time input matrix $\mathbf{B}$ that for it to be evaluated precisely, the continuous-time state transition matrix $\mathbf{A}_c$ needs to be full rank (non-singular). In the case whereby $\mathbf{A}_c$ is singular the first order Euler methods would suffice as approximate discrete models and the discrete-time state transition and input matrices would simply be $\mathbf{A} = \mathbf{I} + \mathbf{A}_c T$ and $\mathbf{B} = \mathbf{B}_c T$ respectively. Fig. 5.6 above shows the simulation of the corresponding discrete-time state space model with $T = 2$ s, $\lambda = -1$, $\tau = 500$ s, $\alpha = 3$, $\beta = 9$ and γ_i as given in equation (5.34). Just like with the Barnes-Jarvis there is a deviation from the expected slope after the first two decades. The approximation frequency range is the same as that of Barnes-Jarvis because the two models are related by a linear transformation.

5.2 Gaussian Mixture Model Reduction Algorithm

One of the challenges of using GMMs is determining the necessary number of Gaussian components to represent the underlying distribution. In the framework of the power low noise models, presented in the previous sections, this problem is re-phrased in terms of the model size required to describe the underlying power law noise adequately within a certain band of frequencies, given some desired accuracy. This can be achieved by comparing the expected PSD and that of the model and adjusting the model size to meet the given specifications. There are various ways of keeping track of the approximate posterior distribution when the underlying prior and likelihood are mixtures of Gaussian distributions. One example being the use of particle filter [77,78]. In this work we adopt the truncation approach which relies on Kullback-Leibler reduction algorithm as presented in [79,80].

5.2.1 Problem Description

Consider the following linear system dynamics with additive power law noise $\mathbf{w}_k \in \mathbb{R}^n$ in the process dynamics and $\mathbf{v}_k \in \mathbb{R}^m$ in the observation;

$$\begin{aligned} \mathbf{x}_{k+1} &= \mathbf{F}\mathbf{x}_k + \mathbf{G}\mathbf{u}_k + \mathbf{w}_k \\ \mathbf{y}_k &= \mathbf{H}^{\dagger}\mathbf{x}_k + \mathbf{v}_k \end{aligned} \tag{5.54}$$

where $\mathbf{x}_k \in \mathbb{R}^n$ is the process state vector, $\mathbf{u}_k \in \mathbb{R}^l$ is the input vector, $\mathbf{y}_k \in \mathbb{R}^m$ is the observation vector, $\mathbf{F} \in \mathbb{R}^{n\times n}$ is the state transition matrix, $\mathbf{G} \in \mathbb{R}^{n\times l}$ is the input-to-state matrix and $\mathbf{H} \in \mathbb{R}^{m\times n}$ is the observation matrix. The power law noise vectors $\mathbf{w}_k$ and $\mathbf{v}_k$ can be modeled compactly as follows;

$$\begin{aligned} \mathbf{z}_{k+1} &= \mathbf{A}\mathbf{z}_k + \mathbf{B}\mathbf{r}_k \\ \mathbf{s}_k &= \mathbf{C}^{\dagger}\mathbf{z}_k + \mathbf{D}\mathbf{r}_k \end{aligned} \tag{5.55}$$

where $\mathbf{z}_k \in \mathbb{R}^{p\times(n+m)}$is the state matrix for power law noise, $\mathbf{r}_k \in \mathbb{R}^{q\times(n+m)}$ is the input white Gaussian noise matrix and $\mathbf{s}_k = \begin{bmatrix} \mathbf{w}_k^{\dagger} & \mathbf{v}_k^{\dagger} \end{bmatrix} \in \mathbb{R}^{1\times(n+m)}$ is the row vector of power law noise components. The

probability distributions associated with the process in equation (5.54) are approximated by the Gaussian mixture models whose dimensions are chosen based on the number of Gaussian noise elements used in constructing the associated power law noise model; in this case $p+q$ Gaussian noise elements. The prior probability distribution is described by;

$$p(\mathbf{x}_1) = \sum_{h=1}^{N_p} \alpha_i \mathcal{N}(\mathbf{x}_1; \mu_1^h, \mathbf{P}_1^h) \tag{5.56}$$

with weights satisfying $\sum_{h=1}^{N_p} \alpha_h = 1$. The process model is of the form;

$$p(\mathbf{x}_{k+1}|\mathbf{x}_k) = \sum_{i=1}^{N_x} \beta_k^i \mathcal{N}(\mathbf{x}_{k+1}; \mathbf{F}\mathbf{x}_k + \mathbf{G}\mathbf{u}_k + \mu_k^i, \mathbf{Q}_k^i) \tag{5.57}$$

with weights satisfying $\sum_{i=1}^{N_x} \beta_i = 1$. The measurement model is of the form;

$$p(\mathbf{y}_k|\mathbf{x}_k) = \sum_{j=1}^{N_y} \gamma_k^j \mathcal{N}(\mathbf{y}_k; \mathbf{H}^\dagger \mathbf{x}_k + \upsilon_k^j, \mathbf{R}_k^j) \tag{5.58}$$

with weights satisfying $\sum_{j=1}^{N_y} \gamma_j = 1$. The form $\mathcal{N}(\mathbf{x}; \mu, \mathbf{P})$ above is used to denote a standard multivariate Gaussian distribution. The mean offset terms μ_k^i and υ_k^j are due to the fact that the Gaussian terms that make up the power law noise may not necessarily be zero-mean. Given a set of measurement outcomes $\mathbf{Y}_M = \{\mathbf{y}_1, \mathbf{y}_2, \ldots, \mathbf{y}_M\}$ we can update the distributions in a Bayesian fashion as shown below;

$$\begin{aligned} p(\mathbf{x}_k|\mathbf{Y}_k) &= \frac{p(\mathbf{y}_k|\mathbf{x}_k)p(\mathbf{x}_k|\mathbf{Y}_{k-1})}{p(\mathbf{y}_k|\mathbf{Y}_{k-1})} \\ p(\mathbf{x}_{k+1}|\mathbf{Y}_k) &= \int p(\mathbf{x}_{k+1}|\mathbf{x}_k)p(\mathbf{x}_k|\mathbf{Y}_k)d\mathbf{x}_k \end{aligned} \tag{5.59}$$

However, it becomes immediately obvious that the posterior distribution terms keep blowing up in number on each iteration k and cannot be efficiently handled. There are various ways of tackling this problem in the literature, such as using particle filter, but in this work we adopt the Kullback-Leibler GMM reduction method. The next section briefly outlines the Kullback-Leibler GMM reduction method as presented in [79].

5.2.2 Kullback-Leibler GMM Reduction

The central idea in this reduction method is to reduce one GMM, with more terms, to an approximate GMM with fewer terms. That is, given the following GMM;

$$GMM_1(x) = \sum_{i=1}^{N} \omega_i \mathcal{N}(x; \mu_i, P_i) \tag{5.60}$$

with weights satisfying $\sum_{i=1}^{N} \omega_i = 1$, the reduction method seeks to find another GMM;

$$GMM_2(x) = \sum_{i=1}^{M} \upsilon_i \mathcal{N}(x; \nu_i, Q_i) \tag{5.61}$$

with weights satisfying $\sum_{i=1}^{N} \upsilon_i = 1$, such that $1 \leq M \leq N$. As presented in [79], the mechanism for achieving this is by picking two Gaussian components and merging them together to form one Gaussian component. This process is repeated until the desired number of Gaussian components M is obtained. In [79] the following merge that preserves the first and second-order moments of the original two components is employed;

$$f(\omega_i \mathcal{N}(x; \mu_i, P_i), \omega_j \mathcal{N}(x; \mu_j, P_j)) = \omega_{ij} \mathcal{N}(x; \mu_{ij}, P_{ij}) \tag{5.62}$$

where

$$\begin{aligned}
\omega_{ij} &= \omega_i + \omega_j \\
\mu_{ij} &= \omega_{i|ij}\mu_i + \omega_{j|ij}\mu_j \\
P_{ij} &= \omega_{i|ij}P_i + \omega_{j|ij}P_j \\
&\quad + \omega_{i|ij}\omega_{j|ij}(\mu_i - \mu_j)(\mu_i - \mu_j)^{\dagger} \\
\omega_{i|ij} &= \frac{\omega_i}{\omega_i + \omega_j} \\
\omega_{j|ij} &= \frac{\omega_j}{\omega_i + \omega_j}
\end{aligned} \tag{5.63}$$

The bound on the discrimination between the mixtures before and after reduction of a component pair is given by;

$$B(i,j) \triangleq \frac{1}{2}\left[\omega_{ij}\log|P_{ij}| - \omega_i \log|P_i| - \omega_j \log|P_j|\right] \tag{5.64}$$

So choosing the i^{th} and j^{th} components to merge such that $B(i,j)$ is minimized will ensure that there is minimal change between the original mixture and the new reduced mixture. More details about the Kullback-Leibler reduction method and its algorithm can be found in [79] and [80].

5.2.3 Recursive Filter Equations

Similar to the Kalman filter, the filtering algorithm using GMM has a prediction step and an update step but unlike the Kalman filter there is an additional step of Kullback-Leibler GMM reduction. In

this section we present, for completeness, the closed form solution to the filtering problem as outlined in [79]. Given the following prediction mixture:

$$p(\mathbf{x}_k|\mathbf{Y}_{k-1}) = \sum_{l=1}^{N_{k|k-1}} \omega_{k|k-1}^l \mathcal{N}(\mathbf{x}_k; \hat{\mathbf{x}}_{k|k-1}^l, \mathbf{P}_{k|k-1}^l) \tag{5.65}$$

with weights satisfying $\sum_{l=1}^{N_{k|k-1}} \omega_{k|k-1}^l = 1$, the measurement update is expressed in the following GMM setting as:

$$\begin{aligned} p(\mathbf{x}_k|\mathbf{Y}_k) &= \sum_{l=1}^{N_{k|k-1}} \sum_{j=1}^{N_y} \omega_{k|k-1}^l \gamma_k^j \\ &\quad \times \frac{\mathcal{N}(\mathbf{y}_k; \mathbf{H}^\dagger \mathbf{x}_k + \upsilon_k^j, \mathbf{R}_k^j)}{p(\mathbf{y}_k|\mathbf{Y}_{k-1})} \\ &\quad \times \mathcal{N}(\mathbf{x}_k; \hat{\mathbf{x}}_{k|k-1}^l, \mathbf{P}_{k|k-1}^l) \\ &= \sum_{s=1}^{N_{k|k}} \omega_{k|k}^s \mathcal{N}(\mathbf{x}_k; \hat{\mathbf{x}}_{k|k}^s, \mathbf{P}_{k|k}^s) \end{aligned} \tag{5.66}$$

with weights satisfying $\sum_{s=1}^{N_{k|k}} \omega_{k|k}^s = 1$, $k = 1, \ldots, N_y$ and $l = 1, \ldots, N_{t|t-1}$ such that:

$$\begin{aligned} N_{k|k} &= N_{k|k-1} N_y \\ s &\triangleq N_y(s-1) + j \\ \hat{\mathbf{x}}_{k|k}^s &= \hat{\mathbf{x}}_{k|k}^l + \mathbf{K}_k^s \mathbf{e}_k^s \\ \mathbf{e}_k^s &= \mathbf{y}_k - \mathbf{H}^\dagger \hat{\mathbf{x}}_{k|k}^l - \mathbf{J}\mathbf{u}_k - \upsilon_k^j \\ \mathbf{E}_k^s &= \mathbf{H}^\dagger \mathbf{P}_{k|k-1}^l \mathbf{H} + \mathbf{R}_k^j \\ \mathbf{K}_k^s &= \mathbf{P}_{k|k-1}^l \mathbf{H} (\mathbf{E}_k^s)^{-1} \\ \mathbf{P}_{k|k}^s &= \mathbf{P}_{k|k-1}^l - \mathbf{K}_k^s \mathbf{E}_k^s (\mathbf{K}_k^s)^\dagger \\ \omega_{k|k}^s &= \bar{\omega}_{k|k}^s (\sum_{s=1}^{N_{k|k}} \bar{\omega}_{k|k}^s)^{-1} \\ \bar{\omega}_{k|k}^s &= \frac{\omega_{k|k-1}^l \gamma_k^j \exp(-\frac{1}{2}(\mathbf{e}_k^s)^\dagger (\mathbf{E}_k^s)^{-1} \mathbf{e}_k^s)}{(2\pi|\mathbf{E}_k^s|)^{\frac{1}{2}}} \end{aligned} \tag{5.67}$$

The next prediction mixture can also be updated as follows:

$$
\begin{aligned}
p(\mathbf{x}_{k+1}|\mathbf{Y}_k) &= \sum_{s=1}^{N_{k|k}} \sum_{i=1}^{N_x} \omega_{k|k-1}^s \beta_k^i \\
&\times \int \mathcal{N}(\mathbf{x}_{k+1}; \mathbf{F}\mathbf{x}_k + \mathbf{G}\mathbf{u}_k \\
&+ \mu_k^i, \mathbf{Q}_k^i) \mathcal{N}(\mathbf{x}_k; \hat{\mathbf{x}}_{k|k}^s, \mathbf{P}_{k|k}^s) d\mathbf{x}_k
\end{aligned} \tag{5.68}
$$

which reduces to:

$$
p(\mathbf{x}_{k+1}|\mathbf{Y}_k) = \sum_{l=1}^{N_{k+1|k}} \omega_{k+1|k}^l \mathcal{N}(\mathbf{x}_{k+1}; \hat{\mathbf{x}}_{k+1|k}^l, \mathbf{P}_{k+1|k}^l) \tag{5.69}
$$

with weights satisfying $\sum_{l=1}^{N_{k+1|k}} \omega_{k+1|k}^l = 1$, $s = 1, \ldots, N_{t|t}$ and $i = 1, \ldots, N_x$ such that the following equations hold:

$$
\begin{aligned}
N_{k+1|k} &= N_{k|k} N_x \\
l &\triangleq N_x(s-1) + i \\
\hat{\mathbf{x}}_{k+1|k}^l &= \mathbf{F}\hat{\mathbf{x}}_{k|k}^s + \mathbf{G}\mathbf{u}_k + \mu_k^i \\
\mathbf{P}_{k+1|k}^l &= \mathbf{F}\mathbf{P}_{k|k}^s \mathbf{F}^\dagger + \mathbf{Q}_k^i \\
\omega_{k+1|k}^l &= \omega_{k|k}^s \beta_k^i
\end{aligned} \tag{5.70}
$$

At this point we repeat the same process in the next iteration given a new measurement outcome. The filtering process can be summarized by the following block diagram in Fig. 5.7.

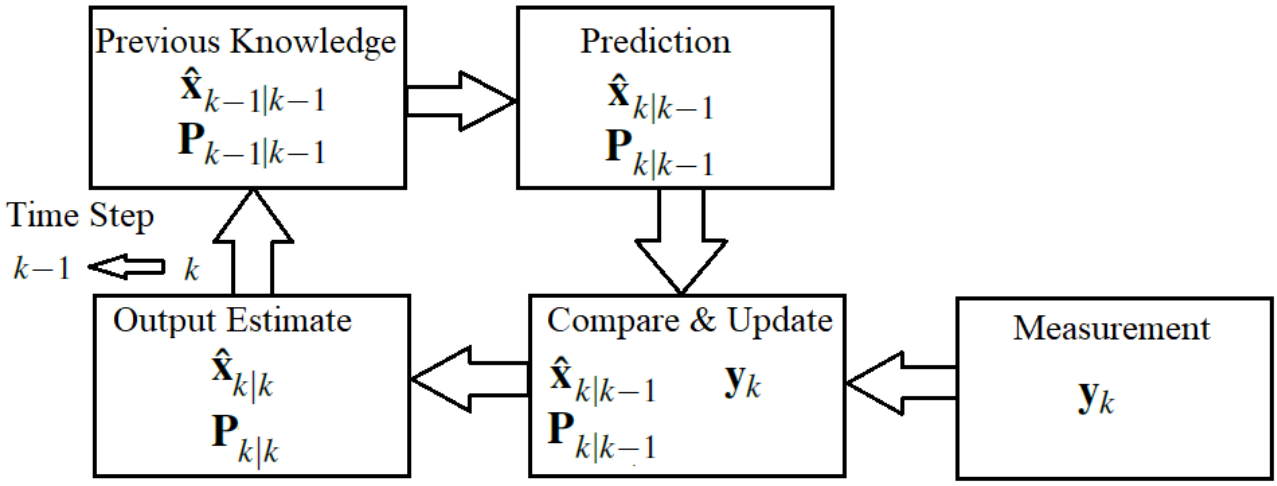

Fig. 5.7: Summary of the recursive Bayesian filtering in block diagram.

5.3 Flicker Noise Simulation Problem

Consider the following first order system with flicker noise associated;

$$\begin{aligned} x_{k+1} &= Fx_k + Gu_k + w_k \\ y_k &= Hx_k + v_k \end{aligned} \tag{5.71}$$

where $F = 1.00$, $G = 1.00$ and $H = 1.00$. The flicker noise terms w_k and v_k are simulated with the flicker noise algorithm shown in the previous diagrams. The input u_k is set to be a white noise with amplitude of order $\sim 10^{-6}$. The flicker noise terms are also of the same order in strength. A model of the system above can be represented as shown below with consideration of some possible modeling errors;

$$\begin{aligned} x_{k+1} &= Fx_k + Gu_k + \mu_k + w_k \\ y_k &= Hx_k + \nu_k + v_k \end{aligned} \tag{5.72}$$

where the modeling parameters (F, G, H) take on four combinations, $\{(1.20, 1.05, 1.02), (0.95, 1.25, 0.89), (1.10, 0.90\ 098), (1.05, 0.98, 1.03)\}$ each corresponding to one of the four components in the Gaussian mixture. Each of the combinations shows the possible model of the underlying first order system including some errors in model parameters. The process noise covariance and measurement noise covariance pair (Q, R) takes on four combinations, $\{(20, 5), (30, 3), (30, 4), (20, 2)\}$. The initial predicted and estimated process covariance pair $(P_{k|k-1}, P_k)$ takes on four combinations $\{(2, 2), (3, 3), (2, 3), (3, 2)\}$. The terms μ_k and ν_k account for possible additive modeling uncertainty which could be treated as the time-varying parameters. In this example we just take them to be white noise terms in the order of $\sim 10^{-6}$. We implement the GMM based filter as described in the previous section. We use four Gaussian components which correspond to the dimensionality of the Mandelbrot model size used to check the accuracy of the produced power spectral density. The mean of the Gaussian components is computed on every iteration and shown in the next simulation results. A Kalman filter performance is also shown alongside the GMM filter for comparison. For Kalman filter the model parameters were set to be $F = 1.05$, $G = 0.98$ and $H = 1.03$ to include some modeling errors. The process noise covariance and measurement noise covariance were set to be $Q = 20$ and $R = 2$ respectively.

Fig. 5.8 shows the prior and posterior distributions of the state x_k for both Kalman filter and the Gaussian mixture model-based filter (GMMF) during the second $(k = 2)$ and hundredth $(k = 100)$ iterations respectively. From the figure there is a relatively significant improvement in localization by GMMF prior from the second iteration to the hundredth iteration. The posterior for GMMF is much more localized and this probably because the states are all close to one another. In other words it would give a wider multimode distribution if the states were sufficiently further apart from each other. The averaging effect of GMMF gives it an edge on robustness in the face of modeling errors hence why its prior distribution is relatively more localized after a few iterations.

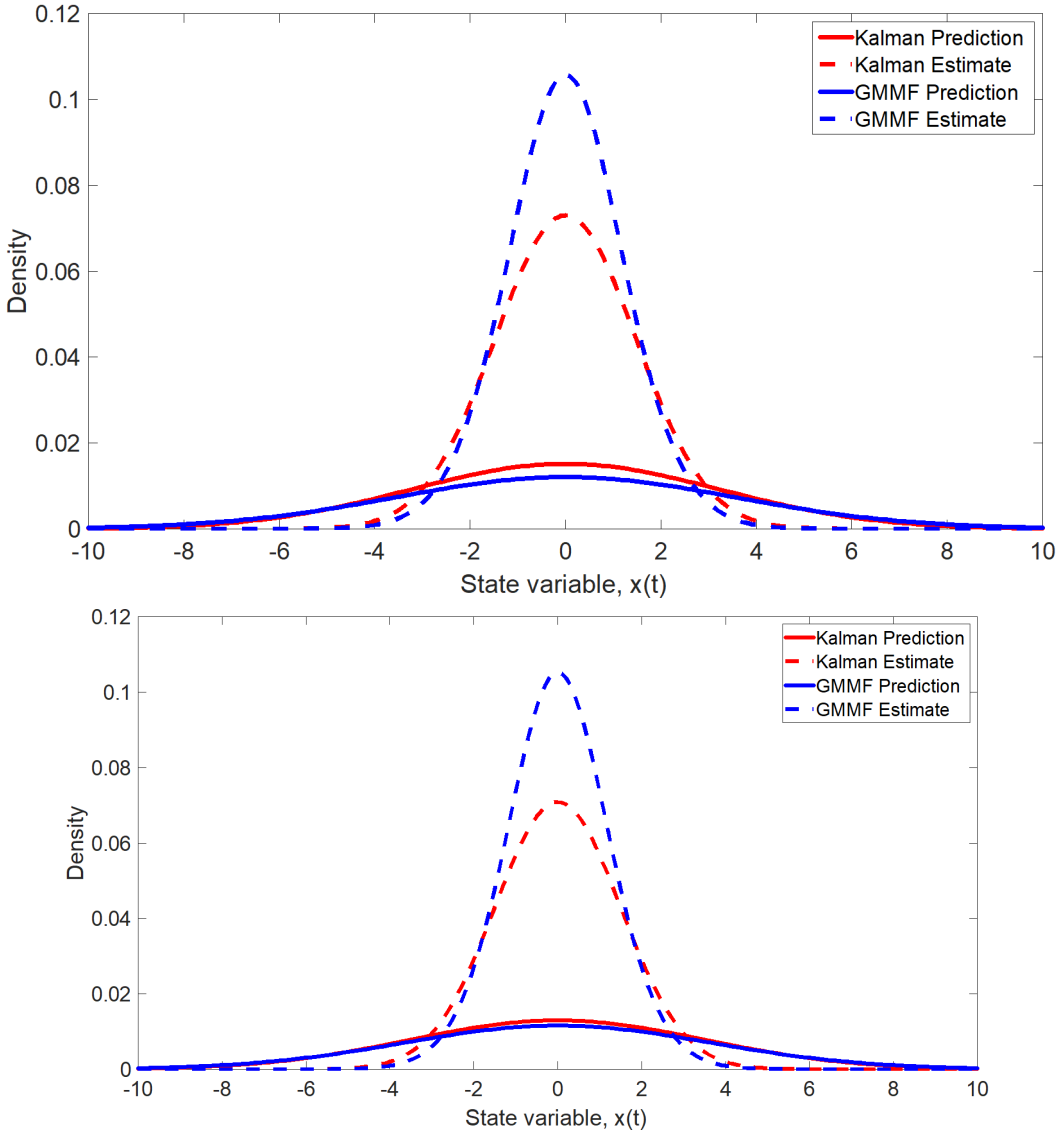

Fig. 5.8: Distributions on iteration 2 (top) and iteration 100 (bottom)

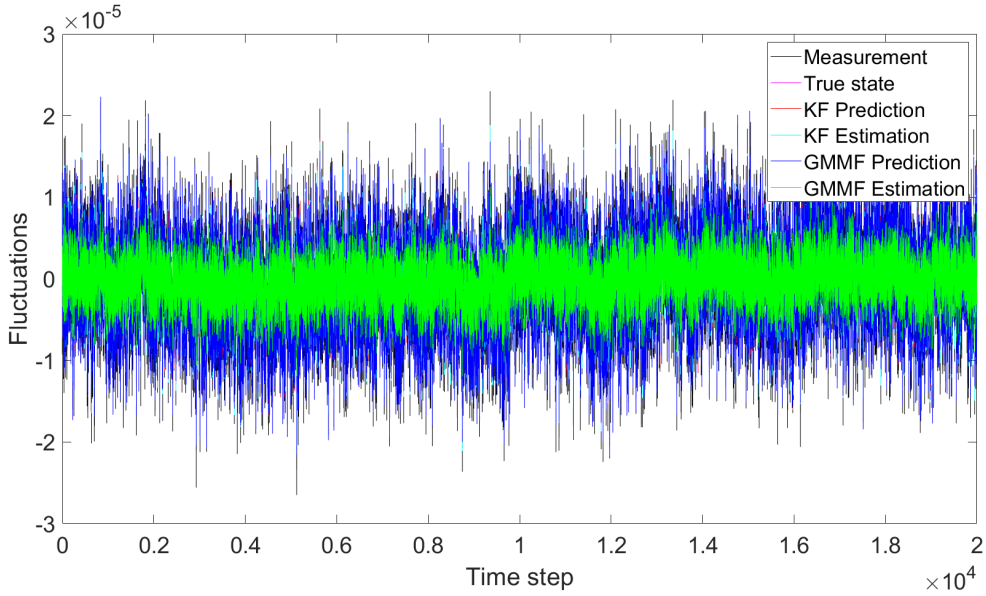

Fig. 5.9: Fluctuations in the predictions, estimations and measurement output y

Fig. 5.9 shows the plot of the fluctuations in the prediction and estimation for both Kalman and GMM Filter as well as fluctuations in the measurement and true state. The GMMF shows some relative suppression in the fluctuation and both Kalman filter and GMMF predictions are fairly comparable with the measurement fluctuations.

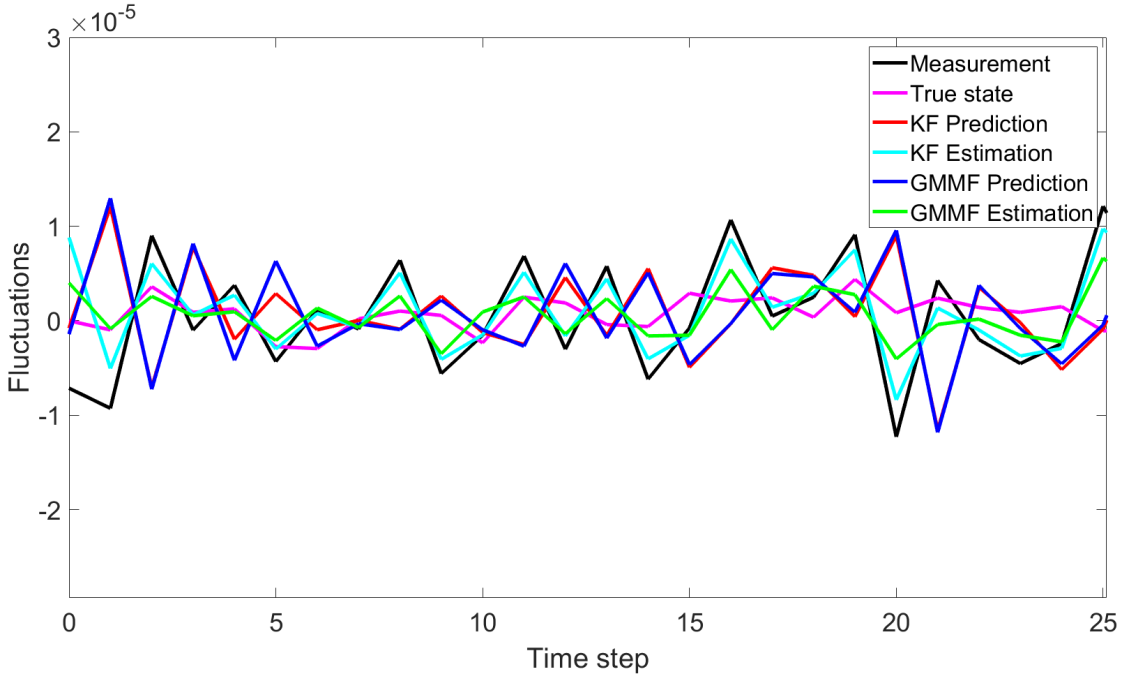

Fig. 5.10: Zoomed-in fluctuations in the predictions, estimations and measurement output y

Fig. 5.10 shows the first 25 time steps of the same plot in Fig. 5.9 to give a clearer picture of all the fluctuations. The slight reduction in estimated fluctuations of Kalman filter can be witnessed but not as clearly as in Fig. 5.11 below, showing the integral square error/fluctuations.

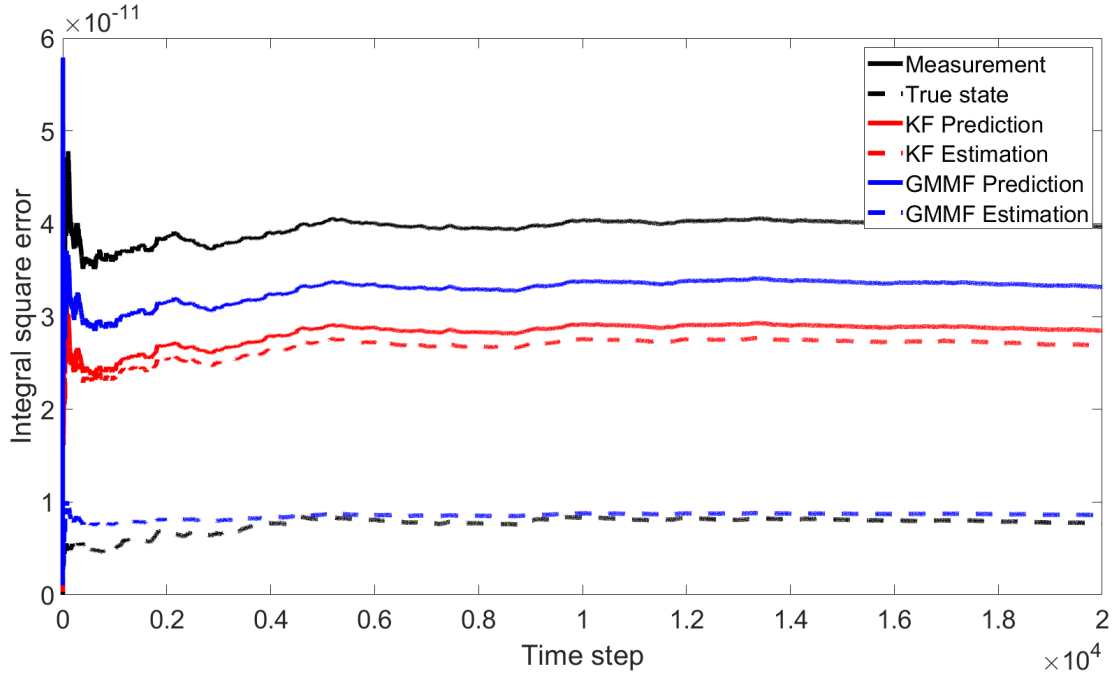

Fig. 5.11: Integral square error of the fluctuations.

Fig. 5.11 shows the integral square fluctuations of the Kalman filter and GMMF predictions and estimations as well as the measurement and true state. The GMMF prediction shows the highest square error/fluctuations which could be due to the modeling uncertainties in each of its prediction model components. The Kalman prediction on the other hand has a slightly less integral square error. Both the Kalman and GMMF estimation errors indicate some improvement of the filtered output as expected.

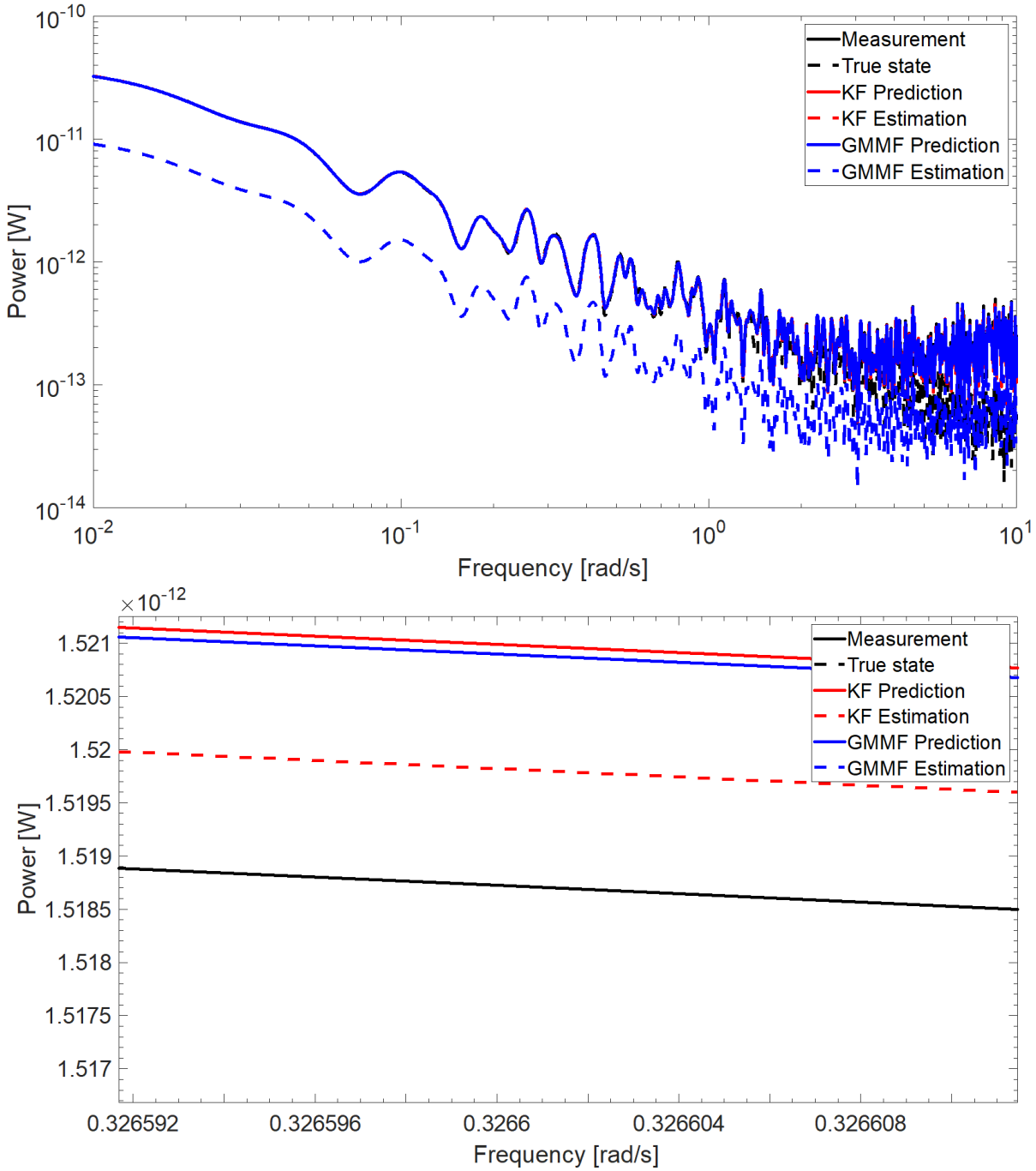

Fig. 5.12: Power spectral density of the fluctuations in predictions, estimations, measurement and true state. Full run (top) and zoomed portion (bottom).

Fig. 5.12 shows the corresponding power spectral density of the actual fluctuations of the predictions and estimations for both Kalman filter and GMM filter as well as that of the measurement and true state. Again the GMMF and Kalman filter show some reduction in the estimated fluctuations compared to the predicted ones.

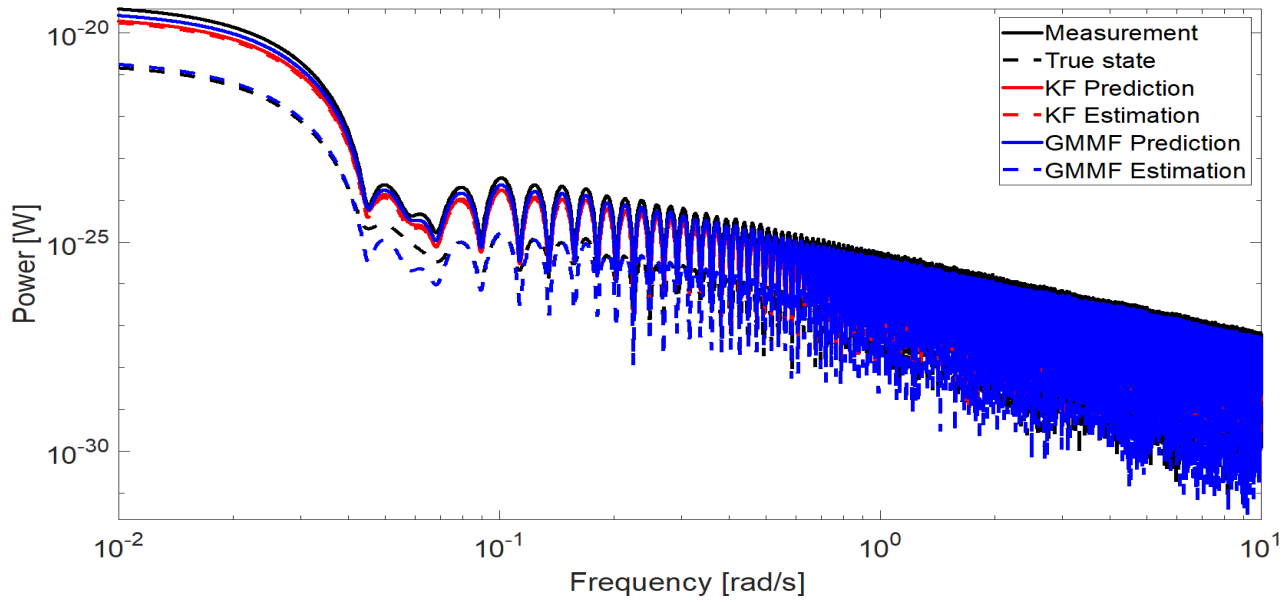

Fig. 5.13: Power spectral density of the integral square error in fluctuations.

Fig. 5.13 shows the power spectral density of the integral square error in fluctuations of the measurement, true state, predictions and estimations by Kalman filter and GMMF. The integral square fluctuations of estimations are relatively suppressed compared to the predicted counterparts as well as measurement in both Kalman filter and GMMF cases.

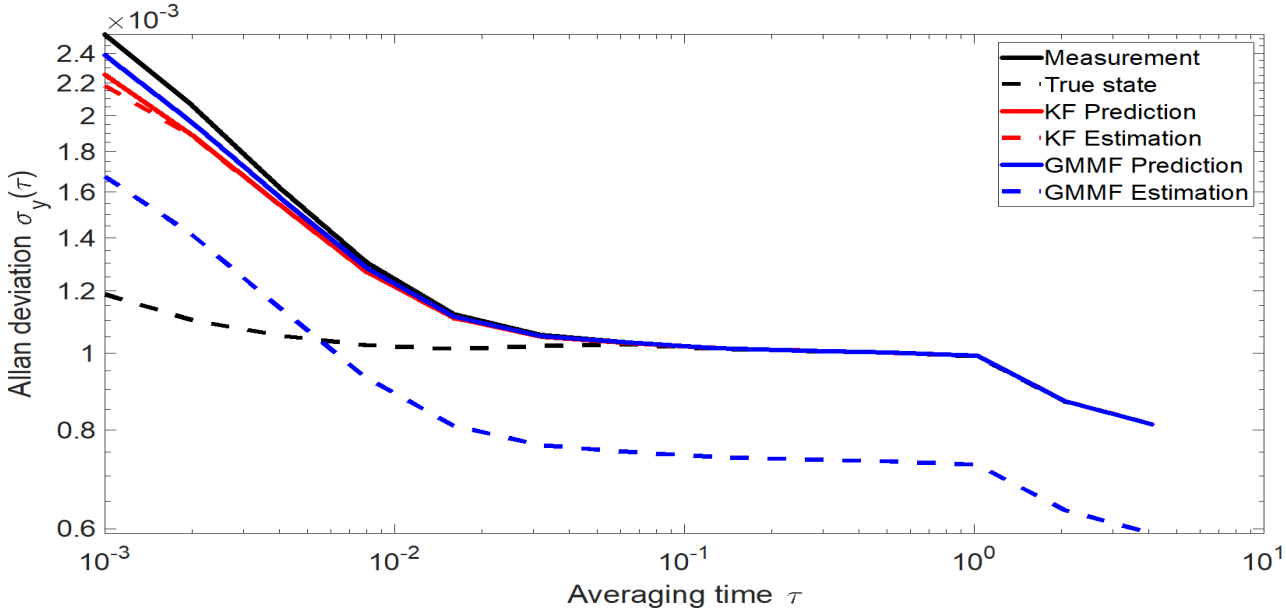

Fig. 5.14: Allan deviation of the fluctuations in predictions, estimations, measurement and true state

In Fig. 5.14 the Kalman filter shows a lot of reliance on the measurement than the prediction. On the sloping part of the Allan deviation plot which correspond to white noise, Kalman filter is below both measurement and predictions and that is indicative of its good performance in handling white noise. However, on the flat part, corresponding to the flicker noise, Kalman filter is as good as the measurement. The GMM filter shows a relatively significant improvement in all averaging times.

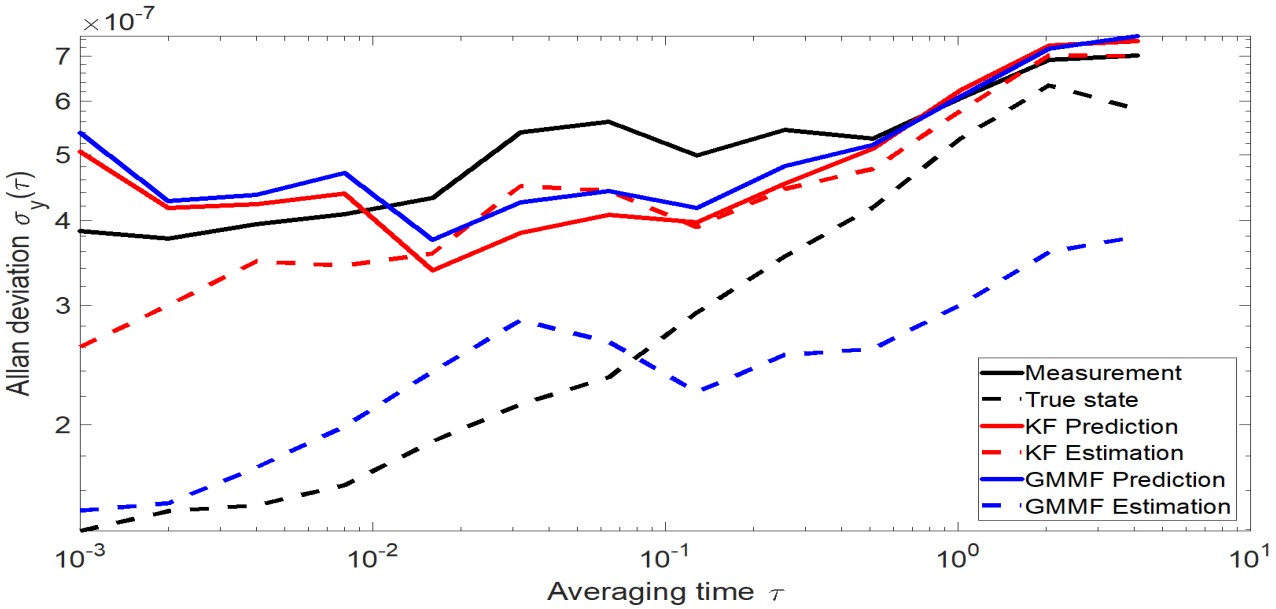

Fig. 5.15: Alan deviation of integral square error.

Fig. 5.15 shows the Allan deviation of the integral square fluctuations in measurement, true state, predicted and estimated signals. Both Kalman filter and GMMF show some significant refinement in the filtered error fluctuations relative to the respective predictions as expected.

5.4 Summary

In this work we presented Barnes-Jarvis and Mandelbrot state space models for generating power law noise in a linear time-invariant fashion. We also demonstrated a partial fraction-based transformation from Barnes-Jarvis cascaded transfer function model to Mandelbrot transfer function model under the assumption of a common/single input Gaussian noise source. These models gave us a way of approximating the power law noise in terms of components of well-known Gaussian white noise such that the precision of the approximation is dependent on the number of Gaussian white noise components used in the model, which is the model size. This way of representing the power law noise in terms of a mixture of Gaussian noise components allowed us to adopt the Gaussian mixture models as the framework for estimating and keeping track of the probability distributions associated with power law noise. This was demonstrated with a simulation of Bayesian filtering applied on a linear time-invariant process with flicker noise associated with both process dynamics and observation. In future work we wish to enforce the constraint on the Gaussian mixtures in GMM which preserves the fixed relationship on the weights of the mixture as required by the power law noise model structure. This will ensure that at all times the Gaussian mixture model is representative of the power law noise model and its distribution.

Chapter 6

Conclusion

In this work we successfully assembled a linear Paul trap under microscope and characterized its geometrical parameters with a laser beam. We designed and implemented a helical and an LC resonators for providing the trap electrodes with filtered and stepped up rf voltage at around 15 MHz from the function generator. These resonators were characterized using the inductive and capacitive probes for measurements of their responses. A positive feedback concept was presented and analyzed with intent of using it for designing resonator. The limiting factor for this positive feedback concept was found out to be the gain-bandwidth product of the components building up the circuit. For op-amps, this meant the operating frequency must be very low compared to the resonance frequency reported for our helical resonator. Importance of impedance matching in efficient delivery of power was addressed and implemented with a coupling coil for our helical resonator. Other LC these resonators, operating near 1 MHz, were implemented, characterized and aimed to be used to couple out rf signal from image currents induced on the trap electrodes.

We successfully trapped both single ions and cloud of ions for $^{171}Yb^{+}$ and $^{174}Yb^{+}$ and demonstrated Doppler cooling with $^{171}Yb^{+}$. Rabi flops were successfully demonstrated with a cloud composed of 1160 $^{171}Yb^{+}$ ions and a 50 measurements averaging photon counts by PMT per point in the trajectory. The obtained Rabi frequency was 181 kilorad/s. Due to non-ideal vacuum conditions our ions kept colliding background gas and got knocked off the trap at the rate characterized by the time constant of 4500^{-1} seconds. To better deal the problem of ion loss we proposed that in future experiments the averaging of a 50 measurements per point should be changed to averaging of 50 full trajectories. In this way the ion loss effect will be averaged uniformly throughout the whole trajectory of Rabi oscillations. As the vacuum conditions improve in future this effect of ion loss will be even more minimal thus, allowing for experiments determining things like the coherence times, stability mapping of our ion trap and precise determination of secular frequencies.

An image current detection scheme proposal was detailed and part of it is currently being implemented in the lab. This involved modeling the oscillating ion inside the trap as analogous to a resonant LC circuit. Then current due to this oscillating ion is imaged onto the electrodes as image current which is the coupled out and enhanced for measurement. It was determined that the transimpedance amplifier that we have has insufficient transimpedance gain (of $10^{8}\Omega$) to allow detection of single ion. However,

this can still work for a cloud of ions oscillating coherently in the trap. Looking at the equation for signal to noise ratio there are other improvements that can be made to enhance detection of ions by means of measuring image current. These improvements include increasing the quality factor of a resonant circuit coupling out the image current, increasing the amplitude of oscillation of trapped ions as well as cooling the circuitry involved in resonantly coupling the image current.

The two power law noise models were implemented and successfully related through partial transformation. A Bayesian estimation approach to power law noise-infested systems using one of two known power law noise models and Gaussian mixture models was proposed, detailed and demonstrated with a simulation example. This handling of power law noise will play a crucial role in future when our lasers are locked to some optical cavities which need to be characterized carefully in terms of their noise content. We strongly believe this much of work will serve as a stepping stone towards realization of future studies including unsharp measurements in our lab here at Stellenbosch university.

Bibliography

[1] R. E. March. An introduction to quadrupole ion trap mass spectrometry. *Journal of Mass Spectrometry*, 32:351 – 369, 1997.

[2] K. Deng and Y. L. Sun. A modified model of helical resonator with predictable loaded resonant frequency and q-factor. *Review of Scientific Instruments*, 85:1 – 7, 2014.

[3] L B Wang, T Nguyen, M Schauer, J Torgerson, S Lamoreaux, S Diddams, and V Flambaum. Efficient photoionization loading of ytterbium and indium ion traps. 2007.

[4] S M Olmschenk. *Quantum Teleportation Between Distant Matter Qubits*. PhD thesis, University of Michigan, 2009.

[5] H. P. Breuer and F. Petruccione. *The Theory of Open Quantum Systems*. Oxford University Press, 2007.

[6] A. Orieux and E. Diamanti. Recent advances on integrated quantum communications. *arXiv:1606.07346v1 [quant-ph]*, pages 1 – 23, 2016.

[7] W. Paul. Electromagnetic traps for charged and neutral particles. *Rev. Mod. Phys*, 62:531 – 540, 1990.

[8] H.G. Dehmelt. Radiofrequency spectroscopy of stored ions i: Storage. *Adv. At. Mol. Phys*, 3:53, 1967.

[9] J.I. Cirac and P. Zoller. Quantum computations with cold trapped ions. *Phys. Rev. Lett.*, 74:4091 – 4094, 1995.

[10] D.J. Wineland, C. Monroe, W.M. Itano, D. Leibfried, B.E. King, and D.M. Meekhof. Experimental issues in coherent quantum-state manipulation of trapped atomic ions. *J. Res. Nat. Inst. Stand. Tech.*, 103:259 – 328, 1998.

[11] H. Haffner, C.F. Roos, and R. Blatt. Quantum computing with trapped ions. *Phys. Rep.*, 469:155 – 203, 2008.

[12] S.A. Webster, P. Taylor, M. Roberts, G.P. Barwood, and P. Gill. Kilohertz-resolution spectroscopy of the 2s1/2 - 2f7/2 electric octupole transition in a single 171yb+ ion. *Phys. Rev. A*, 65:052501, 2002.

[13] M. Chwalla, J. Benhelm, K. Kim, G. Kirchmair, T. Monz, M. Riebe, P. Schindler, A.S. Villar, W. Hansel, C.F. Roos, R. Blatt, M. Abgrall, G. Santarelli, G.D. Rovera, and P. Laurent. Absolute frequency measurement of the 40ca+ 4s 2s1/2 - 3d 2d5/2 clock transition. *Phys. Rev. Lett.*, 102:023002, 2009.

[14] Kurt Jacobs. *Quntum Measurement Theory and its Applications*. Cambridge University Press, 2014.

[15] T. Konrad and H. Uys. Maintaining quantum coherence in the presence of noise through state monitoring. *Physical Review A*, 85:012102–1 – 012102–4, 2012.

[16] H. Bassa, S. K. Goyal, S. K. Choudhary, H. Uys, L. Diosi, and T. Konrad. Process tomography via sequential mmeasurement on a single quantum system. *Physical Review A*, 92:032102, 2015.

[17] P. J. W. du Toit, S. C. Burd, T. Konrad, and H. Uys. Real-time state estimation and feedback control of an oscillating qubit via self-fulfilling prophecy (sfp). *METROLOGIA*, 56(1):104003, 2019.

[18] H. Uys, H. Bassa, P. du Toit, S. Gosh, and T. Konrad. Quantum control through measurement feedback. *Physical Review A*, 97:060102, 2018.

[19] A. Soare, H. Ball, D. Hayes, X. Zhen, M. C. Jarratt, J. Sastrawan, H. Uys, and M. J. Biercuk. Experimental bath engineering for quantitative studies of quantum control. *Physical Review A*, 89:042329, 2014.

[20] A. Friedenauer, H. Schmitz, J.T. Glueckert, D. Porras, and T. Schaetz. Simulating a quantum magnet with trapped ions. *Nature Phys*, 4:757 – 761, 2008.

[21] K. Kim, M.S. Chang, S. Korenblit, R. Islam, E.E. Edwards, J.K. Freericks, G.D. Lin, L.M. Duan, and C. Monroe. Quantum simulation of frustrated ising spins with trapped ions. *Nature*, 465:590 – 593, 2010.

[22] M. Keller, B. Lange, K. Hayasaka, W. Lange, and H. Walther. Deterministic cavity quantum electrodynamics with trapped ions. *J. Phys. B: At. Mol. Opt. Phys*, 2003:613 – 622, 36.

[23] P.F. Herskind, A. Dantan, J.P. Marler, M. Albert, and M. Drewsen. Realization of collective strong coupling with ion coulomb crystals in an optical cavity. *Nature Phys*, 5:494 – 498, 2009.

[24] National Academies of Sciences Engineering and Medicine. *Quantum Computing: Progress and Prospects*. The National Academies Press, Washington, DC, 2019.

[25] P. Wieburg. A linear paul trap for ytterbium ions. Master's thesis, Universitat Hamburg, 2014.

[26] D. Leibfried, R. Blatt, C. Monroe, and D. Wineland. Quantum dynamics of single trapped ions. *Reviews of Modern Physics*, 75:281 – 324, 2003.

[27] D.J. Berkeland, J.D. Miller, J.C. Bergquist, W.M. Itano, and D.J. Wineland. Minimization of ion micromotion in a paul trap. *Journal of Applied Physics*, 83:5025 – 5033, 1998.

[28] M.D. Hughes B. Lekitsch J.A. Broesma W. K. Hesinger. Microfabricated ion traps. *arXiv:1101.3207 [quant-ph]*, 2011.

[29] J.M. Amini, J. Britton, D. Leibfried, and D.J. Wineland. Microfabricated chip traps for ions. *arXiv:0812.3907v1 [quant-ph]*, 2008.

[30] E. M. Purcell. Spontaneous emission probabilities at radio frequencies. *Phys. Rev. 69*, 681, 1946.

[31] Peter W. Milonni. *The Quantum Vacuum: An Introduction to Quantum Electrodynamics*. Academic Press, 1993.

[32] C. Chou, C. Auchter, J. Lilieholm, K. Smith, and B. Blinov. Single ion imaging and fluorescence collection with a parabolic mirror trap. *Review of Scientific Instruments*, 88:086101, 2017.

[33] J. D. Siverns and L. R. Simkins. On the application of radio frequency voltages to ion traps via helical resonators. *arXiv:1106.5013v3*, 2011.

[34] A Reza, A Misra, S Sarkar, A K Sikdar, and P Das. Development of a Helical Resonator for Ion Trap Application. *IEEE Applied Electromagnetics*, 2015.

[35] K. G. Johnson and J.D. Wong-Campos. Active stabilization of ion trap radiofrequency potentials. *Review of Scientific Instruments*, 87:1 – 6, 2016.

[36] Gandolfi Davide. Compact rf amplifier for scalable ion-traps. Master's thesis, University of Innsbruk, 2011.

[37] Phyo Aung Kyaw. Constructing an ultra-high vacuum chamber and a radio frequency helical resonator for trap ions. Master's thesis, Amherst College, 2014.

[38] S Qiao. Constructing a linear paul trap system for measuring time-variation of the electron-proton mass ratio. Master's thesis, Amherst College, 2013.

[39] R. E. Berg and D. G. Stork. *The Physics of Sound*. Pearson, 2004.

[40] R Sarpeshkar. *Ultra Low Power Bioelectronics: Fundamentals, Biomedical AApplication and Bio-inspired Systems*. Cambridge University Press, 2010.

[41] Y. Sun and J. K. Fidler. Design of pi impedance matching networks.

[42] C. Bowick, J. Blyler, and C. Ajluni. *RF Circuit Design, Second Edition*. Newnes, Newton, MA, USA, 2nd edition, 2007.

[43] Joseph Carr. *Secrets of RF Circuit Design*. The McGraw-Hill Companies Inc, 2001.

[44] K. Deng and Y. L. Sun. Design and construction of helical resonator for ion traps. *2013 Joint UFFC EFTF and PFM Symposium*, pages 898 – 900, 2013.

[45] R. Ozeri. Tutorial: The trapped-ion qubit tool box. *Contemporary Physics: arXiv:1106.1190v1 [quant-ph]*, 00:1 – 23, 2011.

[46] D. M. Lucas, C. J. S. Donald, J. P. Home, M. J. McDonnell, A. Ramos, N. Stacey, J.-P. Stacey, A. M. Steane, and S. C. Webster. Oxford ion-trap quantum computing project. *Phil. Trans. R. Soc. Lond. A*, 361:1401 – 1408, 2003.

[47] N. C. Brown and K. R. Brown. Comparing zeeman qubits to hyperfine qubits in the context of the surface code: 174yb+ and 171yb+. *arXiv:1803.0254v2 [quant-ph]*, pages 1 – 7, 2018.

[48] C J Foot. *Atomic Physics*. Oxford University Press, 2007.

[49] H Moya-Cessa, F Soto-Eguibar, J M Vargas-Martinez, R Juarez-Amaro, and A Zuniga-Segundo. Ion-laser interactions: The most complete solution. *Physics Reports*, 513:229 – 261, 2012.

[50] Andrew J. S. Hamilton. Apas 5110. internal processes in gases: Transition probabilities and selection rules. Technical report, Joint Institute for Laboratory Astrophysics, 1999.

[51] M Johanning, A Braun, D Eiteneuer, Chr Paape, Chr Balzar, W Neuhauser, and Chr Wunderlich. Resonance enhanced isotope-selective photoionization of ybi for ion trap loading. *arXiv:0712.0969v2 [physics.atom-ph]*, 2010.

[52] A. Mortensen, J. J. T. Lindballe, I. S. Jensen, P. Staanum, D. Voigt, and M. Drewsen. *Phys. Rev. A 69(4)*, page 042502, 2004.

[53] N. Kjaergaard, L. Hornekaer, A Thammesen, Z Videsen, and M Drewsen. *Appl. Phys. B 71*, page 207, 2000.

[54] S. Gulde, D. Rotter, P. Barton, F. Schmidt-Kaler, R. Blatt, and W. Hogervorst. *Appl. Phys. B 73*, page 861, 2001.

[55] Yugo Onoda. *Trapping of Yb+ Loaded through Photoionization in RF Ion Trap*. PhD thesis, Kyoto University, 2011.

[56] Y. Onoda, K. Sugiyama, M. Ikeda, and M. Kitano. Loading rate of yb+ loaded through photoionization in radiofrequency ion trap. *Applied Physics B*, 105:729 – 740, 2011.

[57] Y Y Jau, J D Hunker, and P D D Schwindt. F - state quenching with ch4 for buffer-gas cooled 171yb+ frequency standard. *AIP Advances*, 5:117209–1 – 117209–8, 2015.

[58] K Pandey, A K Singh, P V K Kumar, M V Suryanarayana, and V Natarajan. Isotope shifts and hyperfine structure in the 555.8 nm 1s0 - 3p1 line of yb. *Physical Review A*, 80:022518–1 – 022518–6, 2009.

[59] Y Ismail, S Joshi, A Forbes, and F Petruccione. Instrumentation limitation on a polarization-based entangled photon source. *Journa of the Optical Society of America B*, 34:1084 – 1089, 2017.

[60] Martina Knoop. Detection techniques for trapped ions. *Physics with Trapped Charged Particles: Lectures from Les Houches Winter School. Edited by RC Thompson, M Knoop, N Madsen. World Scientific Publishing Co. Pte. Ltd.*, 18:25 – 42, 2014.

[61] M Nappi, V Frankevich, M Soni, and R G Cooks. Characteristics of a broad-band fourier transform ion trap mass spectrometer. *Int. J. Mass Spectrom*, 177:91 – 104, 1998.

[62] M Soni, V Frankevich, M Nappi, R E Santini, J W Amy, and R G Cooks. Broad-band fourier transform quadrupole ion trap mass spectrometry. *Analytical Chemistry*, 68:3314 – 3320, 1996.

[63] P Racke, D Spemann, J W Gerlach, B Rauschenbach, and J Meijer. Detection of small bunches of ions using image charges. *Scientific Reports*, 8:1 –10, 2018.

[64] DJ Heinzen and DJ Wineland. Quantum-limited cooling and detection of radio-frequency oscillations by laser-cooled ions. *Physical Review A*, 42:2977 – 2994, 1990.

[65] R. Ethan, G. Badman, E. Patterson, J. Mitchell, Wells Robert, E. Santini, and R. Graham Cooks. Differential non-destructive image current detection in a fourier transform quadrupole ion trap. *Journal of Mass Spectrometry*, 34:889 – 894, 1999.

[66] M Knoop and R C Thompson. *Physics with Trapped Charged Particles*. arXiv:1311.7220 [physics.atom-ph], 2014.

[67] J. S. Babis, R. P. Sperline, A. K. Knight, D. A. Jones, C. A. Gresham, and M. B. Denton. Performance evaluation of miniature ion mobility spectrometer drift cell for application in hand-held explosives detection ion mobility spectrometers. *Analytical and bioanalytical chemistry*, 395:411 – 419, 2009.

[68] G.A. Eiceman, Z. K. Herbert, and H. Hill Jr. *Ion Mobility Spectrometry (Third Edition)*. CRC Press, 2013.

[69] M.T.I. Badal, M.B.I. Reaz, M.A.S. Bhuiyan, and F. Haque. Advancement of cmos transimpedance amplifier for optical receiver. *Transactions on Electrical and Electronic Materials*, pages 1 – 20, 2018.

[70] T. H. Ngo, T. W. Lee, and H. H. Park. Design of transimpedance amplifier for optical rreceiver in 0.13um cmos. *Digest of the 9th International Conference on Optical Internet*, 2010.

[71] E Sackinger. *Analysis and Design of Transimpedance AAmplifier for Optical Receivers*. John Wiley & Sons, Inc, 2017.

[72] M. Crescentini, M. Bennati, S. Saha, J. Ivica, M. Planque, H. Morgan, and M. Tartagni. A low-noise transimpedance amplifier for blmbased ion channel recording. sensors. *Sensors*, 16(5):1 – 20, 2016.

[73] Burr Brown. Noise analysis of fet transimpedance aamplifier. Technical report, Texas Instuments, 1994.

[74] R. E. Kalman. A New Approach to Linear Filtering and Prediction Problems. *Trans. ASME Series D: J. Basic Eng.*, 82:39–49, 1960.

[75] G. Smith, S. Schmidt, and L. McGee. Application Of Statistical Filter Theory To The Optimal Estimation Of Position And Velocity On Board A Circumlunar Vehicle. *Tech. Rep. NASA TR-135*, 1962.

[76] S. J. Julier, J. K. Ulmann, and H. F. Durrant-Whyte. A new approach for filtering nonlinear systems. *American Control Conference Proceedings of 1995*, 3:1628–1632, 1995.

[77] J. Ching, J. L. Beck, and K. A. Porter. Bayesian state and parameter estimation of uncertain dynamical systems. probabilistic engineering mechanics, 2006.

[78] N. J. Gordon, D. J. Salmond, and A. F. M. Smith. A novel approach to nonlinear/non-gaussian bayesian state estimation. *IEEE Proceedings on Radar and Signal Processing*, 140:107–113, 1993.

[79] A. G. Wills, J. Hendricks, C. Renton, and B. Ninness. A bayesian filtering algorithm for gaussian mixture models. *arXiv:1705.05495v1 [stat.ML]*, pages 1–17, 16 May 2017.

[80] A. R. Runnalls. Kullback-leibler approach to gaussian mixture reduction. *IEEE Transactions on Aerospace and Electronic Systems*, 43, 2007.

[81] J. Barnes and S. Jarvis. Efficient numerical and analog modeling of flicker noise processes. *National Bureau of Standards Technical Note 604*, 1971.

[82] R. Kumar, A. Kumar, and A. J. Kumar. Effects of 1/f baseband noise and its suppression using kalman filter in ofdm system. *International Journal of Engineering Research & Technology*, 2:724 – 729, 2013.

[83] J. A. Davis, C. A. Greenhall, and P. W. Stacey. A kalman filter clock algorithm for use in the presence of flicker frequency modulation noise. *Metrologia*, 42(1):1, 2005.

[84] T. Rosenband, D. Hume, C. W. Chou, J. Koelemeij, A. Brusch, et al. Alpha-dot or not: Comparison of two single atom optical clocks. *Frequency Standards and Metrology*, pages 20 – 33, October 05, 2008.

[85] Greenhall C. A. An approach to power-law phase-noise models through generalized functions. *Metrolgia*, 47:605 – 615, 2010.